High-Order Harmonic Generation Driven by Mid-Infrared Laser Light

by

Benjamin R. Galloway

B.S., Colorado School of Mines, 2011

M.S., Colorado School of Mines, 2012

A thesis submitted to the

Faculty of the Graduate School of the

University of Colorado in partial fulfillment

of the requirements for the degree of

Doctor of Philosophy

Department of Physics

2017

This thesis entitled:
High-Order Harmonic Generation Driven by Mid-Infrared Laser Light
written by Benjamin R. Galloway
has been approved for the Department of Physics

_____

Prof. Margaret Murnane

_____

Prof. Henry Kapteyn

Date _____

The final copy of this thesis has been examined by the signatories, and we find that both the content and the form meet acceptable presentation standards of scholarly work in the above mentioned discipline.

Galloway, Benjamin R. (Ph.D., Physics)

High-Order Harmonic Generation Driven by Mid-Infrared Laser Light

Thesis directed by Prof. Margaret Murnane

Light is a powerful tool for making observations of the physical world. In particular, light in the extreme ultraviolet (EUV) and X-ray regimes enable unique and higher resolution measurements than is possible using longer wavelengths. A relatively new technique called high-order harmonic generation (HHG) provides a route for scientists to produce light in these useful spectral ranges, starting with lasers operating at more accessible wavelengths. HHG has been successfully applied to a number of applications including high resolution microscopy, spectroscopy, and measurements of magnetism, thermal transport, and molecular structure.

This dissertation covers several illuminating studies of HHG in the temporal and spectral domains when the process is driven by long wavelength, mid-infrared light. Interestingly, the characteristics of the harmonic emission are highly dependent on the driving laser parameters and geometries. As the driving laser wavelength is increased, the harmonic cutoff and bandwidth naturally broaden, while the emitted pulse train reduces in length until a single isolated burst of phase-matched harmonics with sub-femtosecond duration is achieved. This trend is experimentally verified by performing an electric field autocorrelation of the harmonic emission. The resulting HHG supercontinuum has particular utility in X-ray absorption fine structure spectroscopies, where the nanoscale lattice structure can be probed. These spectroscopies have been performed on polymer, scandium, and iron samples using the broadest HHG bandwidths achieved to date, extending up to 1.6 keV. Pushing this harmonic cutoff further would conventionally require the use of longer wavelength drivers approaching the far-infrared regime. However, long driving wavelengths can also result in relativistic effects, resulting in longitudinal Lorentz drifts that could cause the HHG process to be inhibited. A theoretical accounting of all of the forces involved does not indicate HHG would be shut off entirely, however, and it is possible for HHG to occur even with driving

wavelengths beyond 10 µm and harmonic cutoffs in the hard X-ray regime. The use of cylindrical vector beams or multi-beam geometries can also be used to compensate for relativistic effects, as well as to create new phase-matching conditions for sum and difference frequency processes. Through high-order difference frequency generation in a two-beam noncollinear geometry, it is predicted that the conventional phase-matching limitations could be significantly exceeded, opening up the possibility to use visible drivers to reach the soft X-ray regime or further. Pushing the limits of the HHG spectral characteristics would inevitably enable new levels of capability for its applications.

The investigations presented here will follow a progression from shorter to longer wavelengths as drivers for the HHG process, starting with experiments using the most commonly used Ti:sapphire wavelength of 800 nm, moving to 1.3 µm and 2.0 µm, then up to 3.9 µm, and ultimately arriving at theory for far-infrared drivers up to 20 µm. Furthermore, the conventional single-beam driving configuration will be primarily investigated, but new capabilities are predicted for multi-beam and multi-color geometries, which will be discussed.

Dedication

For Jenny - because if I didn't have this, I'd still have you.

Acknowledgements

First, I would like to thank Prof. Margaret Murnane and Prof. Henry Kapteyn for the excellent guidance and constant support. The opportunities they opened up for me have taught me so much and have made my Ph.D. journey enjoyable.

The entire KM group also deserves acknowledgment for all of the aid over the years. In particular, a big thanks to Tenio Popmintchev, Dimitar Popmintchev, Ming-Chang Chen, Dan Adams, Michael Gerrity, Seth Cousin, Amitava Adak, Chris Mancuso, Christian Gentry, Kevin Dorney, Jennifer Ellis, Liz Shanblatt, Giulia Mancini, Chrissy Porter, and Michael Tanksalvala. The collaboration with KM Labs has made my research more feasible, so I would like to thank Sterling Backus, Xiaoshi Zhang, Daisy Raymondson, Jon Garlick, and Stephen Uhlhorn for their laser and production expertise. I appreciate Prof. Chip Durfee for sending me along to the KM group and for teaching me the fundamentals of optics.

I would like to express my deep appreciation for the outstanding support from the Department of Energy, National Nuclear Security Administration, and Krell Institute through the Stewardship Science Graduate Fellowship program - there are some very good people that manage the fellowship to whom I owe a considerable amount. (This work was supported by the Department of Energy National Nuclear Security Administration Stewardship Science Graduate Fellowship program, which is provided under grant number DENA002135.)

Finally, I would like to thank the support of my family and friends who kept me sane during the many instances of laser trouble. I couldn't have made it without the love and laughter. Many thanks!

Contents

Chapter

Tables

Table

Figures

Figure

Chapter 1

Introduction to High-Order Harmonic Generation

1.1 Background

Light is an incredibly powerful tool for measurement and excitation. From the casual use of light by the human eye, to the implementation of X-rays to create shock waves in matter that can initiate a fusion reaction - light truly is versatile. The various properties of photons - the fundamental particles that make up light - allow them to be utilized so flexibly. Photons carry energy and momentum, and they can be superimposed to create electromagnetic fields with arbitrary spatial and temporal structure. The polarization and coherence properties of light give it additional complexity that can be harnessed for a plethora of applications. In particular, laser light makes use of the coherent nature of photons to create a highly directional beam of light. Through the process of stimulated emission, lasers take single photons and coherently multiply them many orders of magnitude, reaching electromagnetic intensities in the laboratory unavailable through any other means.

Since the first demonstration of the laser by Theodore Maiman in 1960 [77], lasers have found applications in imaging [156, 153, 126, 150, 84, 127, 131], remote sensing [108, 82], spectroscopy [66, 6, 35, 135], micro-machining [83, 31, 20, 168], nano-lithography [148, 54, 41], particle acceleration [119, 162, 151, 158], quantum mechanics [5, 80, 113, 114, 86], magnetics [157, 138, 159], fusion [88, 152], ultra-cold matter [67, 78], thermal transport [91, 133, 52], gravitational research [99, 125], and more. Each of these applications requires particular laser properties in terms of wavelength (color), bandwidth (pulse duration), peak and average powers, polarization, and coherence. In

particular, light in one region of the electromagnetic spectrum (Fig. 1.1) may be suitable for a particular application, but inappropriate for another. Alternatively, an application might be able to use of a wide range colors, but the sensitivity or fidelity of the result could be dependent on the particular wavelength(s) used. For applications that require the coherence of laser light, the most easily accessible colors are in the infrared and visible regions. The reason behind this limitation lies in the atomic transition energies of the available materials that can be used in lasers and amplifiers. Additionally, as the laser wavelength is decreased (toward the ultraviolet regime), the upper state lifetime of the gain medium reduces. This makes it more difficult to maintain the population inversion that is required for the laser to operate. As a result, conventional laser oscillators and amplifiers in the extreme ultraviolet (EUV) and X-ray regions of the spectrum would require a prohibitively large amount of (fast) supply power. However, there exist several alternative approaches to generate laser-like beams of EUV and X-ray light: synchrotrons, free-electron lasers (FELs), and high-order harmonic generation (HHG).

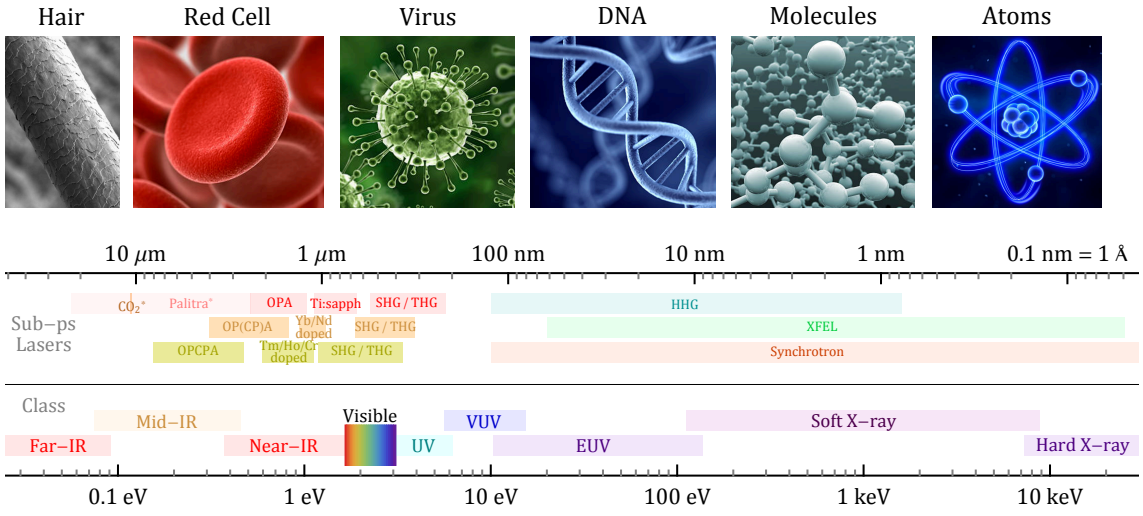

Figure 1.1: Regimes of the electromagnetic spectrum and regions where ultrafast laser technology is currently available [56, 171, 97, 65, 47, 139, 111]. *The Palitra^{TM} optical parametric amplifier specifies a broad tunability range for ultrafast operation, but the conversion efficiency for high energy models is less than 1% for idler wavelengths greater than 2.6 µm [118]. A CO_2 amplifier can be used to boost the idler at 10.6 µm, but at the cost of bandwidth and achievable pulse duration [104, 101].

Table 1.1: A comparison of the accessible range of photon energies E_{ph}, pulse duration dt, coherence times τ_{coh}, and degree of transverse spatial coherence r_{coh}/w for HHG, X-ray FEL, and synchrotron light sources. The values listed are approximate records to date. *Achieving ultrashort pulse durations or high levels of coherence with facility scale sources usually requires pulse-slicing, bandpass filtering, or spatial filtering, each of which reduce the source brightness. For HHG, tuning the driving laser wavelength can also be associated with trade-offs.

	HHG	X-ray FEL	Synchrotron
E_{ph} range	0.3 eV - 1.6 keV [161]	0.26 - 25 keV [34]	0.1 eV - $>$ 300 keV [62]
dt_{min}	$\sim$300 as [18]	100 as [61]	100 fs* [13]
τ_{coh}	$>$ 1 s [12]	1.5 fs [174]	$\sim$as* [62]
r_{coh}/w	$>$ 0.75 [155]	0.45 [174]	0.008 - 0.38 [117]

Synchrotrons and FELs are facility scale sources that are capable of producing very bright beams of EUV/X-ray light with wavelength tunability and progressively improving levels of coherence and temporal duration (see Table 1.1 and Fig. 1.2). Despite the many advantages of these large-scale sources, their cost and accessibility can be prohibitive in cases. For example, proposed experiments that have a high level of scientific risk might be denied time on the light source. If an experiment is approved, the allotted time could be insufficient to perform a thorough study. Fortunately, HHG is a complementary technology that can provide more opportunities for experimentation, but at the cost of source brightness and spectral ranges available to date.

High-order harmonic generation describes a frequency conversion technique in which an intense driving laser is focused in a medium, and as a result of the laser-matter interaction, harmonic frequencies of the driving laser are emitted. In most cases, the HHG medium is a noble gas, but molecules and solid targets have also been used [48, 116, 173]. At the core of the HHG process is the coherent nature of the driving laser and the electrons in the target medium, which work together to produce a highly coherent beam of harmonics. Figure 1.3 depicts HHG from a photon point of view. A number of effects influence the characteristics of the harmonic output, both on the microscopic and macroscopic scales. The remainder of Chapter 1 will elaborate on these fundamental details behind the HHG process, while the following chapters provide experimental and theoretical approaches that have been and can be performed to provide insight into the limits of

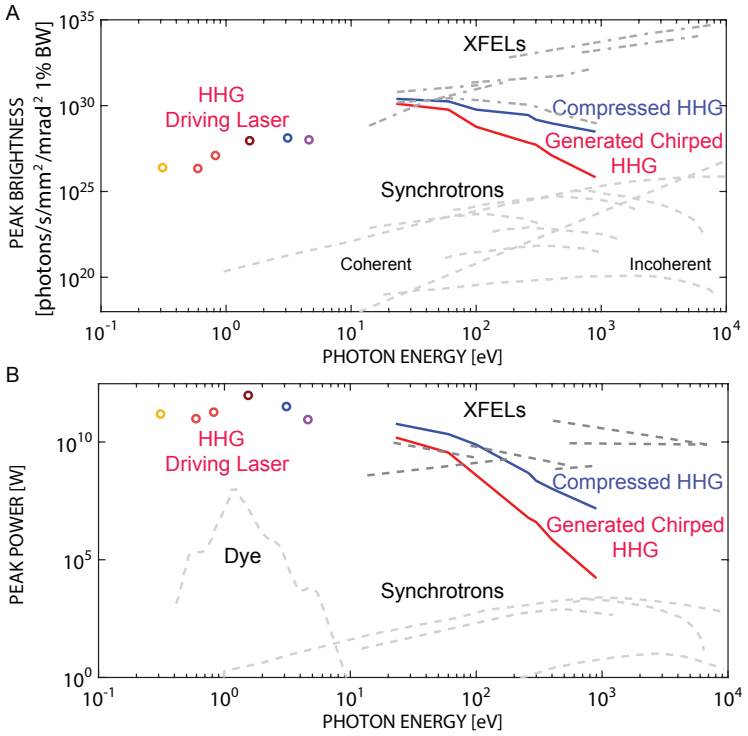

Figure 1.2: Plots of the (A) peak brightness and (B) peak power of coherent HHG X-ray sources (solid lines), compared to X-ray FELs and synchrotron sources (dashed lines). Driving lasers used for HHG shown in open circles - 3.9 µm, 2.1 µm, 1.5 µm, 0.8 µm, 0.4 µm, 0.27 µm). Data compiled from [34, 27, 64].

HHG technology when driven by mid-infrared laser light.

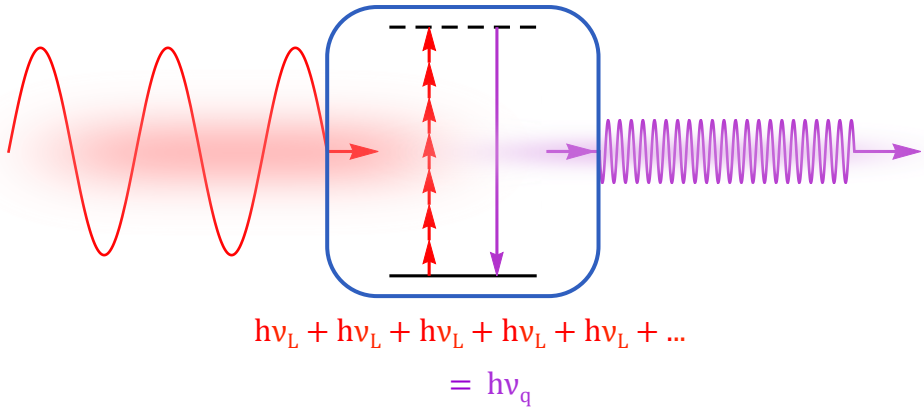

Figure 1.3: The photon picture of HHG. The driving laser with fundamental photon energy $h\nu_L$ contributes q photons to generate a harmonic photon with energy $h\nu_q$.

Nomenclature

In this dissertation, SI units are used unless otherwise noted. The following physical constants will be used:

- ϵ_0 is the permittivity of free space ($8.854 \times 10^{-12}\ F/m$).
- μ_0 is the permeability of free space ($1.256 \times 10^{-6}\ N/A^2$).
- e is the natural Euler number (2.718).
- c is the speed of light in free space ($2.998 \times 10^{8}\ m/s$).
- $\hbar = \frac{h}{2\pi}$ is the reduced Planck constant ($1.054 \times 10^{-34}\ J \cdot s/rad$).
- q_e is the charge of the electron ($-1.602 \times 10^{-19}\ C$).
- m_e is the mass of the electron ($9.109 \times 10^{-31}\ kg$, $511\ keV$).
- r_B is the Bohr radius ($5.292 \times 10^{-11}\ m$)
- $r_e = \frac{1}{4\pi\epsilon_0}\frac{q_e^2}{m_e c^2}$ is the classical electron radius ($2.818 \times 10^{-15}\ m$)

- N_a is the number density of atoms in a gas at standard temperature and pressure ($2.687 \times 10^{25}\ m^{-3}$).

Additionally, the following formulae will be implied:

- $n = \sqrt{\frac{\epsilon\mu}{\epsilon_0\mu_0}}$ is the index of refraction of a medium.
- $I_L = \frac{c\epsilon_0 n}{2}|E_{L0}|^2$ is the intensity of a laser field with electric field strength E_{L0}.
- $k = \frac{2\pi n}{\lambda}$ is the wavenumber of an electromagnetic wave with wavelength λ.
- $\omega = \frac{2\pi c}{\lambda}$ is the angular frequency of an electromagnetic wave with wavelength λ.
- $T = 2\pi/\omega = \lambda/c$ is the period of an electromagnetic wave with wavelength λ.
- dt is the duration of a laser pulse, defined as the full width at half maximum (FWHM) of the intensity profile.
- $v_\phi = \frac{\omega}{k}$ is the phase velocity of an electromagnetic wave through a medium.
- $v_g = \frac{\partial\omega}{\partial k}$ is the group velocity of an electromagnetic wave through a medium.

1.2 Microscopic Picture of HHG

The mechanism that facilitates HHG fundamentally resides at the atomic scale. In HHG, driving radiation illuminates the atoms in the target medium, and energy is re-radiated by the electrons bound to the atoms. According to Coulomb's law, charged particles experience a force in response to an electric field. Electrons, being 1,837 times less massive than protons, are accelerated more readily by the oscillating electric field of the illuminating electromagnetic wave. The subsequent motion of the electron, an accelerating charged particle, gives rise to re-radiation. However, for frequency conversion to occur, the system must be nonlinear - that is, the electron must not simply oscillate at the same frequency as the incident laser field. The Coulomb potential from the ion allows the electron to take on nonlinear motion, thus facilitating frequency conversion.

The field of nonlinear optics is rich in processes where spectral/temporal and angular/spatial characteristics undergo changes, where much of the observed phenomena can be explained using perturbation theory. However, the spectral trends experimentally observed in HHG do not agree with perturbative predictions. In the first report on HHG in 1987 [81], the observed harmonic flux did not simply scale exponentially with harmonic order; there was a plateau at high orders (Fig. 1.4). This indicated a non-perturbative regime of frequency conversion that had not been seen in lower intensity experiments. A theoretical framework other than perturbation theory was needed to explain these findings.

In 1993, a semi-classical three step model was proposed to describe the HHG process [26, 60], and the predictions of that model [68, 70], including the non-perturbative characteristics in the spectral domain, have held true experimentally. In the three step model, the electron starts bound to its atom, confined by the atomic Coulomb potential. Then, the electron is subjected to the electric field of the laser, thus distorting the total potential that it experiences. If the laser field is intense enough, the electron can tunnel ionize through the distorted Coulomb barrier. Once free of the short-range potential of the ion, the electron propagates only under the influence of the laser field. Initially, the electron accelerates away from the ion, but since the laser field is oscillatory, the electron may reverse direction and return close to the ion. If the electron does re-encounter the ion, there is a probability for the electron to recombine with it, returning to its ground state and giving up any excess energy that it might have gained while under the influence of the laser field. That energy is released in the form of a photon. Thus, the three step model consists of (1) ionization, (2) propagation, and (3) recombination. Figure 1.5 depicts this process, and the details behind each step are conveyed in the following sections.

1.2.1 Step 1: Ionization

In the first step of HHG, the electron is liberated from its parent ion by the incident laser field. This can occur if the electric field strength of the laser approaches the Coulomb field strength of the ion. In the simplest case, the atomic Coulomb potential experienced by the electron is given

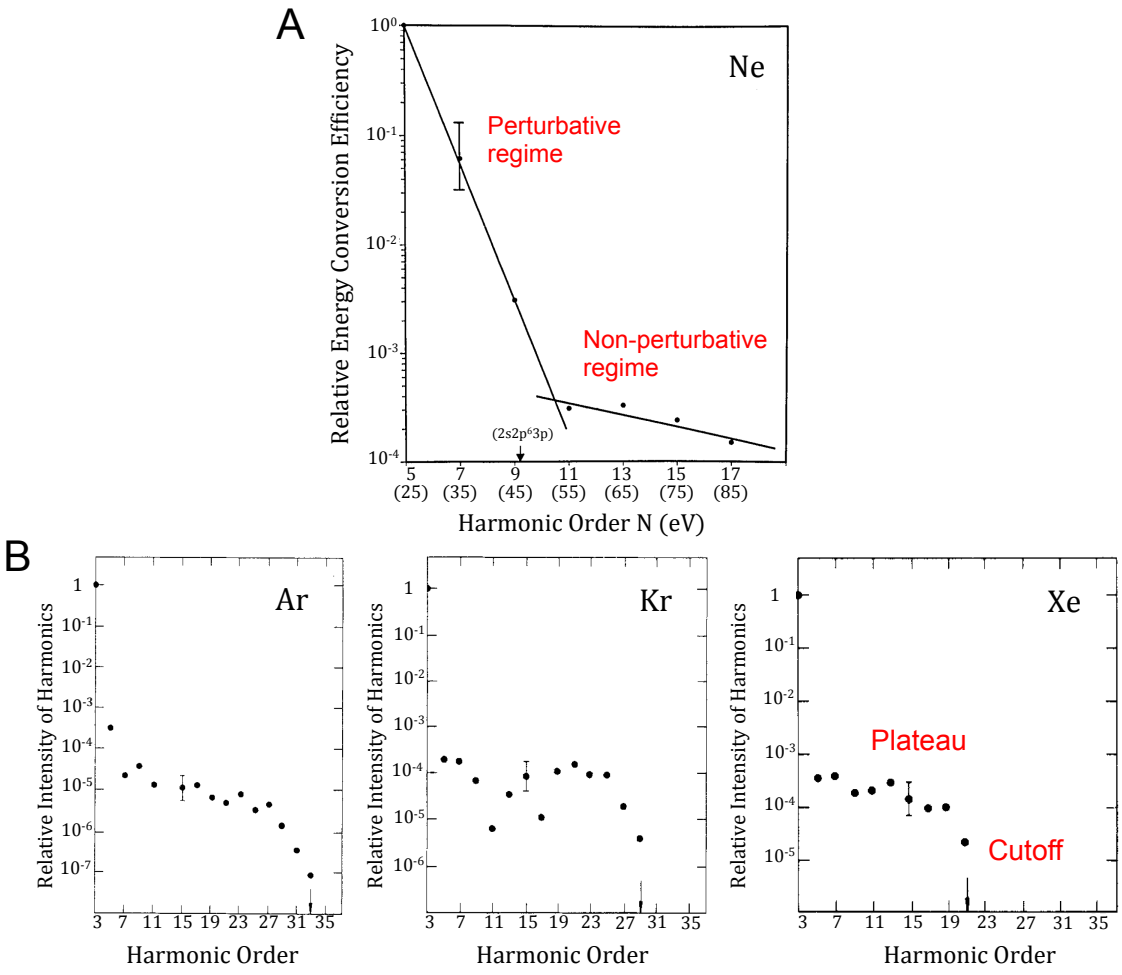

Figure 1.4: The first reports on HHG, demonstrating perturbative behavior at low harmonic orders and non-perturbative behavior at high orders. (A) A plot of the relative harmonic conversion efficiency in Ne, demonstrating the shift from perturbative behavior to non-perturbative behavior at the 11th harmonic. Adapted from [81]. (B) Similar plots showing the "plateau" and "cutoff" for harmonics in Ar, Kr, and Xe. Adapted from [36]. Typical error bars are shown for a single harmonic.

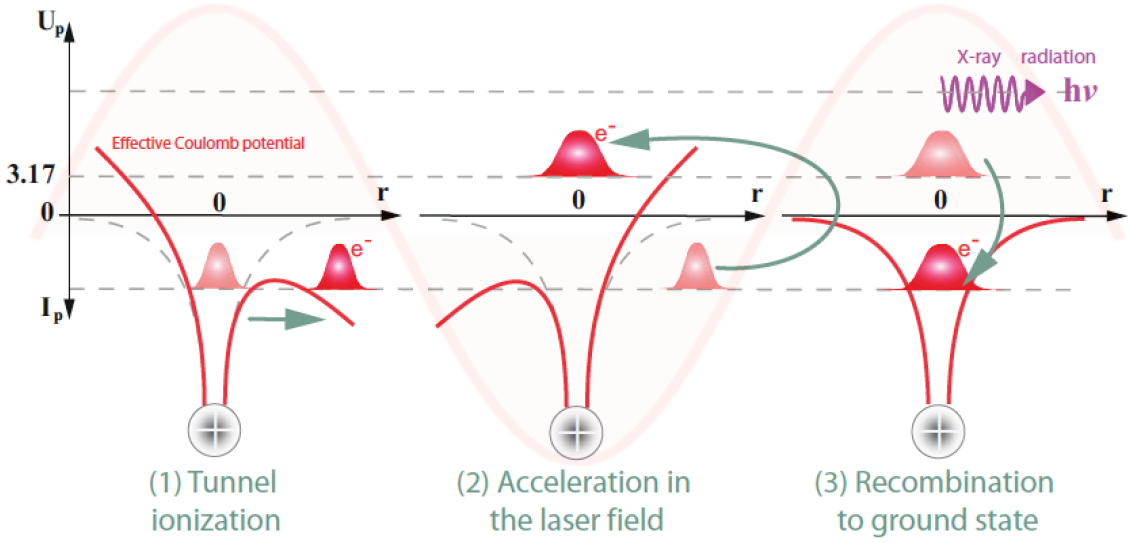

Figure 1.5: Diagram of the three step model describing the HHG process. Adapted from [106].

by:

$$V_{atomic}(\boldsymbol{r}) = -\frac{q_e^2}{4\pi\epsilon_0 r} \tag{1.1}$$

The electric field of the laser introduces an additional potential felt by the electron:

$$V_{laser}(\boldsymbol{r}, t) = -\int_0^{\boldsymbol{r}} q_e \boldsymbol{E}_L(\boldsymbol{r}\,', t) \cdot d\boldsymbol{r}\,' \tag{1.2}$$

where $\boldsymbol{E}_L(\boldsymbol{r}, t)$ is the electric field of the laser, which points in a direction $\hat{\boldsymbol{\psi}}$ corresponding to the local polarization direction of the laser field [1] . In this section, consider a plane-wave electric field of the form $\boldsymbol{E}_L(\boldsymbol{r}, t) = E_{L0}\cos(\omega_L t)\hat{\boldsymbol{\psi}}$. The total potential experienced by the electron is then the sum of Eq. (1.1) and Eq. (1.2), which may result in one of several ionization possibilities depending on the strength of E_{L0}: multiphoton ionization, tunneling ionization, and barrier-suppressed ionization. Each of these are depicted in Fig. 1.6.

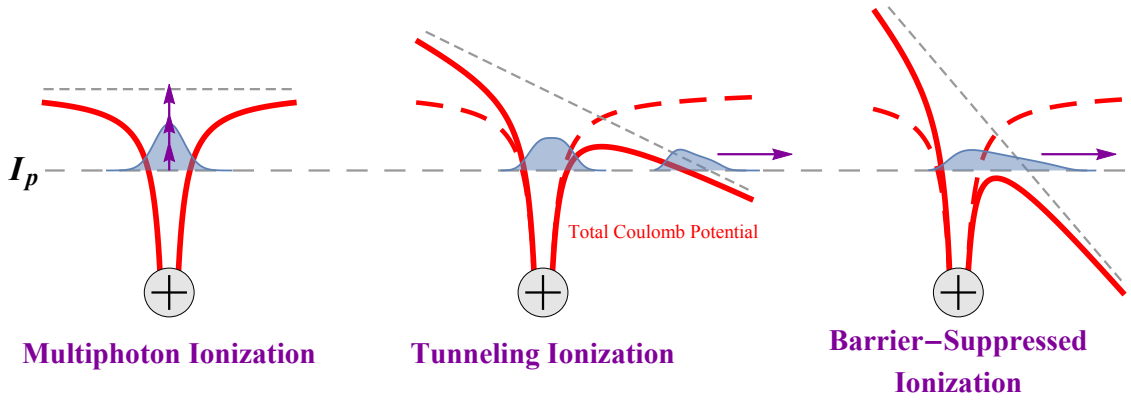

Figure 1.6: Diagrams indicating the possible mechanisms for ionization under the influence of intense laser light. The electric field strength of the laser increases from left to right. It is noted that single-photon ionization is a possibility if the laser photon energy $\hbar\omega_L$ is larger than the ionization potential I_p of the atom, which is not considered here.

The parameters that determine the particular ionization regime are inherent to the laser characteristics and the atomic ionization potential, as described by Keldysh [55]. In particular, Keldysh introduced a single parameter that relates the ionization potential to the laser pondero-

[1] The local polarization direction may vary as a function of time, as in the case of elliptically polarized light. Furthermore, the polarization of the laser mode can vary spatially (e.g. cylindrical vector beams). The local field polarization at the location of the atom is of primary importance for the microscopic picture of HHG.

motive potential, dubbed the Keldysh adiabatic parameter $\gamma_{Keldysh}$:

$$\gamma_{Keldysh} = \sqrt{\frac{I_p}{2U_p}} \tag{1.3}$$

where U_p is the ponderomotive potential of the laser field:

$$U_p = \frac{q_e^2 E_{L0}^2}{4 m_e \omega_L^2} \tag{1.4}$$

The three regimes of ionization can be determined through $\gamma_{Keldysh}$ according to the following:

- $\gamma_{Keldysh} >> 1$, **Multiphoton Ionization**: The laser ponderomotive potential U_p is much smaller than the ionization potential I_p of the atom, thus distorting the total Coulomb potential to a small degree. Only the perturbative mechanism of multiphoton ionization can liberate the electron from its potential well, in which N photons from the driving field impart the sum of their energies to the electron, liberating it from the potential well ($N \cdot \hbar\omega_L \geq I_p$). The ionization rate in this regime scales perturbatively as I_L^N [172].

- $\gamma_{Keldysh} < 1$, **Tunneling Ionization**: U_p approaches I_p, significantly distorting the Coulomb well and creating a finite barrier through which a portion of the electron wavefunction can tunnel. Only a portion of the electron wavefunction escapes the ion's Coulomb potential, while the remainder stays in a bound state. The ionization rate in this regime is related to the proportion of the wavefunction that tunnels and can be modeled using Ammosov-Delone-Krainov (ADK) theory [4], discussed later in this section.

- $\gamma_{Keldysh} << 1$, **Barrier-Suppressed Ionization**: U_p greatly exceeds I_p, completely suppressing the Coulomb barrier that originally confined the electron. The electron leaks away from the ion directly into continuum states, rapidly accelerating due to the strong laser field. The ionization rate in this regime can be large enough to completely populate the ion species within a few cycles of the driving laser.

Tunneling ionization is the relevant regime for the purposes of HHG, as will be evident by the discussion in Sections 1.3 and 1.4.

Keldysh calculated the ionization rate $\omega_{Keldysh}$ for the hydrogen atom in the quasi-static limit [55], which was later extended to more complex atoms and electronic states by Ammosov, Delone and Krainov. The resulting ADK ionization rate ω_{ADK} of an atom or ion can be calculated using the following equations in atomic units (adapted from [4]):

$$n^* = \frac{\bar{Z} q_e^2}{\hbar} \sqrt{\frac{m_e}{2\mathcal{E}_0}} \tag{1.5}$$

$$\beta_{ADK} = \frac{2(2\mathcal{E}_0)^{3/2}}{3} \tag{1.6}$$

$$\alpha_{ADK} = \frac{\mathcal{E}_0}{2\pi n^*} \frac{(2l+1)(l+|m|)!}{2^{|m|}|m|!(l-|m|)!} \left(\frac{2e}{n^*}\right)^{2n^*} (3\beta_{ADK})^{2n^*-|m-1|} \tag{1.7}$$

$$\omega_{ADK}(t) = \alpha_{ADK} E(t)^{1+|m|-2n^*} exp\left[-\frac{\beta_{ADK}}{E(t)}\right] * F_{BS}(t) \tag{1.8}$$

where in au, $\hbar = 1$, $m_e = 1$, and $q_e = 1$ (not to be confused with e, the natural Euler number). $\bar{Z}$ is the charge state of the resulting ion, $\mathcal{E}_0$ is the ionization potential of the atom/ion (in hartree), l and m are the orbital quantum number and its projection for the electron being ionized, $E(t)$ is the electric field strength of the laser (in au), and F_{BS} is a modification factor that must be included when the barrier-suppression regime is approached ($\gamma_{Keldysh} << 1$) [163]:

$$F_{BS}(t) = exp\left[-\alpha_{BS} \frac{\bar{Z}^2}{\mathcal{E}_0} \frac{E(t)}{(2\mathcal{E}_0)^{3/2}}\right] \tag{1.9}$$

where α_{BS} is a fitting parameter used by Tong and Lin in [163] to match calculated ionization rates in the barrier-suppressed regime using the single-active electron approximation (see Table 1.2 for values of α_{BS}). Without F_{BS}, the ADK ionization formula would overestimate the ionization rate in the barrier-suppressed regime and would therefore only be valid in the tunneling regime. The addition of F_{BS} maintains the simplicity of the ADK formulation while extending the applicable range of the model.

Equation (1.8) represents the instantaneous ionization rate of the atomic or ionic medium by the laser. For the case of neutral atoms being singly-ionized to the first ionic state, the time-

Table 1.2: Some values of the fitting parameter α_{BS} for various atomic and ionic species, including critical field strengths E_{cr} and ionization potentials $\mathcal{E}_0$ (in au). Adapted from Table 2 in [163].

	Rb	H	He	Ar	Ar^+	Ne	Ne^+
α_{BS}	6.0	6.0	6.0	9.0	8.0	9.0	8.0
E_{cr}	0.006	0.063	0.204	0.084	0.129	0.157	0.285
$\mathcal{E}_0$	0.154	0.500	0.904	0.579	1.016	0.793	1.506

dependent ionization population fraction $\eta_{ADK}(t)$ can be simply calculated through integration:

$$\eta_{ADK}(t) = 1 - exp\left[-\int_{-\infty}^{t} \omega_{ADK}(\tau)d\tau\right] \tag{1.10}$$

For media that become multiply-ionized by a single laser pulse, one must use a more complex calculation that accounts for the simultaneous population and depopulation of each ionic species. To approach the multiple-ionization case, we define $\eta_0(t)$ as the time-dependent population of neutral atoms, while $\eta_i(t)$ represents the population of ion species i. The rate at which electrons are ionized from species $i-1$ into species i is given by $\omega_i(t)$ (each of which will depend on the i^{th} ionization potential $\mathcal{E}_i$, the particular electron's quantum numbers l and m, and the resulting charge state $\bar{Z}$). The neutral atom population can be calculated simply from the rate at which the first ionization species becomes populated:

$$\eta_0(t) = exp\left[-\int_{-\infty}^{t} \omega_1(\tau)d\tau\right] \tag{1.11}$$

Thus, the neutral population starts at unity and decreases as electrons are removed to populate the singly-ionized state $\eta_1(t)$. However, the population and depopulation of the first ionization species is more complicated since it depends not only on transitions from the neutral species, but also on transitions into the second ionization species. For the first ionization species, the population is given by an adjusted form of Eq.(1.10):

$$\eta_1(t) = [1 - \eta_0(t)]\ exp\left[-\int_{-\infty}^{t} \omega_2(\tau)d\tau\right] \tag{1.12}$$

For an arbitrary species i, this equation can be generalized:

$$\eta_i(t) = \left[1 - \sum_{k=1}^{i} \eta_{i-k}(t)\right] exp\left[-\int_{-\infty}^{t} \omega_{i+1}(\tau)d\tau\right] \tag{1.13}$$

This formula is self-referencing, since the definition needs to be re-implemented to solve for each $\eta_{i-k}(t)$ until the neutral state ($i = k$) is reached. In other words, to solve for $\eta_5(t)$, it is first necessary to solve for $\eta_4(t)$, and so on. The total ionization population fraction $\eta_{tot}(t) = \sum_{i=1}^{Z_{atom}} i * \eta_i(t)$ can also exceed 100%, indicating more free electrons than ions in the resulting plasma.

1.2.2 Step 2: Propagation

Once the electron is ionized, it quickly escapes the short-range potential of the ion (several r_B) whereupon the laser potential dominates. The motion of the electron following ionization can be classically modeled. Using a z-propagating plane-wave for the laser field with a polarization direction along the y-axis, the electric field is:

$$\boldsymbol{E}_L(\boldsymbol{r}, t) = E_{L0}\cos(\omega_L t - kz + \phi_0)\hat{\boldsymbol{y}} \tag{1.14}$$

where ϕ_0 is the phase of the field at the time of ionization. The magnetic component of the laser field takes on a similar form:

$$\boldsymbol{B}_L(\boldsymbol{r}, t) = -\frac{E_{L0}}{c}\cos(\omega_L t - kz + \phi_0)\hat{\boldsymbol{x}} \tag{1.15}$$

As a result, the Lorentz force governing the motion of the ionized electron is:

$$\boldsymbol{F}(t) = \frac{d\boldsymbol{p}(t)}{dt} = q_e\left[\boldsymbol{E}_L(t) + \boldsymbol{v}(t) \times \boldsymbol{B}_L(t)\right] = q_e E_{L0}\left[\hat{\boldsymbol{y}} - \frac{\boldsymbol{v}(t)}{c} \times \hat{\boldsymbol{x}}\right]\cos(\omega_L t - kz + \phi_0) \tag{1.16}$$

The non-relativistic ($|\boldsymbol{v}(t)| << c$) equations of motion at z = 0 are then:

$$\begin{aligned} \boldsymbol{a}(t) &= \frac{q_e}{m_e} E_{L0}\left[\hat{\boldsymbol{y}} - \frac{\boldsymbol{v}(t)}{c} \times \hat{\boldsymbol{x}}\right]\cos(\omega_L t + \phi_0) \\ &\cong \frac{q_e}{m_e} E_{L0}\cos(\omega_L t + \phi_0)\hat{\boldsymbol{y}} \end{aligned} \tag{1.17}$$

$$\boldsymbol{v}(t) \cong \frac{q_e}{m_e \omega_L} E_{L0}[\sin(\omega_L t + \phi_0) - \sin(\phi_0)]\hat{\boldsymbol{y}} + \boldsymbol{v}_0 \tag{1.18}$$

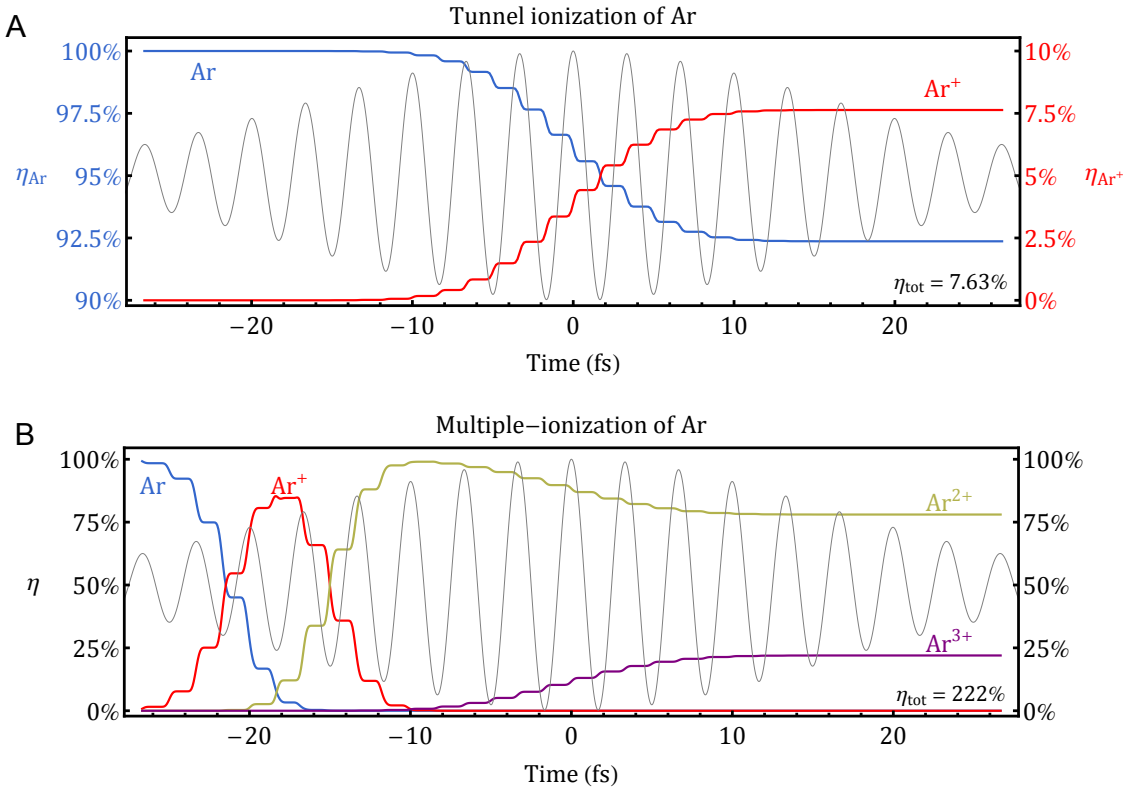

Figure 1.7: Ionization populations for different ion species of Ar plotted as a function of time. The driving laser pulse (shown in gray) has a wavelength of 1 µm and an 8-cycle pulse duration. (A) The low intensity case ($I_L = 1.8 \times 10^{14}$ W/cm^2, $\gamma_{Keldysh} = 0.69$, $E/E_{cr} = 0.85$) where Ar becomes lightly tunnel-ionized; relevant for HHG from atoms. (B) The high intensity case ($I_L = 3.0 \times 10^{15}$ W/cm^2, $\gamma_{Keldysh} = 0.17$, $E/E_{cr} = 3.5$) where Ar becomes multiply-ionized in the barrier-suppressed regime; relevant for HHG from ion species [134].

$$\boldsymbol{x}(t) \cong -\frac{q_e}{m_e\omega_L^2}E_{L0}[\cos(\omega_L t+\phi_0)+\omega_L \sin(\phi_0)t-\cos(\phi_0)]\hat{\boldsymbol{y}}+\boldsymbol{v}_0 t+\boldsymbol{x}_0 \tag{1.19}$$

Typically, the initial displacement of the electron $\boldsymbol{x}_0$ is assumed to be small (i.e. zero), but the initial velocity $\boldsymbol{v}_0$ can be nonzero depending on the initial momentum state of the electron before ionization. Note that in the above derivation, the magnetic component of the Lorentz force (which would tend to accelerate the electron in the +z direction) was assumed to be negligible due to the non-relativistic assumption. In cases where the electron velocity becomes comparable to the speed of light, this component cannot be ignored, as will be discussed in Chapter 4. However, for the purposes of recollision processes like HHG, the non-relativistic assumption is semi-classically valid for laser intensities $< 10^{15}$ W/cm^2 and wavelengths < 5 µm.

For the following analyses, assume the electron starts at rest at the origin. Its trajectory can be plotted for a variety of ionization phases ϕ_0, as shown in Fig. 1.8. Only ionization phases within $[0, \pi/2)$ give trajectories that return to the origin, leading to recollisions.

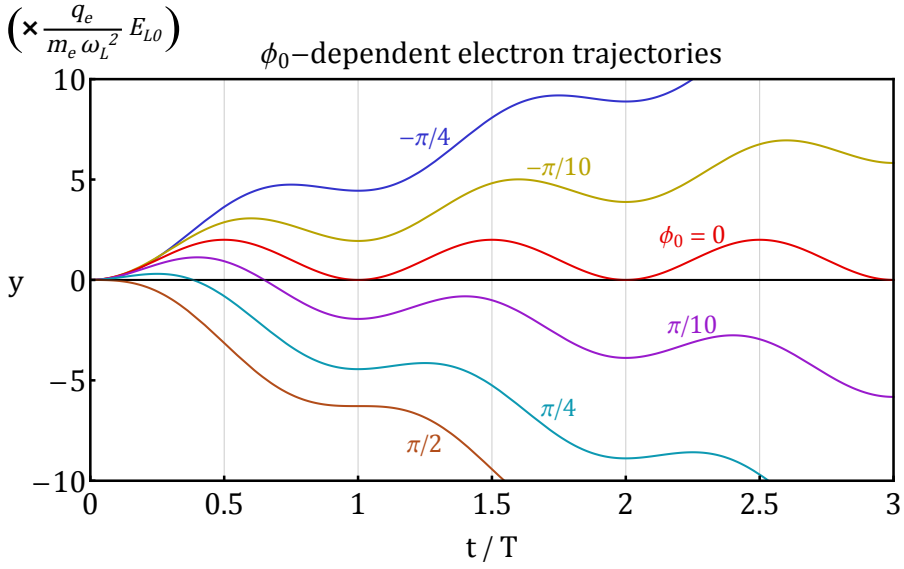

Figure 1.8: Electron trajectories for a variety of ionization phases. The electron returns to its starting position only for $\phi_0 \in [0, \pi/2)$.

For returning trajectories, the amount of time the electron spends away from the ion (τ_f)

cannot be exactly solved for all values of ϕ_0, since setting Eq. (1.19) to zero forms a transcendental equation with only the trivial solution $t = 0$. Of course, numerical methods may be used. However, for the special case of $\phi_0 = 0$, the exact solution is easily calculated to be $\tau_f = \lambda/c = T$, the laser period. Additionally, for $\phi_0 = \pi/2$, the solution is $\tau_f = 0$. Approximate solutions can be found for ionization phases close to 0 and $\pi/2$ (i.e. $\phi_0 = \varepsilon$ and $\phi_0 = \pi/2 - \varepsilon$, where ε is small). In these regimes, the sinusoidal terms may be Taylor expanded. Keeping only the first two terms in the expansions for sine and cosine gives an equation with orders up to ε^3, which yields the following approximate forms for $\tau_f(\phi_0)$:

$$\begin{aligned} \tau_f(\phi_0 < \pi/30) &\cong \frac{12\pi - \phi_0^3 - \sqrt{\phi_0^6 - 24\pi\phi_0(\phi_0^2 - 6)}}{12\pi}\, T \\ \tau_f(\phi_0 > \pi/3) &\cong \frac{3(\pi/2 - \phi_0)}{2\pi}\, T \end{aligned} \tag{1.20}$$

These approximations are valid with less than 1% error for the phase ranges listed, as evidenced by their plots compared to the numerical solution for $\tau_f(\phi_0)$ shown in Fig. 1.9. Note that Taylor expanding out to the first three terms of the sinusoidal functions (orders up to ε^5) yields a much more complicated solution that partially extends the phase ranges where the approximations are valid, but does not impart any additional scientific insight.

With τ_f solved for, the electron's velocity at the time of recollision can be calculated by inserting the values of ϕ_0 and $\tau_f(\phi_0)$ into Eq. (1.18). The kinetic energy of the electron at recollision is then:

$$E_{kinetic}(\tau_f) = \frac{m_e|\boldsymbol{v}(\tau_f)|^2}{2} = 2U_p\left[\sin(\omega_L\tau_f(\phi_0) + \phi_0) - \sin(\phi_0)\right]^2 \tag{1.21}$$

where the ponderomotive potential U_p from Eq. (1.4) was substituted. Equation (1.21) is plotted in Fig. 1.10, showing a maximum value [2] of $3.17U_p$ for an electron ionized around $\phi_0 \approx \pi/10$. This phase marks a division between electron trajectories labeled "long" ($0 < \phi_0 < \pi/10$) and "short" ($\pi/10 < \phi_0 < \pi/2$), simply due to the relative duration of their excursions with respect to the peak energy scenario. Long and short trajectories do result in different quantum and macroscopic physics, as will be discussed in Sections 1.3 and 1.4.

[2] The electron can achieve a kinetic energy $> 3.17U_p$ during its trajectory (up to $8U_p$ if $\phi_0 \approx \pm\pi/2$), but the electron is far from its parent ion when it achieves these higher energies.

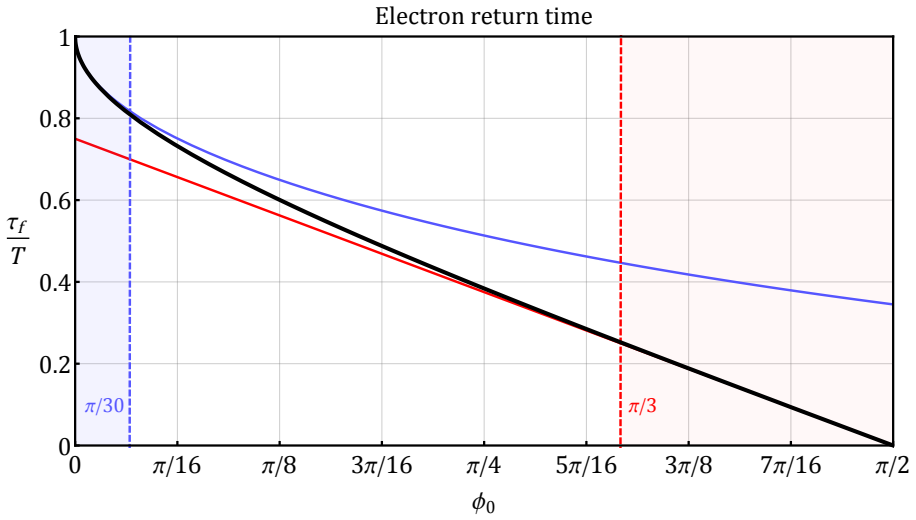

Figure 1.9: The amount of time τ_f an electron spends away from the ion before returning to its starting position, plotted as a function of ionization phase ϕ_0. Only phases within $[0, \pi/2)$ are considered since all other phases result in non-returning trajectories. The solid black line is the numerical solution, while the solid red and blue lines represent the approximate solutions from Eq. (1.20). The shaded regions indicate the phases where the approximate solutions have less than 1% error.

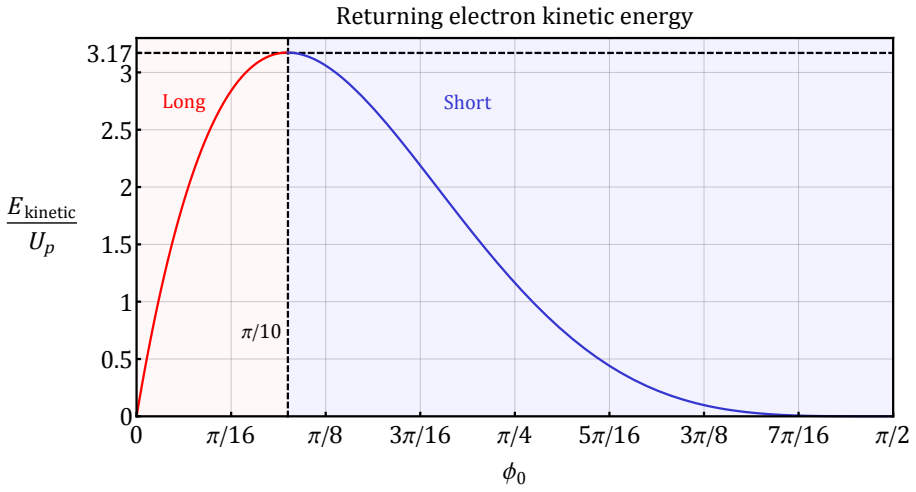

Figure 1.10: The kinetic energy $E_{kinetic}$ of the recolliding electron, plotted as a function of ionization phase ϕ_0. A maximum value of $3.17U_p$ occurs for $\phi_0 \approx \pi/10$. Electrons ionized before this phase (long trajectories) and those ionized after this phase (short trajectories) have reduced energy upon recollision.

At the time of recollision, the electron can recombine with the ion and enter the ground state, causing it to release its kinetic energy combined with the ionization potential I_p of the atom, leading to the HHG single-atom cutoff energy rule:

$$E_{SAC} = I_p + 3.17U_p \tag{1.22}$$

This key equation results from a purely classical analysis of the electron's motion following ionization, and it represents the highest photon energy that can be emitted via the HHG process from a single atom under monochromatic, linearly-polarized illumination.

Note that the above calculations assumed the electron started at rest. Had the electron been ionized with residual momentum from its bound state, its motion would be identical except with a linear drift in time. This drift points in the direction of $\boldsymbol{v}_0$, which can result in electrons returning to the origin for ionization phases outside $\phi_0 \in [0, \pi/2)$ if $\boldsymbol{v}_0 \parallel \hat{\boldsymbol{y}}$, the polarization direction. Furthermore, there exist alternative driving field configurations that allow the electron to take returning trajectories, such as bichromatic, bicircular driving fields used to produce circularly-polarized harmonics [154, 130, 129, 128].

1.2.3 Step 3: Recombination

As described in the previous section, the recombination step provides the mechanism for the electron to release its kinetic energy through photon emission. Whether or not a photon is released depends on a number of factors. The following must occur:

(1) Ionization of the electron must occur.

(2) The electron must return to the vicinity of its parent ion.

(3) Upon recollision with the ion, the electron must recombine with the ion, re-entering the ground state.

The first two items have been discussed in this semi-classical analysis, but the recombination pathway is only one of several options that the electron can take. In general, a recollision can also

result in:

- **Above-threshold ionization**: The electron absorbs more photons than necessary to become ionized, leaving it in a continuum state with non-zero kinetic energy [3, 9, 32].
- **Elastic backscattering**: The ionized electron recollides with the ion, scattering elastically backward and leaving the system as an energetic free electron [95].
- **Inelastic excitation**: The ionized electron recollides with the ion and imparts some of its kinetic energy to a remaining bound electron by scattering inelastically, thus exciting the bound electron to an excited state [29].
- **Non-sequential double ionization**: The ionized electron recollides with the ion at high energy, imparting $> I_p$ of its energy to a bound electron such that the second electron also becomes ionized [75, 39].

Figure 1.11 depicts each of these processes in addition to the HHG pathway. The cross sections for each of these processes vary; for HHG, a quantum mechanical treatment is required and will be presented in Section 1.3. Should the electron take the HHG pathway and recombine with ion, its total energy changes:

$$E_{tot,0} = E_{kinetic,0} + \cancelto{0}{V_0} \quad \longrightarrow \quad E_{tot,f} = -I_p \tag{1.23}$$

which leads to the emission of a photon with energy $E_{ph} = -(E_{tot,f} - E_{tot,0})$, limited by the single atom cutoff energy, presented in Eq. (1.22). Some ionization potentials are listed in au as $\mathcal{E}_0$ in Table 1.2, and in electron-volts as I_p in Table 1.3.

1.2.4 Characteristics of Microscopic HHG Emission

The harmonic emission that results from the HHG three step process has properties and limitations that are inherent to the microscopic picture. Already, a spectral limitation for HHG has been presented through the derivation of the single-atom cutoff energy described in Eq. (1.22).

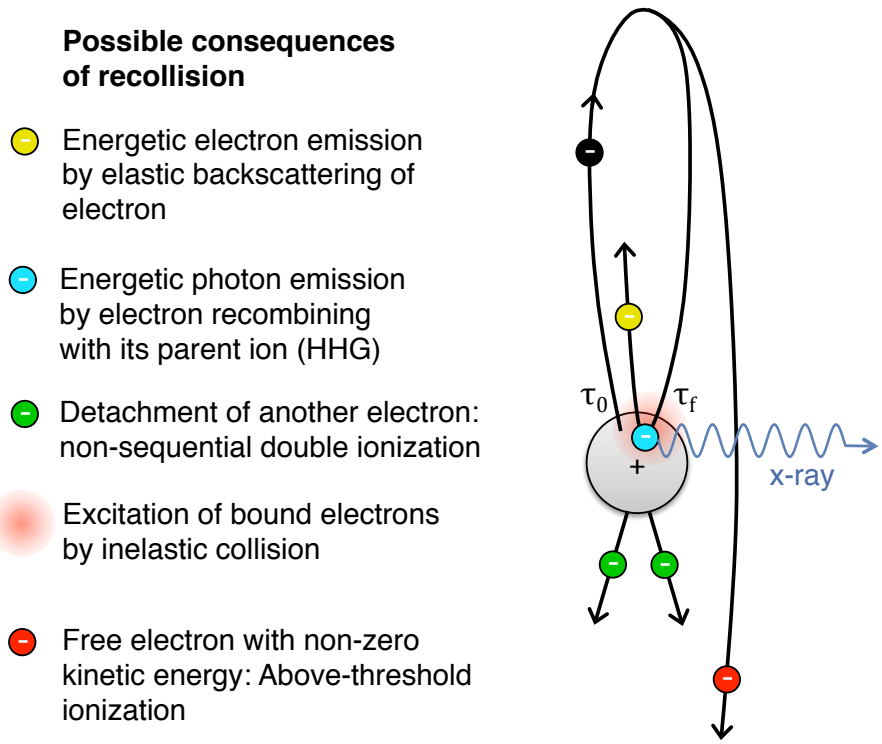

Figure 1.11: Several processes observed in electron-ion recollisions following ionization. Only HHG results in photon emission, while all other processes result in one or more free electrons and an ion species. In the figure, τ_0 and τ_f refer to the times when the electron is born and when it returns to the ion, respectively. Adapted from [19].

Table 1.3: Ionization potentials I_p (in eV) for various gases and their ionic species. Data obtained from [71]. Ionization potentials beyond first ionization can be important for HHG from ions, as demonstrated in [134].

	I_p (eV)						
	$X \rightarrow X^+$	$X^+ \rightarrow X^{2+}$	$X^{2+} \rightarrow X^{3+}$	$X^{3+} \rightarrow X^{4+}$	$X^{4+} \rightarrow X^{5+}$	$X^{5+} \rightarrow X^{6+}$	$X^{6+} \rightarrow X^{7+}$
H	13.6						
He	24.59	54.42					
Ne	21.56	40.96	63.45	97.11	126.21	157.93	207.26
Ar	15.76	27.63	40.74	59.81	75.04	91.01	124.4
Kr	14.00	24.36	36.95	52.5	64.7	78.5	111
Xe	12.13	21.21	32.1	46	57	82	100
N	14.53	29.60	47.45	77.47	97.89	552.06	667.03

In essence, the maximum harmonic energy achievable from HHG is determined by the ionization potential of the medium as well as the driving laser's intensity and wavelength. An additional property in the spectral domain is the scaling of harmonic flux with harmonic order; at low orders, the exponential scaling typical of perturbative effects is observed, but at large orders, there is non-perturbative behavior indicated by the plateau of harmonics extending to the cutoff energy (Fig. 1.4). Only the three step model of HHG explains these qualities.

With regards to the time domain, only the electron motion has been discussed. However, the electron is at the core of the HHG process, and the harmonic output is therefore dependent on its behavior. In particular, harmonic emission occurs at the time the electron recombines with its parent ion - some time after the electron is first ionized. If the electron is ionized at a phase $\phi_0 \in [0, \pi/2)$, then it will recombine and emit a photon at a later phase $\phi_f \in (\pi/2, 2\pi]$. Take note that the laser field amplitude is periodic, such that the non-relativistic [3] physics that takes place within a given half-cycle should be repeated for the following half-cycle, except with a change of sign. This necessarily results in the possibility of harmonic emission occurring every half-cycle of the driving laser field. For an ensemble of emitters, the averaged microscopic result would be a pulse train of harmonics with temporal spacing $\frac{\lambda}{2c}$. This pulse train would last for the duration dt of the driving laser, while the intensity is large enough to tunnel ionize ($\gamma_{Keldysh} < 1$) and the ionization level remains unsaturated ($\eta_{ADK} < 1$). Each individual harmonic pulse would have a duration less than a half-cycle of the driving field ($dt_{HHG} < \frac{\lambda}{2c}$).

The $\frac{\lambda}{2c}$ periodicity of the harmonic pulses in the time domain generates interferences in the spectral domain. Without the interferences (i.e. considering the emission from only a single half-cycle) the HHG spectrum would be a broad supercontinuum extending from the fundamental frequency ω_L to the single-atom cutoff energy (many harmonic orders higher). With the interference from the neighboring pulses, however, the supercontinuum becomes modulated with peaks occurring at every odd harmonic of the fundamental. The separation of $2\omega_L$ between each peak is a direct

[3] Note that for relativistic cases ignored in Section 1.2, the half-cyclic symmetry can be broken. These cases will be investigated in Chapter 4

result of the $\frac{\lambda}{2c}$ periodicity in the time domain. The peaks occur at every odd harmonic (as opposed to every even harmonic) due to the relative phases of each pulse in the harmonic pulse train. The emission from electrons ionized during an up half-cycle - $\phi_0 \in [0, \pi/2)$ - is followed by emission from electrons ionized during a down half-cycle - $\phi_0 \in [\pi, 3\pi/2)$. The opposing signs of the fields and trajectories result in a π phase shift between neighboring harmonic pulses, which in turn results in the odd harmonics that are observed experimentally. Figure 1.12 provides a qualitative depiction of these phenomena, while Fig. 1.13 contains measured data of HHG in the time and frequency domains. The spectral and temporal characteristics of HHG can be modified either through breaking of the half-cycle symmetries, or through adjusting the driving laser waveform in the time domain. For instance, emission of an isolated harmonic pulse is possible by driving HHG with a single-cycle laser pulse ($dt \approx \lambda/c$) [22, 140, 137].

Another important property of the harmonic beam in the time domain is the chirp rate of each pulse. As a result of the three step model, electrons ionized at different times within the pulse will recombine at different times and emit harmonics of different energies. From the analyses performed in Section 1.2.2, the spectral phase (and thus the various orders of chirp/dispersion) can be calculated. Dispersive orders tend to increase the duration of a pulse, thus imposing a limitation on the pulse duration achievable via HHG without using compression techniques (which can be difficult and inefficient in the EUV and soft X-ray regimes). Figure 1.14 contains plots of the group delay dispersion ($GDD = \frac{d^2\phi}{d\omega^2}$) and third-order dispersion ($TOD = \frac{d^3\phi}{d\omega^3}$). The GDD has the largest effect on the pulse duration, while higher orders can be largely neglected.

Finally, the spatial and angular characteristics of the harmonic emission can also be deduced from the electron motion. In this microscopic picture, the size of the photon source would obviously be no larger than the size of the atom. As for the direction of photon emission, the electron's acceleration vector gives a clue. Accelerating charged particles radiate light, according to the Larmor formulation:

$$\frac{dP(t)}{d\Omega} = \frac{q_e^2}{4\pi c}\frac{\sin^2(\theta)a^2(t)}{c^2} \tag{1.24}$$

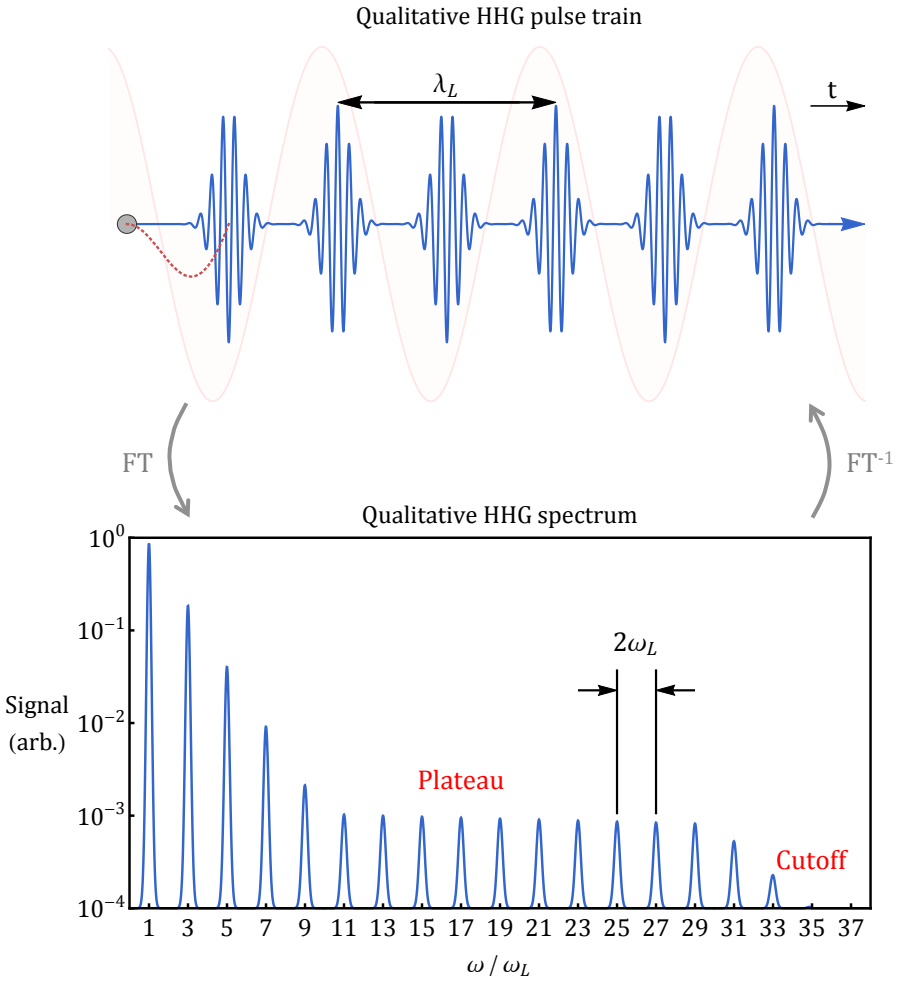

Figure 1.12: Plots of the qualitative characteristics of HHG in the time and frequency domains. The spacing of the pulses in time result in a $2\omega_L$ spacing of peaks in the spectrum. The absolute positions of the spectral peaks is governed by the relative phases of neighboring pulses in the time domain. Odd harmonics are naturally generated for non-relativistic HHG using monochromatic drivers.

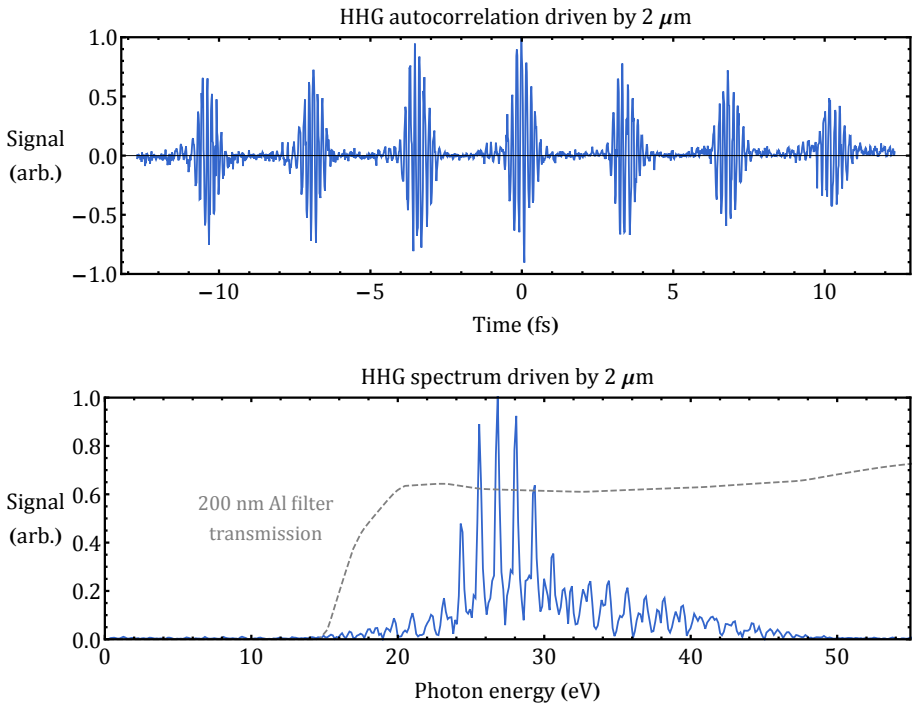

Figure 1.13: Plots of the measured signal in the time and frequency domains for HHG driven by $\lambda = 2$ µm at low intensity and transmitted through an Al filter. An electric field autocorrelation of the HHG pulse train is presented for the time domain, whose Fourier transform directly gives the spectrum (Chapter 2, [18]). Attosecond streaking methods are otherwise required to indirectly measure the HHG pulse train, as opposed to its autocorrelation [144]. Note that macroscopic effects (Section 1.4) apply here.

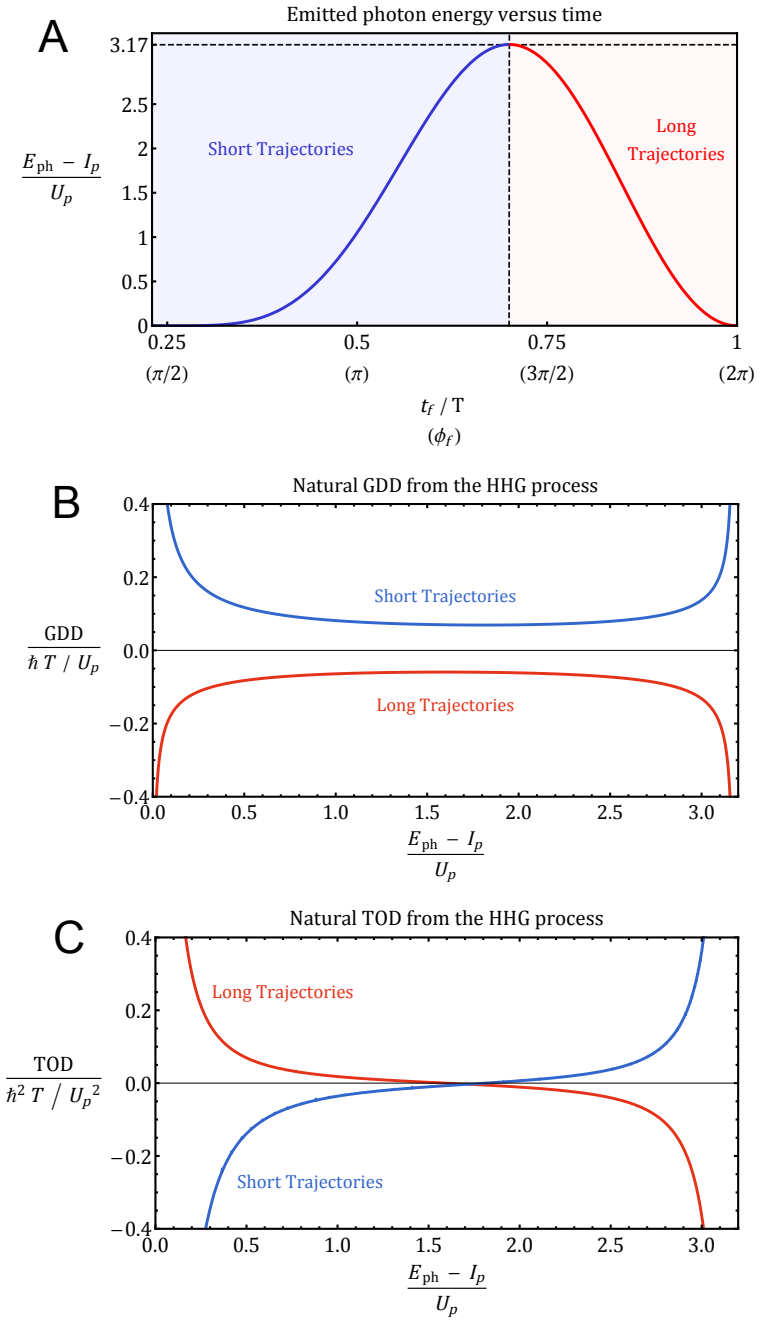

Figure 1.14: Plots showing the dispersion of natural HHG emission. (A) A plot of the energy of the emitted photon for an electron returning to the ion at a final time t_f, corresponding to a final phase ϕ_f. (B) and (C) Plots of the normalized group delay dispersion (GDD) and third-order dispersion (TOD) that result from the three step model of HHG. These are used in Taylor expansions for the spectral phase, and tend to increase the durations of the harmonic pulses unless compensated for through compression techniques. Note that the atom's ionization potential has no effect on the microscopic dispersion, but would only shift the curves uniformly along the energy axis.

$$P(t) = \frac{2}{3}\frac{q_e^2 a^2(t)}{c^3} \tag{1.25}$$

Here, θ is the angle between the acceleration and observation vectors. Equation (1.17) gives the acceleration of the electron, but under the influence of the driving laser field only, which would result in the electron radiating at the same fundamental frequency. It is the recollision with the ion that causes the electron to radiate at higher frequencies, so it is the impulsive acceleration upon recombination that must be considered. In terms of quantitave power radiated, the classical acceleration upon recollision is difficult to calculate, since the rate at which the electron stops to recombine is not readily deduced. Scattering theory can be used, but gives a result that is highly dependent on the impact parameter. The quantum mechanical treatment in Section 1.3 provides a more intuitive and straightforward calculation for the quantitative power radiated. Fortunately, the qualitative direction of the acceleration upon recollision is obvious, and therefore the emission pattern would follow the $\sin^2(\theta)$ scaling in Eq. (1.24), with θ being the angle measured from the $\hat{\boldsymbol{y}}$-direction. For a single atom, the harmonic emission is brightest in the x-z plane, while there is zero emission along the $\hat{\boldsymbol{y}}$ direction. Figure 1.15 depicts this microscopic radiation pattern. Despite the broad angular distribution for single atom radiation, macroscopic effects reduce the total beam divergence (see Section 1.4).

1.3 Quantum Mechanical Picture of HHG

The semi-classical analysis of microscopic HHG presented in Section 1.2 is a valid approach to derive the primary characteristics of the harmonic emission. A quantum approach should yield the same physical conclusions, but can give deeper insight into the process from the viewpoint of the electron wavefunction. Ensemble averages, which are relevant to realistic laboratory conditions with many atoms, can be derived directly from the quantum perspective.

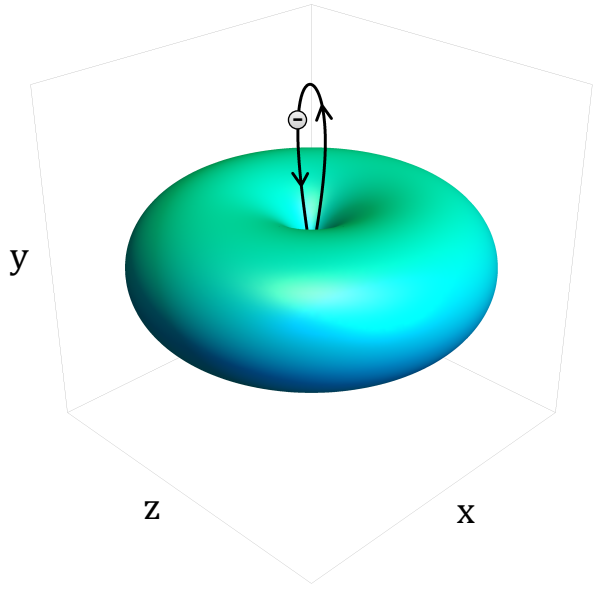

Figure 1.15: Depiction of the Larmor radiation pattern following the $\sin^2(\theta)$ scaling from Eq. (1.24). The power is primarily radiated along the x-z plane, with zero emission directly along $\hat{\boldsymbol{y}}$. Microscopically, HHG would be emitted with this broad angular distribution, but macroscopic effects enhance the emission along the laser propagation direction $\boldsymbol{k} \parallel \hat{\boldsymbol{z}}$.

1.3.1 The Quantum Three Step Model

The quantum derivation for the three step model is found in [68] and is reproduced here. The general approach is to solve the time-dependent Schrödinger equation while treating the electron's wavefunction as a sum of the bound state and ionized states in the continuum. By solving for the continuum states, the dipole radiation at the time of recombination can be solved for.

The electron's wavefunction obeys the time-dependent Schrödinger equation:

$$i\hbar\frac{\partial\left|\Psi(\boldsymbol{r},t)\right\rangle}{\partial t}=\left[\frac{-\hbar^2}{2m_e}\nabla^2+V(\boldsymbol{r},t)\right]\left|\Psi(\boldsymbol{r},t)\right\rangle, \tag{1.26}$$

where $\left|\Psi(\boldsymbol{r},t)\right\rangle = e^{-iEt/\hbar}\left|\psi(\boldsymbol{r})\right\rangle$ is the electron's wavefunction, and $V(\boldsymbol{r},t)$ is the total potential experienced by the electron. $\left|\psi(\boldsymbol{r})\right\rangle$ satisfies the time-independent Schrödinger equation:

$$\left[\frac{-\hbar^2}{2m_e}\nabla^2+V(\boldsymbol{r},t)\right]\left|\psi(\boldsymbol{r})\right\rangle = E\left|\psi(\boldsymbol{r})\right\rangle \tag{1.27}$$

Prior to the laser field, the electron is in the atomic ground state $\left|\psi(\boldsymbol{r})\right\rangle = \left|0\right\rangle$ with energy $E_0 = -I_p$, confined by only the atomic Coulomb potential $V_{atomic}(\boldsymbol{r})$, which in the simplest case is given by Eq. (1.1).

In the presence of the laser field, an additional potential arises. For a linearly-polarized laser field aligned along the $\hat{\boldsymbol{y}}$ direction:

$$V_{laser}(\boldsymbol{r},t) = -q_e E_{L0}\cos(\omega_L t)\, y \tag{1.28}$$

The time-dependent Schrödinger equation then becomes:

$$i\hbar\frac{\partial\left|\Psi(\boldsymbol{r},t)\right\rangle}{\partial t}=\left[\frac{-\hbar^2}{2m_e}\nabla^2+V_{atomic}(\boldsymbol{r},t)-q_e E_{L0}\cos(\omega_L t)\, y\right]\left|\Psi(\boldsymbol{r},t)\right\rangle \tag{1.29}$$

At this point, the following assumptions are necessary to proceed:

(1) Only the $\left|0\right\rangle$ bound state contributes to the the evolution of the atomic system, while all other states' contributions are neglected.

(2) The depletion of the $\left|0\right\rangle$ state is ignored, indicating ionization fractions $\eta << 1$.

(3) Once the electron ionizes to a continuum state $|\boldsymbol{p}\rangle$, the short-range atomic potential $V_{atomic}(\boldsymbol{r})$ no longer acts on it (strong-field approximation).

The validity of the assumptions are generally good for Keldysh parameters $\gamma_{Keldysh} < 1$, but for intensities less than the saturation intensity. Note that the continuum states satisfy Eq. (1.26) with the form:

$$|\Psi_{\boldsymbol{p}}\rangle = e^{-iE_p t/\hbar}\,|\boldsymbol{p}\rangle = Ae^{i(\boldsymbol{k}\cdot\boldsymbol{r}-\omega_p t)} = Ae^{i(\boldsymbol{p}\cdot\boldsymbol{r}-E_P t)/\hbar}, \tag{1.30}$$

where $\boldsymbol{p} = m_e\boldsymbol{v}$ is the momentum of the electron, $E_p = \frac{p^2}{2m_e}$ is its energy, $\boldsymbol{k} = \frac{\boldsymbol{p}}{\hbar} = \frac{2\pi}{\lambda_D}\hat{\boldsymbol{v}}$ is its wavevector, λ_D is the DeBroglie wavelength, and $\omega_p = \frac{E_p}{\hbar} = \frac{\hbar k^2}{2m_e} = \frac{\pi v}{\lambda_D}$.

With the assumptions, the total wavefunction of the electron can be decomposed into bound and continuum components as follows:

$$|\Psi(\boldsymbol{r},t)\rangle = e^{iI_p t/\hbar}\left[a(t)\,|0\rangle + \int d^3\boldsymbol{p}\;\; b(\boldsymbol{p},t)\,|\boldsymbol{p}\rangle\right] \tag{1.31}$$

where $a(t)$ represents the time-dependent proportion of the wavefunction that stays in the ground state, and $b(\boldsymbol{p},t)$ represents the proportion that ionizes and enters the continuum state with momentum $\boldsymbol{p}$. [4] Note that the phase $e^{iI_p t/\hbar}$ is factored, shifting the energy of the ground state $|0\rangle$ to zero and the energy of the continuum states up to $\frac{p^2}{2m_e} + I_p$. Ignoring the ground state depletion $a(t) \cong 1$, the left-hand side of the time-dependent Schrödinger equation becomes:

$$i\hbar\frac{\partial}{\partial t}\,|\Psi(\boldsymbol{r},t)\rangle = -I_p\,|\Psi(\boldsymbol{r},t)\rangle + i\hbar e^{iI_p t/\hbar}\int d^3\boldsymbol{p}\;\; \dot{b}(\boldsymbol{p},t)\,|\boldsymbol{p}\rangle \tag{1.32}$$

With the substitution of Eq. (1.31) and using the fact that the atomic potential $V_{atomic}(\boldsymbol{r})$ acting on the phase-shifted continuum states results in $-I_p\,|\boldsymbol{p}\rangle$, the right-hand side of the time-dependent Schrödinger equation is:

$$\begin{aligned} H\,|\Psi(\boldsymbol{r},t)\rangle = &-I_p\,|\Psi(\boldsymbol{r},t)\rangle - e^{iI_p t/\hbar}q_e E_{L0}\cos(\omega_L t)\,y\,a(t)\,|0\rangle \\ &+ e^{iI_p t/\hbar}\int d^3\boldsymbol{p}\;\; \left(\frac{p^2}{2m_e} + I_p\right) b(\boldsymbol{p},t)\,|\boldsymbol{p}\rangle \\ &- e^{iI_p t/\hbar}q_e E_{L0}\cos(\omega_L t)\,y\int d^3\boldsymbol{p}\;\; b(\boldsymbol{p},t)\,|\boldsymbol{p}\rangle \end{aligned} \tag{1.33}$$

[4] Here, $a(t)$ is unitless, while $b(\boldsymbol{p},t)$ has units of $[p^{-3}]$.

Putting together the two sides of the time-dependent Schrödinger equation results in the cancellation of the terms $-I_p\,|\Psi(\boldsymbol{r},t)\rangle$ and $e^{iI_pt/\hbar}$. Additionally, the y operator can be expressed in momentum space as $i\hbar\frac{\partial}{\partial p_y}$. The result is:

$$\begin{aligned} i\hbar\int d^3\boldsymbol{p}\;\; \dot{b}(\boldsymbol{p},t)\,|\boldsymbol{p}\rangle = &-q_eE_{L0}\cos(\omega_Lt)\,y\,a(t)\,|0\rangle \\ &+\int d^3\boldsymbol{p}\;\; \left(\frac{p^2}{2m_e}+I_p\right)b(\boldsymbol{p},t)\,|\boldsymbol{p}\rangle \\ &-i\hbar q_eE_{L0}\cos(\omega_Lt)\int d^3\boldsymbol{p}\;\; \frac{\partial}{\partial p_y}b(\boldsymbol{p},t)\,|\boldsymbol{p}\rangle \end{aligned} \tag{1.34}$$

Multiplying both sides of the equation by [5] $\int d^3\boldsymbol{p}'\,\langle\boldsymbol{p}'|$:

$$\begin{aligned} i\hbar\dot{b}(\boldsymbol{p},t) = &-\langle\boldsymbol{p}|\,q_eE_{L0}\cos(\omega_Lt)\,y\,|0\rangle + \left(\frac{p^2}{2m_e}+I_p\right)b(\boldsymbol{p},t) \\ &-i\hbar q_eE_{L0}\cos(\omega_Lt)\int d^3\boldsymbol{p}'\,\langle\boldsymbol{p}'|\,\frac{\partial}{\partial p_y}b(\boldsymbol{p},t)\,|\boldsymbol{p}\rangle \end{aligned} \tag{1.35}$$

The product rule is needed for the last term, resulting in:

$$\begin{aligned} \int d^3\boldsymbol{p}'\,\langle\boldsymbol{p}'|\,\frac{\partial}{\partial p_y}b(\boldsymbol{p},t)\,|\boldsymbol{p}\rangle = &\;\frac{\partial b(\boldsymbol{p},t)}{\partial p_y}\int d^3\boldsymbol{p}'\,\langle\boldsymbol{p}'|\boldsymbol{p}\rangle \\ &+b(\boldsymbol{p},t)\int d^3\boldsymbol{p}'\,\langle\boldsymbol{p}'|\,\frac{\partial}{\partial p_y}\,|\boldsymbol{p}\rangle \end{aligned} \tag{1.36}$$

From Eq. (1.30), the derivative of $|\boldsymbol{p}\rangle$ with respect to p_y causes the second term's integrand to be odd, resulting in zero for the integral. Finally, the time-dependent Schrödinger equation for $b(\boldsymbol{p},t)$ takes the form of the Volkov equation:

$$\dot{b}(\boldsymbol{p},t) = -\frac{i}{\hbar}\left(\frac{p^2}{2m_e}+I_p\right)b(\boldsymbol{p},t) - q_eE_{L0}\cos(\omega_Lt)\frac{\partial b(\boldsymbol{p},t)}{\partial p_y} + \frac{i}{\hbar}q_eE_{L0}\cos(\omega_Lt)\,\langle\boldsymbol{p}|\,y\,|0\rangle \tag{1.37}$$

Note that the term $\langle\boldsymbol{p}|\,y\,|0\rangle = d_y(\boldsymbol{p})$ is the atomic dipole matrix element for the bound-free transition parallel to the polarization axis $\hat{\boldsymbol{y}}$. The Volkov equation can be solved exactly using the electromagnetic vector potential, which takes the following form for this electric field in the radiation gauge $\left(\boldsymbol{E}(t) = -\frac{d\boldsymbol{A}(t)}{dt}\right)$:

$$\boldsymbol{A}(t) = \begin{pmatrix} 0 \\ -\frac{E_{L0}}{\omega_L}\sin(\omega_Lt) \\ 0 \end{pmatrix} \tag{1.38}$$

[5] Here, we implicitly assume there is an additional factor with amplitude 1 containing units of $\left[p^{-3}\right]$. This implicit factor will disappear when integrals over $d^3\boldsymbol{p}$ collapse, but would remain for the first term in Eq. (1.35) and its eventual conversion to $d_y(\boldsymbol{p})$, which persists through the calculation.

With the substitution for the canonical momentum ($\bar{\boldsymbol{p}} = \boldsymbol{p} + q_e\boldsymbol{A}(t) = m_e\boldsymbol{v} + q_e\boldsymbol{A}(t)$), the solution for $b(\bar{\boldsymbol{p}}, t)$ is then:

$$b(\bar{\boldsymbol{p}}, t) = \frac{i}{\hbar}\int_0^t dt' q_e E_{L0}\cos(\omega_L t')\, d_y(\bar{\boldsymbol{p}} - q_e\boldsymbol{A}(t'))\, e^{-iS(\bar{\boldsymbol{p}},t,t')} \tag{1.39}$$

where the integral begins at time $t = 0$ (corresponding to the peak of the driving electric field), and $S(\bar{\boldsymbol{p}}, t, t')$ is the semi-classical action:

$$S(\bar{\boldsymbol{p}}, t, t') = \frac{1}{\hbar}\int_{t'}^t dt'' \left[\frac{(\bar{\boldsymbol{p}} - q_e\boldsymbol{A}(t''))^2}{2m_e} + I_p\right] \tag{1.40}$$

At this point in the derivation, we have arrived at a closed form solution for the continuum state amplitudes as a function of time. Recall that the goal of the derivation is to arrive at an equation for the harmonic dipole emission upon recombination. The harmonic electric field will be proportional to the second time-derivative of the dipole:

$$\begin{aligned}\langle\Psi(\boldsymbol{r},t)|\, y\,|\Psi(\boldsymbol{r},t)\rangle = \langle 0|\, y\,|0\rangle &+ \int d^3\boldsymbol{p}\, d^3\boldsymbol{p}'\, b^*(\boldsymbol{p}',t)\,\langle\boldsymbol{p}'|\, yb(\boldsymbol{p},t)\,|\boldsymbol{p}\rangle \\ &+ \int d^3\boldsymbol{p}\,\langle 0|\, yb(\boldsymbol{p},t)\,|\boldsymbol{p}\rangle \\ &+ \int d^3\boldsymbol{p}\, b^*(\boldsymbol{p},t)\,\langle\boldsymbol{p}|\, y\,|0\rangle\end{aligned} \tag{1.41}$$

The first term contains an odd integrand and is therefore zero. The second term concerns transitions between continuum states, which do not contribute to the harmonic emission. The remaining terms are complex conjugates of each other. The component of the dipole that concerns harmonic emission can therefore be written as:

$$\chi(t) = \int d^3\boldsymbol{p}\, b^*(\boldsymbol{p},t)\,\langle\boldsymbol{p}|\, y\,|0\rangle + c.c. = \int d^3\boldsymbol{p}\, b(\boldsymbol{p},t) d_y(\boldsymbol{p}) + c.c. \tag{1.42}$$

Substituting $b(\bar{\boldsymbol{p}}, t)$ from Eq. (1.39) [6] :

$$\chi(t) = \frac{i}{\hbar}\int_0^t dt' \int d^3\bar{\boldsymbol{p}}\, q_e E_{L0}\cos(\omega_L t')\, d_y(\bar{\boldsymbol{p}} - q_e\boldsymbol{A}(t'))\, e^{-iS(\bar{\boldsymbol{p}},t,t')}\, d_y^*(\bar{\boldsymbol{p}} - q_e\boldsymbol{A}(t)) + c.c. \tag{1.43}$$

Equation (1.43) can be physically interpreted in terms of probability amplitudes corresponding to each component of the three-step model. First, the electron is ionized at time t' from a bound

[6] Recall $b(\bar{\boldsymbol{p}}, t)$ contains an implicit factor with units $\left[p^{-3}\right]$, which carries into $\chi(t)$.

state into a continuum state with a probability amplitude: $E_{L0}\cos(\omega_L t)d_y(\bar{\boldsymbol{p}} - q_e\boldsymbol{A}(t'))$. Following ionization, the free electron propagates in the laser field with a constant canonical momentum $\bar{\boldsymbol{p}}$, acquiring a phase equal to the quasi-classical action: $e^{-iS(\bar{\boldsymbol{p}},t,t')}$. Finally, the electron recombines with the ion at time t, transitioning from a continuum state to the bound state with a probability amplitude: $d_y^*(\bar{\boldsymbol{p}} - q_e\boldsymbol{A}(t))$. Note that Eq. (1.43) can be extended to arbitrary polarization and temporal shape. For an electric field of the form $\boldsymbol{E_L}(t)$, the dipole moment along direction $\hat{\boldsymbol{n}}$ is:

$$\chi(t) = \frac{i}{\hbar}\int_0^t dt' \int d^3\bar{\boldsymbol{p}}\, q_e \boldsymbol{E_L}(t') \cdot \boldsymbol{d}(\bar{\boldsymbol{p}} - q_e\boldsymbol{A}(t'))\ \hat{\boldsymbol{n}} \cdot \boldsymbol{d}^*(\bar{\boldsymbol{p}} - q_e\boldsymbol{A}(t))\, e^{-iS(\bar{\boldsymbol{p}},t,t')} + c.c. \tag{1.44}$$

The dipole moment contains an integral over the canonical momentum where the terms in the integrand oscillate rapidly for many values of $\bar{\boldsymbol{p}}$. Because the term $e^{-iS(\bar{\boldsymbol{p}},t,t')}$ oscillates most rapidly, the integral averages to zero except in regions where $\nabla_{\bar{p}}S(\bar{\boldsymbol{p}},t,t') \cong 0$ (which can also be stated as $\boldsymbol{x}(t) - \boldsymbol{x}(t') \cong 0$; i.e. only electrons with trajectories that return to the ion contribute to HHG). Therefore, the result of the integration can be approximated by finding the stationary phases $\bar{\boldsymbol{p}}_s$ of $S(\bar{\boldsymbol{p}})$ and Taylor expanding about them:

$$S(\bar{\boldsymbol{p}}) \cong S(\bar{\boldsymbol{p}}_s) + \frac{1}{2}\nabla_{\bar{p}}^2 S|_{\bar{p}_s}(\bar{\boldsymbol{p}} - \bar{\boldsymbol{p}}_s)^2, \tag{1.45}$$

where $\bar{\boldsymbol{p}}_s$ satisfies $\nabla_{\bar{p}}S(\bar{\boldsymbol{p}}_s,t,t') = 0 \ \rightarrow\ \int_{t'}^t dt''(\bar{\boldsymbol{p}}_s - q_e\boldsymbol{A}(t'')) = 0$. Lumping together the other terms in the integrand as $F(\bar{\boldsymbol{p}})$, and recognizing that $F(\bar{\boldsymbol{p}})$ varies slowly compared to $S(\bar{\boldsymbol{p}})$, the integral over the momentum becomes:

$$F(\bar{\boldsymbol{p}}_s)e^{-iS(\bar{\boldsymbol{p}}_s)}\int d^3\bar{\boldsymbol{p}}\ \ exp\left[-\frac{i}{2}\nabla_{\bar{p}}^2 S|_{\bar{p}_s}(\bar{\boldsymbol{p}} - \bar{\boldsymbol{p}}_s)^2\right] \tag{1.46}$$

This integral is separable into integrals over the three Cartesian directions, each of which can be solved using the same substitution $\pi\xi^2/2 = \nabla_{\bar{p}}^2 S|_{\bar{p}_s}(\bar{p}_x - \bar{p}_{s,x})^2$. Equation (1.46) then takes the following form:

$$F(\bar{\boldsymbol{p}}_s)e^{-iS(\bar{\boldsymbol{p}}_s)}\left(\frac{\pi}{\nabla_{\bar{p}}^2 S|_{\bar{p}_s}}\right)^{3/2}\left[\int_{-\infty}^{\infty} d\xi\ exp\left(-i\pi\xi^2/2\right)\right]^3 \tag{1.47}$$

which contains a Fresnel-type integral with solution $\int_{-\infty}^{\infty} dx\ (\cos(\pi x^2/2) - i\sin(\pi x^2/2)) = i\sqrt{i}$.

Also noting that $\nabla^2_{\bar{p}} S|_{\bar{p}_s} = \frac{(t-t')}{m_e \hbar} = \frac{\tau_f}{m_e \hbar}$, the dipole moment finally becomes [7] :

$$\begin{aligned}\chi(t) = \frac{1}{\hbar}\int_0^t dt' \left(\frac{i\pi m_e \hbar}{\tau_f}\right)^{3/2} q_e \boldsymbol{E_L}(t') \cdot \boldsymbol{d}(\bar{\boldsymbol{p}}_s - q_e \boldsymbol{A}(t')) \\ \times \hat{\boldsymbol{n}} \cdot \boldsymbol{d}^*(\bar{\boldsymbol{p}}_s - q_e \boldsymbol{A}(t))\, e^{-iS(\bar{\boldsymbol{p}}_s, t, t')} + c.c.\end{aligned} \tag{1.48}$$

Calculating $q_e \ddot{\chi}(t)$ will give the harmonic electric field in the time domain, which when Fourier transformed will result in the HHG spectrum. The emission amplitude into the N^{th} harmonic with frequency $N\omega_L$ can be calculated by performing the integral $\int_{-\infty}^{\infty} dt\ q_e \ddot{\chi}(t) e^{-iN\omega_L t}$.

Every half-cycle of the driving laser contains two stationary phases $\bar{\boldsymbol{p}}_s$ corresponding to the long and short electron trajectories, both of which should be considered for the total harmonic dipole emission from a single atom. [8] For an electron ionized at time t' and returning at time $t = t' + \tau_f$, the stationary value of the canonical momentum along the polarization direction is:

$$\bar{\boldsymbol{p}}_s(t, \tau_f) = \frac{q_e E_L}{\omega_L^2 \tau_f} \left[\cos(\omega_L t) - \cos(\omega_L (t - \tau_f))\right] \tag{1.49}$$

The quasi-classical action can then be evaluated at the stationary points:

$$\begin{aligned}S(\bar{\boldsymbol{p}}_s, t, t') &= \frac{1}{\hbar}\int_{t-\tau_f}^{t} dt'' \left[\frac{(\bar{\boldsymbol{p}}_s - q_e \boldsymbol{A}(t''))^2}{2m_e} + I_p\right] \\ &= \frac{(I_p + U_p)\tau_f}{\hbar} - \frac{2U_p}{\hbar\omega_L^2 \tau_f}\left[1 - \cos(\omega_L \tau_f)\right] - \frac{U_p G(\tau_f)}{\hbar\omega_L}\cos\left(\omega_L(2t - \tau_f)\right),\end{aligned} \tag{1.50}$$

where

$$G(\tau_f) = \sin(\omega_L \tau_f) - \frac{4}{\omega_L \tau_f}\sin(\omega_L \tau_f/2)^2. \tag{1.51}$$

Equation (1.50) is plotted in Fig. 1.16 for the limiting cases when $I_p >> U_p$ ($\gamma_{Keldysh} >> 1$) and when $U_p >> I_p$ ($\gamma_{Keldysh} << 1$). For HHG, the tunneling regime is relevant ($\gamma_{Keldysh} < 1$, $U_p \sim I_p$), so the curve for the quasi-classical action during HHG would lie between the two limiting cases. It is noted that the curve for the case $U_p >> I_p$ exactly matches the fully classical approach where an integral is performed over the electron's kinetic energy: $S_{U_p >> I_p}(t, t') = \int_{t'}^{t} dt'' m_e v(t'')^2/\hbar$, with $v(t)$ given by Eq. (1.18).

[7] Noting the presence of the implicit factor containing units $\left[p^{-3}\right]$.

[8] However, it is noted that macroscopic phase-matching effects can preferentially select either the long or short trajectory to be generated brightly.

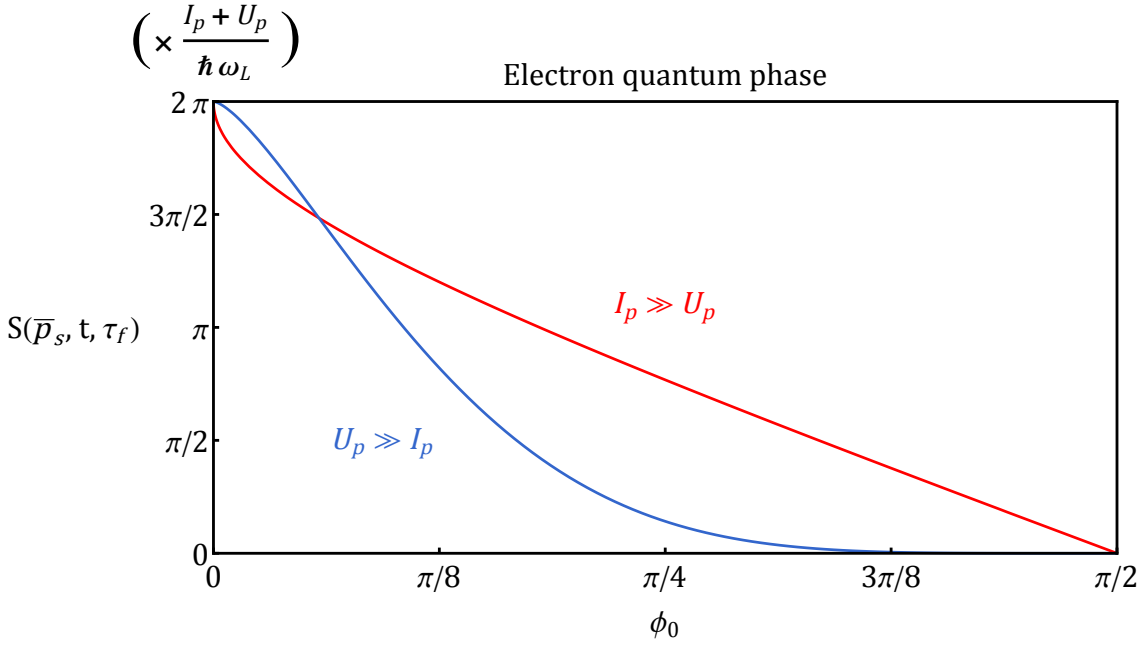

Figure 1.16: $S(\bar{\boldsymbol{p}}_s, t, \tau_f)$ plotted as a function of ionization phase ϕ_0 for the limiting cases $I_p >> U_p$ (red) and $U_p >> I_p$ (blue). For HHG in the tunneling regime, U_p will be comparable to I_p, so the resulting curve will lie between the two curves shown.

The quasi-classical action depends linearly on the duration of the trajectory τ_f, causing the long trajectories to develop significantly more phase compared to the short ones. $S(\bar{\boldsymbol{p}}_s, t, t')$ also depends linearly on the ponderomotive potential U_p, resulting in a linear dependence with respect to I_L and ultimately a cubic dependence with respect to λ_L. The linear dependence of $S(\bar{\boldsymbol{p}}_s, t, t')$ on I_L can result in a spatially-dependent harmonic phase for driving fields with nonzero ∇I_L. Additionally, the long trajectories have a stronger dependence on I_L than the short trajectories. For the trajectories that emit photons with energy $2U_p$ ($\phi_0 \cong \pi/32$ and $\phi_0 \cong 3\pi/16$), $\frac{dS(\bar{\boldsymbol{p}}_s,t,t')}{dI_L}$ is 5.3 times larger for the long trajectory than the short. The importance of this trajectory-dependent phase will be discussed in Section 1.4.3.

Another characteristic to note about the oscillating dipole $q_e\ddot{\chi}(t)$ is that it contains terms related to the interaction between the bound state $|0\rangle$ and the continuum states $|\boldsymbol{p}\rangle$, specifically, the dipole matrix elements $d_y(\boldsymbol{p})$ combined with the relative phase difference $S(\boldsymbol{p}, t, t')$. The physical interpretation is that the time-varying interference resulting from the overlap of these states gives rise to the oscillating dipole, and thus, harmonic emission. Figure 1.17 shows a quantum simulation of the electron's wavepacket, indicating the interference between the ground and continuum states.

Finally, the integral in Eq. (1.48) is usually limited to values of $t \leq T$ so that only electrons ionized during the same cycle of the harmonic emission are considered. It is possible for electrons ionized during previous cycles to recollide with the ion during the current cycle, but these free electrons' wavepackets have spread out and reduced in amplitude as a result of quantum diffusion (discussed in Section 1.3.2). Therefore, it is usually valid to neglect the contributions from previous cycles' ionized electrons.

1.3.2 Quantum Diffusion of the Electron Wavepacket

Quantum diffusion of the free electron wavepacket ultimately reduces the harmonic dipole strength. The longer the electron spends in the continuum, the more dispersed its wavepacket becomes, and the smaller amplitude it will have in the region that overlaps with the bound state wavefunction. This results in reduced harmonic emission for large values of τ_f, as can be seen in

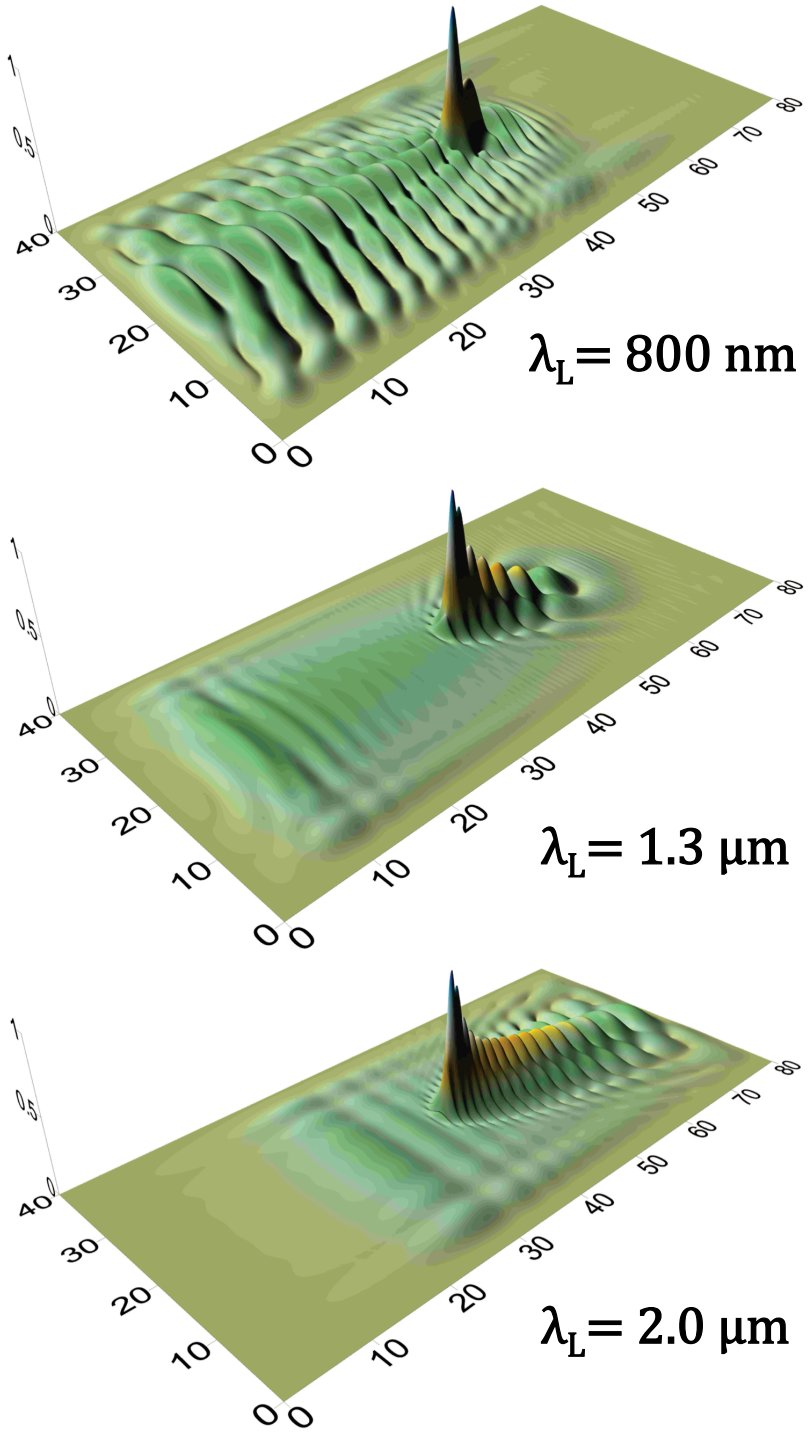

Figure 1.17: Total electron wavepacket (2D projection, normalized to 1) calculated at the peak of a three cycle laser pulse for three different wavelengths. The laser polarization is along the longer dimension of the plots. Adapted from [106].

the $\tau_f^{-3/2}$ dependence of Eq. (1.48). In terms of the harmonic intensity or flux, the scaling from quantum diffusion is τ_f^{-3}. These dependencies on τ_f are a direct result of quantum diffusion and can be derived using a Gaussian approximation for the bound state $|0\rangle$:

$$|0\rangle \cong \pi^{-3/4}\sigma_0^{-3/2}\, exp\left(\frac{-r^2}{2\sigma_0^2}\right), \tag{1.52}$$

where σ_0 specifies the spatial width of the bound wavefunction, which should be on the order of the Bohr radius r_B.

Upon ionization in the strong field approximation, some fraction of the bound wavefunction enters the continuum states $|\boldsymbol{p}\rangle$, where the relative amplitudes of the individual unbound states $C(\boldsymbol{p})$ can be calculated through a simple decomposition of $|0\rangle$ into $|\boldsymbol{p}\rangle$:

$$\begin{aligned} |0\rangle &= \int d^3\boldsymbol{p}\ C(\boldsymbol{p})\,|\boldsymbol{p}\rangle \\ C(\boldsymbol{p}) &= \int d^3\boldsymbol{r}\ \ \langle \boldsymbol{p}|0\rangle \end{aligned} \tag{1.53}$$

Here, the amplitudes $C(\boldsymbol{p})$ must have units of $\left[p^{-3}\right]$. From Eq. (1.30), it is clear that the amplitudes $C(\boldsymbol{p})$ are calculated through a simple Fourier transform of the bound state, resulting in a Gaussian in $\boldsymbol{p}$-space:

$$\begin{aligned} C(\boldsymbol{p}) &= \int d^3\boldsymbol{r}\ \pi^{-3/4}\sigma_0^{-3/2}\, exp\left(\frac{-r^2}{2\sigma_0^2}\right) \times e^{-i\boldsymbol{p}\cdot\boldsymbol{r}/\hbar} \\ &= 2\sqrt{2}\pi^{3/4}\sigma_0^{3/2} exp\left(\frac{-p^2}{4\hbar^2/\sigma_0^2}\right) \end{aligned} \tag{1.54}$$

After the ionization step, the freed electron is subjected to the time-dependent oscillating laser potential. The expectation value of the ionized electron's position

$$\langle \boldsymbol{r}\rangle = \int d^3\boldsymbol{r} \int d^3\boldsymbol{p}\ C^*(\boldsymbol{p})\,\langle \boldsymbol{p}|\,\boldsymbol{r}\,C(\boldsymbol{p})\,|\boldsymbol{p}\rangle \tag{1.55}$$

should follow the motion described during the propagation step in Section 1.2.2. The electron's wavepacket will diffuse in addition to this motion, and it is assumed that the diffusion transverse to the polarization direction can be calculated separately from the average motion. This is allowed since the Schrödinger equation is separable in the non-relativistic regime, giving rise to a free particle Hamiltonian for the transverse directions. Conveniently, each $|\boldsymbol{p}\rangle$ has a propagator for

time development in the form of the phase $e^{-iE_p t/\hbar}$, where $E_p = \frac{p^2}{2m_e}$. Therefore, to propagate the wavefunction forward in time, a quadratic phase must be added:

$$|\Psi(\boldsymbol{r},t)\rangle = \int d^3\boldsymbol{p}\; C(\boldsymbol{p})\,|\boldsymbol{p}\rangle\, exp\left(\frac{-ip^2 t}{2m_e\hbar}\right) \tag{1.56}$$

Using Eq. (1.30) and Eq. (1.54), $|\Psi(\boldsymbol{r},t)\rangle$ takes the form of an inverse Fourier transform of a Gaussian multiplied by a quadratic phase. The quadratic phase in momentum space is responsible for broadening the wavepacket in position space, and the integral can be handled by treating the total integrand as a single Gaussian with a complex width in momentum space. Performing the integration along one of the transverse dimensions yields the wavefunction along that dimension at time t after ionization:

$$|\Psi_x(t)\rangle = \pi^{-1/4}\sigma(t)^{-1/2}\, exp\left(\frac{-x^2}{2\sigma(t)^2}\right) exp\left(i\frac{m_e x^2}{2\hbar R(t)}\right) exp(i\Gamma(t)), \tag{1.57}$$

where:

$$\begin{aligned} t_D &= \sigma_0^2 m_e/\hbar \\ \sigma(t) &= \sigma_0\,\sqrt{1+\left(\frac{t}{t_D}\right)^2} \\ R(t) &= t\left[1+\left(\frac{t_D}{t}\right)^2\right] \\ \Gamma(t) &= -\frac{1}{2}\tan^{-1}\left(\frac{t}{t_D}\right) \end{aligned} \tag{1.58}$$

This form [9] derived from the free particle Schrödinger equation is valid for the two dimensions transverse to the polarization axis in the non-relativistic regime, but the presence of the time-dependent laser potential prevents the polarization axis to be treated as a free particle. Additionally, the ground state before ionization would not be expected to have the same width along the polarization axis as the transverse width σ_0. Indeed, for the transverse directions, σ_0 is typically larger than r_B due to the shifting of the electron in $V_{atomic}(\boldsymbol{r})$ by the laser field. $\sigma_0 \cong \left(\frac{3\sqrt{2}\hbar}{8m_e\omega_L}\gamma_{Keldysh}\right)^{1/2}$ was presented in [28], while $\sigma_0 \cong 4\,r_B$ has been shown to agree with numerical studies [169, 170, 92].

[9] Note the similarity to Gaussian beam propagation (Section 1.4.3), which uses the same wave-decomposition of a Gaussian electric field amplitude. For instance, the characteristic diffusion time t_D is analogous to the Rayleigh range z_R. The parabolic and Gouy phase terms are present as well.

Using this value, the characteristic diffusion time $t_D = 388\ as$, which for reference is comparable to the return time τ_f of an electron ionized at $\phi_0 = \pi/10$ for a driving laser with wavelength 175 nm.

Despite the fact that the polarization direction cannot be treated equally, diffusion should still occur in that direction, even if not exactly as $\sigma(t)$. From Eq. (1.57) and the form for $\sigma(t)$, it can be assumed that the total probability density $\langle\Psi(t)|\Psi(t)\rangle$ scales roughly as t^{-3} in amplitude, for $t >$ several t_D. Therefore, the free electron's overlap with the bound state will correspondingly be reduced by this factor. This is in agreement with the statement at the beginning of this section: the harmonic flux scaling from quantum diffusion is τ_f^{-3}, or λ^{-3}.

1.3.3 Quantum Mechanical Characteristics of HHG

The quantum mechanical analysis preformed in this section has revealed new physics beyond the simple semi-classical approach from Section 1.2. This approach gives a more straightforward and intuitive method for calculating the harmonic emission as opposed to classical scattering theory. Of primary importance is the treatment of the ionized electron as a spreading wavepacket, which accounts for the electron's many possible initial momentum states and ultimately results in an analytical scaling of τ_f^{-3} for the harmonic flux. The single-atom HHG flux scaling thus receives a λ_L^{-3} contribution from quantum diffusion, and a λ_L^{-2} scaling from increasing harmonic bandwidth (Eq. (1.22)) for a fixed energy interval. Macroscopic effects can further limit this scaling, resulting in a final HHG flux scaling ranging from λ_L^{-5} to λ_L^{-9} [161, 120, 42, 98].

Finally, the quantum mechanical explanation for the harmonic emission lies in the oscillating dipole $q_e\ddot{\chi}(t)$, where the harmonic frequency dependence arises from the phase $S(\bar{\boldsymbol{p}}, t, t')$. In short, the semi-classical action is responsible for the frequency conversion, while also describing the trajectory the electron takes. Thus, any perturbation of the electron's trajectory can give rise to a phase shift in the harmonic dipole. Absolute phase shifts are of little importance in terms of their effect on the harmonic spectrum except when the phase shifts are asymmetric across half-cycles of the laser. This phase asymmetry can emulate a linear phase in the time domain, mapping to a fre-

quency shift in the spectral domain. Therefore, it is possible to observe harmonics that are shifted from their typical odd positions, provided there is a mechanism to break the half-cycle symmetry of the electron trajectory. Relativistic effects (Chapter 4), quickly varying pulse envelopes ($dt \approx T$), and multicolor drivers are possible symmetry-breaking mechanisms.

1.4 Macroscopic Picture of HHG

To this point, only the single-atom picture of HHG has been discussed in detail. The physics that governs the microscopic picture sets limits on the properties of HHG that are possible, and macroscopic effects tend to further constrain those characteristics. Some of the additional constraints can be considered detrimental for certain applications. As will be shown, macroscopic effects tend to reduce the spectral cutoff energy, which can limit spectroscopy experiments [135]. On the other hand, the presence of many atoms contributing to the final output leads to bright emission that is highly directional (as opposed to the Larmor radiation pattern of Fig. 1.15), allowing the use of smaller optics to steer the full harmonic beam. The harmonic pulse train in the time domain can also be restricted to one or a few half-cycles, which can be beneficial for time-resolved applications. Here, the details of phase-matching dynamics in the time-domain are left for further discussion in Chapter 2.

The macroscopic treatment of HHG will assume a gaseous medium of length L_{med} and density $\rho(z)$, where $\rho(z)$ may vary as a function of location z along the medium. For simplicity, $\rho(z)$ will be equal to zero for $z < 0$ and for $z > L_{med}$, and the final harmonic output will be defined at the location $z = L_{med}$.

1.4.1 Phase-Matching

First, consider the 1D case where the gas medium has a constant density $\rho(z) = \rho_0$, and the driving field is a monochromatic plane-wave with frequency ω_L and wavenumber $k_L = n(\omega_L)\,\omega_L/c$. The emission from an atom at location z will result in the following field strength at the medium

exit:

$$E_{HHG}(L_{med}) = E^0_{HHG} e^{i\Phi(z)} e^{i\gamma(\omega_q)(L_{med}-z)}, \tag{1.59}$$

where $E^0_{HHG} e^{i\Phi(z)}$ is the microscopic amplitude and phase of the harmonic field at the time and location of emission, and $\gamma(\omega_q) = k(\omega_q) + i\kappa(\omega_q)$ is the complex wavenumber at the harmonic frequency $\omega_q = q\omega_L$. The harmonic emission phase $\Phi(z)$ is related to the phase of the fundamental field at the time and location of emission. Considering the emission from two atoms at locations z_1 and z_2, the combined output will be given by:

$$\sum_{z_i}^{2} E_{HHG}(L_{med}) = E^0_{HHG} e^{i\Phi(z_1)} e^{i\gamma(\omega_q)(L_{med}-z_1)} \left(1 + e^{i(z_2-z_1)(q*n(\omega_L)\omega_L/c - \gamma(\omega_q))}\right) \tag{1.60}$$

To achieve the maximum output amplitude for arbitrary z_1 and z_2, the following must be true: $k(\omega_q) = q * n(\omega_L)\omega_L/c$. Since $k(\omega_q)$ is defined as $n(\omega_q)\omega_q/c$, the condition for maximum harmonic field strength at the medium exit simplifies to an equivalence of refractive indices for the fundamental and harmonic frequencies: $n(\omega_L) = n(\omega_q)$. Often, this is described as a matching of the phase velocities for the two frequencies $v_\phi(\omega_L) = v_\phi(\omega_q)$, or as a wavevector mismatch equation:

$$\Delta k \equiv k(q\,\omega_L) - q\,k(\omega_L) = 0 \tag{1.61}$$

Equation (1.61) represents the 1D phase-matching condition for the simple monochromatic, collinear scenario. For an arbitrary number of driving fields with frequencies ω_j and 3D wavevectors $\boldsymbol{k}_j$, the general phase-matching equation is:

$$\begin{aligned} \Delta\boldsymbol{k} &\equiv \boldsymbol{k}_Q(\omega_Q) - \sum_j m_j\,\boldsymbol{k}_j(\omega_j) = 0 \\ \omega_Q &= \sum_j m_j\,\omega_j \end{aligned} \tag{1.62}$$

Here, m_j is an integer describing the number of photons from driving field j that contribute to the final output field with frequency ω_Q propagating along the direction of $\boldsymbol{k}_Q(\omega_Q)$. Sum frequency generation (SFG) corresponds to values of m_j that are all positive, whereas difference frequency generation (DFG) can occur when one or more of the m_j values are negative. More discussion on high-order DFG is presented in Section 5.3.

Once again, Eq. (1.62) is the condition for the brightest harmonic field strength at the exit of the HHG medium. Its physical interpretation is the conservation of momentum and energy for the frequency conversion process. For $|\Delta \boldsymbol{k}| \neq 0$, a coherence length L_{coh} can be defined that specifies the medium length over which the harmonic emission adds constructively:

$$L_{coh} \equiv \frac{\pi}{|\Delta \boldsymbol{k}|} \tag{1.63}$$

The effect of the coherence length L_{coh} on the final harmonic output will be discussed further in Section 1.4.5. A diagram of the phase-matching concept is shown in Fig. 1.18.

1.4.2 Phase-Matching in Fractionally Ionized Gases

Calculating $\Delta \boldsymbol{k}$ requires knowledge of the medium and its effect on $\boldsymbol{k}(\omega_L)$ and $\boldsymbol{k}(\omega_q)$. Furthermore, the HHG geometry can contribute to the total phase mismatch. The wavevector can be written as a sum of each contribution:

$$\boldsymbol{k}(\omega) = \boldsymbol{k}_{vacuum}(\omega) + \boldsymbol{k}_{atoms}(\omega) + \boldsymbol{k}_{ions}(\omega) + \boldsymbol{k}_{plasma}(\omega) + \boldsymbol{k}_{geom}(\omega) + \boldsymbol{k}_{\nabla I_L}(\omega) \tag{1.64}$$

The first four terms are simple to calculate for any experimental geometry. The vacuum wavevector has magnitude $k_{vacuum}(\omega) = 2\pi\omega/c$. For collinear HHG where all driving beams are parallel to the output beam ($\boldsymbol{k}_j(\omega_j) \parallel \boldsymbol{k}(\omega_Q) \ \forall \ j$), the vacuum contribution to Δk vanishes. However, this is not true for noncollinear geometries.

The neutral atom term can be determined from the dispersion of the neutral portion of the medium. The wavevector magnitude $k_{atoms}(\omega)$ is related to the refractive index:

$$k_{atoms}(\omega) = [n(\omega) - 1]\,\frac{\omega}{c} \tag{1.65}$$

If the linear index of refraction of a neutral gaseous medium at 1 atm is $n_1^0(\omega)$, then the neutral contribution to the linear index of refraction of a gas at arbitrary pressure ($P = \bar{P} \times 1\ atm$) and neutral population fraction η_0 would be $n_1(P, \eta, \omega) = 1 + \bar{P}\eta_0(n_1^0(\omega) - 1)$. [10] Furthermore, there is

[10] For clarity, $\eta_0 = 1$ represents a fully neutral gas without ionization; ion species' population fractions are represented as η_i. The total ionization fraction $\eta_{tot} = \sum_{i=1}^{Z} i * \eta_i$

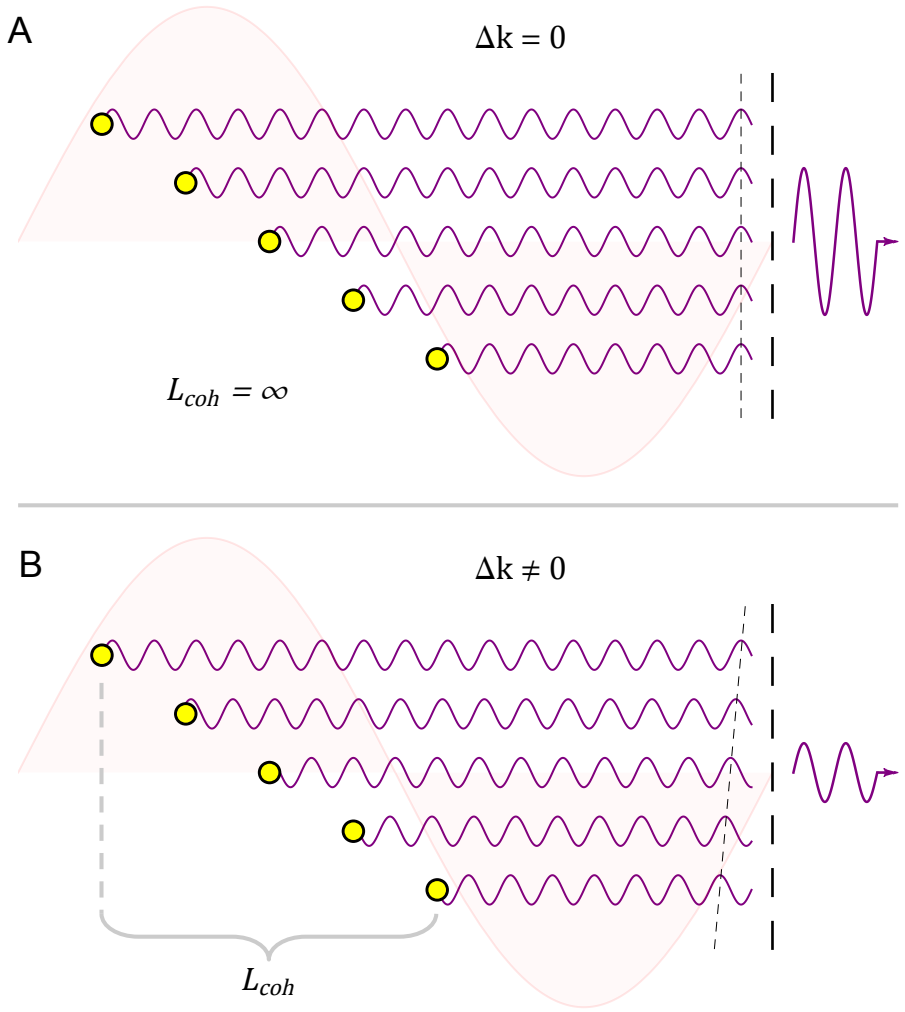

Figure 1.18: Phase-matching during HHG. (A) The wavevector mismatch $\Delta k = 0$, corresponding to an infinite coherence length L_{coh}. All atoms emit harmonics in sync with each other, leading to a bright output. (B) The wavevector mismatch $\Delta k \neq 0$, corresponding to a finite coherence length L_{coh}. The atoms shown span one coherence length, resulting in weaker (but nonzero) emission. Note that $L_{coh} \sim \lambda_L$ is an extreme case of phase mismatch.

a nonlinear index of refraction n_2^0 from neutral atoms that can contribute to the total index if the laser intensity is high. In HHG, only the driving fields have sufficient intensity for the nonlinear refractive index to be significant. Ultimately, the equation for Δk_{atoms} in the monochromatic, collinear case becomes:

$$\Delta k_{atoms} = k_{atoms}(q\omega_L) - qk_{atoms}(\omega_L) = -q\bar{P}\eta_0 \frac{2\pi}{\lambda_L}(\Delta\delta^0 + n_2^0 I_L), \tag{1.66}$$

where $\Delta\delta^0 = n_1^0(\omega_L) - n_1^0(q\omega_L)$ is the difference in the linear refractive index at the fundamental and harmonic frequencies, and $n_2^0 I_L$ is the nonlinear contribution to the refractive index from the driving laser at λ_L and 1 atm. For fundamental and harmonic frequencies far from resonances, $\Delta\delta^0$ is positive, as can be deduced from Fig. 1.19. Thus, $\Delta k_{atoms} < 0$.

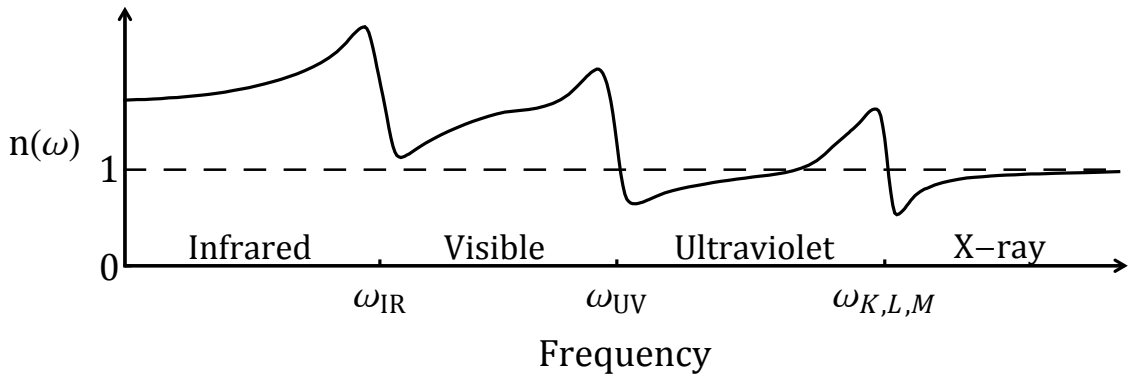

Figure 1.19: A qualitative illustration of the real part of the refractive index across the electromagnetic spectrum. Resonances occur at atomic and molecular absorption edges, resulting in variations in $n(\omega)$ via the Kramers-Kronig relations. For X-ray frequencies above all atomic resonances, there is asymptotic tendancy toward $n(\omega) = 1$. Figure adapted from [7].

The contribution to $\boldsymbol{k}(\omega)$ from ion species can be approached the same way as the atom term. Unsurprisingly, the form for Δk is nearly identical:

$$\Delta k_{ions} = -\sum_{i=1}^{Z} q\bar{P}\eta_i \frac{2\pi}{\lambda_L}(\Delta\delta^i + n_2^i I_L), \tag{1.67}$$

where the index i refers to quantities that pertain to ion species of charge state i. The parameters n_2^i and $\Delta\delta^i$ can be difficult to determine precisely since experimental measurements would need to occur on ultrafast time scales and would be convoluted by the presence of plasma and multiple ion

species. *Ab initio* calculations can be performed to estimate the order of magnitude of the linear and nonlinear refractive indices, as demonstrated in [134] for Ar species at 270 nm. Similarly to neutral atoms, $\Delta k_{ions} < 0$.

The plasma term of Eq. (1.64) can also be determined through the refractive index. The plasma resonance frequency ω_p is given by:

$$\omega_p = \sqrt{\frac{q_e^2 n_e}{\epsilon_0 m_e}}, \tag{1.68}$$

where $n_e = \eta_{tot} N_a \bar{P}$ is the free electron number density, and N_a is the number density of atoms in a gas at standard pressure and temperature. The plasma resonance leads to a plasma refractive index given by:

$$n_{plasma}(\omega) = \sqrt{1 - \left(\frac{\omega_p}{\omega}\right)^2} = \sqrt{1 - \left(\frac{n_e}{n_c(\omega)}\right)}, \tag{1.69}$$

where $n_c(\omega) = \epsilon_0 m_e \omega^2 / q_e^2$ is the critical plasma density above which light at frequency ω will be reflected by the plasma. The typical pressures and ionization levels used for HHG are such that the plasma density n_e is much smaller than the critical density n_c. [11] As such, a Taylor expansion can be performed to approximate the plasma refractive index:

$$n_{plasma}(\omega) \cong 1 - \frac{1}{2}\left(\frac{\omega_p}{\omega}\right)^2 \tag{1.70}$$

The plasma term of Eq. (1.64) has a magnitude:

$$k_{plasma}(\omega) = (n_{plasma}(\omega) - 1)\frac{\omega}{c} = -\frac{\omega_p^2}{2c\omega} \tag{1.71}$$

For the monochromatic, collinear HHG case, the plasma term for the phase mismatch is then:

$$\Delta k_{plasma} = \frac{\omega_p^2}{2c\omega_L}\frac{(q^2-1)}{q} = n_e r_e \frac{(q^2-1)}{q}\lambda_L = \eta_{tot} N_a r_e \bar{P}\frac{(q^2-1)}{q}\lambda_L \tag{1.72}$$

Here, the classical electron radius r_e was substituted. For large harmonic orders $q \gtrsim 10$, the term $\frac{(q^2-1)}{q} \cong q$, allowing Δk_{plasma} to have the same $q\bar{P}$ dependence as Δk_{atoms} and Δk_{ions}. For nonzero ionization levels, $\Delta k_{plasma} > 0$.

[11] However, high pressures can be necessary for phase-matching HHG when using longer wavelength drivers. Therefore, plasma mirroring effects could introduce a limitation on HHG driven by wavelengths $\lambda_L > 10$ µm.

Before considering the two remaining terms relevant to phase-matching, some conclusions can be drawn concerning the contribution from the fractionally-ionized medium. Under the most common HHG conditions where a low level of tunnel ionization occurs ($\eta_1 << 1$, $\eta_0 = 1 - \eta_1$), Δk_{ions} can be neglected. The medium's contribution to the total phase-mismatch at high harmonic order is then:

$$\Delta k_{medium} \cong \Delta k_{atoms} + \Delta k_{plasma} \cong q\bar{P}\left[-(1-\eta_1)\frac{2\pi}{\lambda_L}(\Delta\delta^0 + n_2^0\, I_L) + \eta_1 N_a r_e \lambda_L\right] \tag{1.73}$$

Satisfying the phase-matching condition $\Delta k_{medium} = 0$ for arbitrary driving wavelength and harmonic order gives a solution for the critical ionization level:

$$\eta_c = \left[\frac{\lambda_L^2 N_a r_e}{2\pi(\Delta\delta^0 + n_2^0 I_L)} + 1\right]^{-1} \tag{1.74}$$

Often, the nonlinear term $n_2^0 I_L$ is small compared to $\Delta\delta^0$, but η_c still depends on λ_L (and somewhat on q through $\Delta\delta^0$). The critical ionization level η_c represents a zero crossing of $\Delta k_{medium}(\eta_1)$. For $\eta_1 < \eta_c \longrightarrow \Delta k_{medium} < 0$, and for $\eta_1 > \eta_c \longrightarrow \Delta k_{medium} > 0$. In the next section, the geometrical contributions to Δk will be shown to be positive. As a result, phase-matching is only possible for $\eta_1 < \eta_c$ (in the monochromatic, collinear HHG scenario).

Just considering the medium contribution to phase-matching, some conclusions can be drawn regarding the driving laser intensities that are appropriate for phase-matched HHG. Assuming an 8-cycle driving laser pulse, ADK ionization levels can be calculated so that the critical ionization level η_c is achieved at the peak of the pulse. This sets an optimal peak intensity level that will maximize the efficiency of the HHG process, since exceeding this peak intensity level will cause phase-matching to occur on the leading edge of the pulse where there are lower intensities, while smaller peak intensities will result in phase-matching on the trailing edge of the pulse (or not at all). Performing the ADK calculation results in Fig. 1.20, which shows the optimal intensities to drive HHG in noble gases for driving wavelengths up to 20 μm. Also plotted are the optimal intensities for a mode-averaged HHG signal.

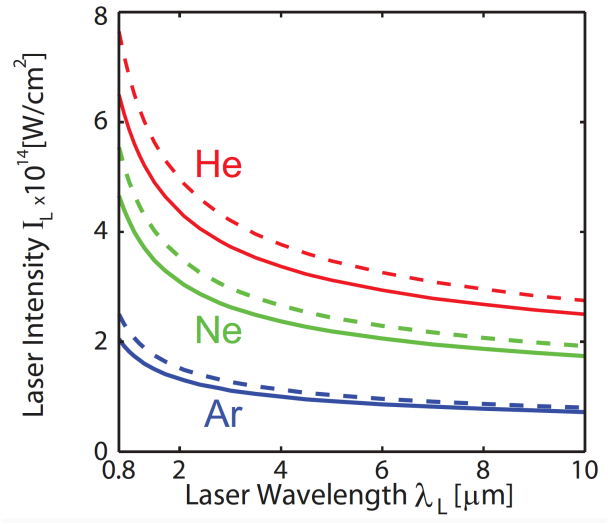

Figure 1.20: Predicted laser intensity required to reach the critical ionization level at the peak of an 8-cycle laser pulse on axis (solid line), and when modal averaging is taken into account (dashed line). Adapted from [106].

1.4.3 Phase-Matching Geometries

In this section, the geometrical contribution to $\Delta\boldsymbol{k}$ will be discussed. For monochromatic, collinear HHG, there are two primary geometries: the Gaussian free-focus geometry and the waveguide geometry. Certainly, there are other geometries possible for multi-color, noncollinear schemes, in which the full vector form of $\Delta\boldsymbol{k}$ must be considered. The two-beam, noncollinear, bichromatic scenario will be discussed in Section 5.3. Here, only the Gaussian free-focus and waveguide geometries will be considered.

Gaussian Free-Focus Geometry

Realistic laser spatial modes can be flat-topped, Bessel- or sinc-like as a result of amplifier gain profiles, propagation in fiber waveguides, and clipping on apertures. However, these can be approximated as Gaussian for simplicity, since it is straightforward to arrive at a theoretical description of how Gaussian modes propagate. Gaussian modes are convenient to model because they maintain their Gaussian shape throughout propagation. The derivation for a Gaussian mode amplitude and phase in the paraxial approximation involves solving the source-free scalar wave equation, and is analogous to the derivation of the free electron wavepacket $|\Psi(t)\rangle$ presented in Section 1.3.2. A Gaussian mode takes the following scalar form in the transverse direction (r), as a function of propagation distance z from a focal point:

$$E(r,z) = E_0 \frac{w_0}{w(z)} exp\left(\frac{-r^2}{w(z)^2}\right) exp\left(\frac{ikr^2}{2R(z)}\right) exp(i\Gamma(z)), \tag{1.75}$$

where:

$$\begin{aligned} z_R &= \frac{\pi w_0^2}{\lambda_L} \\ w(z) &= w_0\sqrt{1+\left(\frac{z}{z_R}\right)^2} \\ R(z) &= z\left[1+\left(\frac{z_R}{z}\right)^2\right] \\ \Gamma(z) &= -tan^{-1}\left(\frac{z}{z_R}\right) \end{aligned} \tag{1.76}$$

Here, $w(z)$ is the radius at which the intensity drops to $1/e^2$ of the central intensity (with value w_0 at the focal position), z_R is called the Rayleigh range, $R(z)$ represents the wavefront radius of

curvature, and $\Gamma(z)$ is called the Gouy phase. Note that here, $k = \frac{2\pi}{\lambda}$ is the vacuum wavenumber. Figure 1.21 depicts the qualities of a Gaussian free-focus.

To evaluate the wavevector $\boldsymbol{k}_{Gaussian}$ of the mode, the gradient of its phase is taken:

$$\begin{gathered} \boldsymbol{k}_{Gaussian} = \boldsymbol{\nabla}\Phi(\boldsymbol{r}) \\ \rightarrow k_{Gaussian} = \frac{\partial}{\partial z}\left[\frac{kr^2}{2R(z)} + \Gamma(z)\right] = -\frac{\omega}{c}\left[\frac{w_0^2 + r^2}{2z_R^2\left(1 + \frac{z^2}{z_R^2}\right)}\right] \end{gathered} \tag{1.77}$$

The wavefront curvature and Gouy phase ultimately reduce the Gaussian mode wavenumber compared to the plane-wave value in vacuum. Looking on-axis ($r = 0$):

$$\begin{aligned} k_{Gaussian}(r=0) \rightarrow k_{Gouy} &= \frac{-1}{z_R\left(1 + \frac{z^2}{z_R^2}\right)} \\ &\cong \frac{-1}{z_R} \quad (\text{for} \quad z << z_R) \end{aligned} \tag{1.78}$$

If HHG was possible far from the focus ($z >> z_R$), the mode wavenumber would become $k_{Gouy} \cong 0$. For the purposes of standard HHG in a free-focus, only regions near the focus where there is high intensity will be relevant. With the assumption that the harmonics are generated with a similar confocal parameter, the geometric contribution to Δk from the Gouy phase is:

$$\Delta k_{Gouy} = \frac{(q-1)}{z_R} \tag{1.79}$$

Clearly, $\Delta k_{Gouy} > 0$.

Off-axis, the effect of the radius of curvature is nonzero and varies quadratically with r:

$$\Delta k_{RoC} = \frac{(q-1)}{z_R}\frac{r^2}{w_0^2} \tag{1.80}$$

Its contribution can result in a radially-dependent phase-mismatch where certain radii can be roughly phase-matched for a length $\sim z_R$ while other radii contain a large amount of phase-mismatch. Again, the wavevector mismatch is postive: $\Delta k_{RoC} > 0$. The total geometric wavevector mismatch for a Gaussian mode at arbitrary radius is the sum $\Delta k_{Gouy} + \Delta k_{RoC}$:

$$\Delta k_{Gaussian} = \frac{(q-1)}{z_R}\left(1 + \frac{r^2}{w_0^2}\right) \tag{1.81}$$

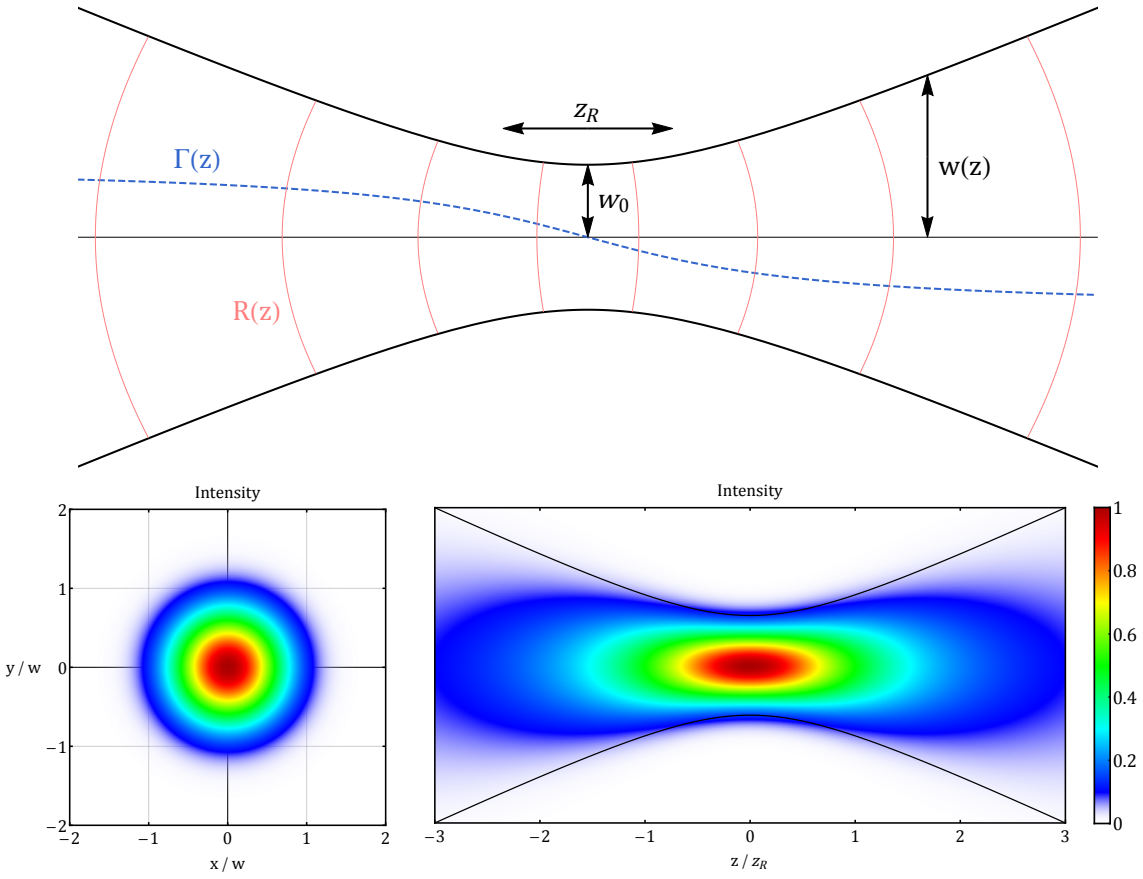

Figure 1.21: An illustration of a Gaussian free-focus and its characteristic parameters.

Recall that there is one final term that contributes to the wavevector: $\boldsymbol{k}_{\nabla I_L}(\omega)$. This term is related to the linear dependence of the intensity on the electron's quantum phase, as discussed in Section 1.3.1. Thus, any driving field that has a nonzero intensity gradient along the z-axis will result in an additional phase-mismatch. The phase only applies to the harmonic wavevector, so that the form for the wavevector mismatch is:

$$\Delta\boldsymbol{k}_{\nabla I_L} = \frac{q_e^2\tau_f}{4\hbar m_e\omega_L^2}\boldsymbol{\nabla}|E(r,z)|^2 \tag{1.82}$$

The gradient (along z) of $|E(r,z)|^2$ from Eq. (1.75) is:

$$\frac{\partial}{\partial z}|E(r,z)|^2 = -2|E(r,z)|^2\frac{(w(z)^2-2r^2)\lambda_L}{\pi w(z)^4}\left(\frac{z}{z_R}\right) \tag{1.83}$$

It is evident that $\Delta k_{\nabla I_L}$ for a Gaussian free-focus varies with respect to z and can have a negative magnitude. This fact can be exploited when also considering the geometric contribution $\Delta k_{Gaussian}$. Looking on-axis, it is possible for the sum $\Delta k_{Gouy} + \Delta k_{\nabla I_L} = 0$ at certain locations along the z-axis. Additionally, $\Delta k_{\nabla I_L}$ depends on τ_f, suggesting that different trajectories can be phase-matched at different z-positions. Figure 1.22 illustrates this trajectory-dependent, z-dependent phase-matching concept. The importance of this finding is that for a Gaussian beam focused through a short medium ($L_{med} < z_R$, i.e. a gas jet or gas cell), the trajectories that will be phase-matched will depend on the z-location of the gas jet with respect to the focal position. Long trajectories can be phase-matched when the gas jet is close to the focus, whereas short trajectories would be phase-matched for a gas jet placed just after the focus. This analysis assumes the phase-matching occurs along the axis, but phase-matching can occur off-axis. L'Huillier and Balcou *et al.* [69, 8] discovered that the harmonic efficiency and beam divergence can be controlled by adjusting the focal spot with respect to the gas jet. Long trajectories tend to phase-match in an off-axis ring, whereas short trajectories phase-match on-axis.

For a Gaussian free-focus, the total phase mismatch equation on-axis is the sum of all the

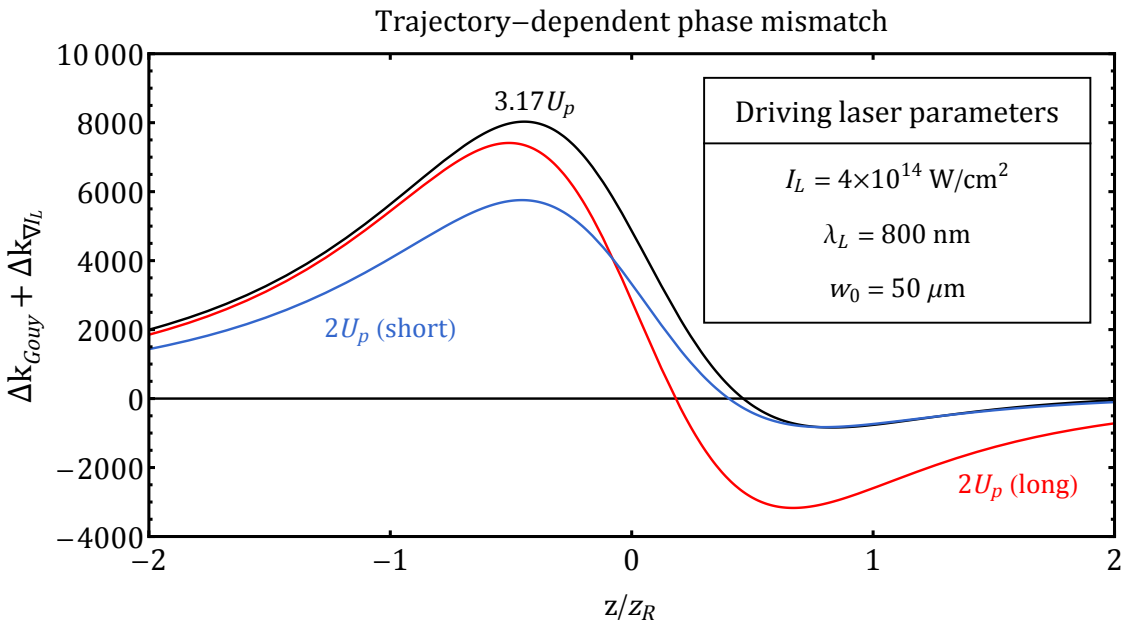

Figure 1.22: A plot of the on-axis geometrical phase-mismatch $\Delta k_{Gouy} + \Delta k_{\nabla I_L}$ for a Gaussian free-focus as a function of axial position. Typical HHG driving conditions are used: $I_L = 4 \times 10^{14}$ W/cm^2, $\lambda_L = 800$ nm, and $w_0 = 50$ µm. Under these conditions, $z_R = 9.8$ mm, and $2U_p$ corresponds to $q \cong 31$ while $3.17U_p$ corresponds to $q \cong 49$. Ionization phases for the $2U_p$ cases are $\phi_0 = \pi/32$ (long) and $\phi_0 = 3\pi/16$ (short).

contributions discussed here and in Section 1.4.2:

$$\begin{aligned}\Delta k &= \underbrace{\Delta k_{atoms}}_{<0} + \underbrace{\Delta k_{ions}}_{<0} + \underbrace{\Delta k_{plasma}}_{>0} + \underbrace{\Delta k_{Gouy}}_{>0} + \underbrace{\Delta k_{\nabla I_L}}_{+/-} \\ &= q\bar{P}\left[-\sum_{i=0}^{Z}\left(\eta_i \frac{2\pi}{\lambda_L}(\Delta\delta^i + n_2^i I_L)\right) + \eta_{tot} N_a r_e \lambda_L\right] + \frac{(q-1)}{z_R} + \frac{q_e^2 \tau_f}{4\hbar m_e \omega_L^2}\boldsymbol{\nabla}|E(r,z)|^2\end{aligned} \tag{1.84}$$

The off-axis equation requires the full vector form of $\Delta\boldsymbol{k}$, which includes a nonzero contribution from $\Delta\boldsymbol{k}_{vacuum}$ and $\Delta\boldsymbol{k}_{RoC}$.

Waveguide Geometry

HHG in a Gaussian free-focus is limited to a region where the driving laser maintains high intensity. Additionally, the z-dependence of $\Delta k_{\nabla I_L}$ imposes a restriction on the length of medium where phase-matching is possible. These limitations ultimately reduce the harmonic flux possible in a free-focus geometry. Thus, an alternative geometry that can extend the interaction length for efficient harmonic generation is desirable. The goal would employ radial confinement of the laser energy over long distances, which is possible with waveguiding techniques. Plasma waveguides have been used [85, 16, 132], as well as gas-filled hollow capillaries [110, 106]. Here, the latter will be explored in detail. Figure 1.23 depicts the hollow waveguide geometry under consideration.

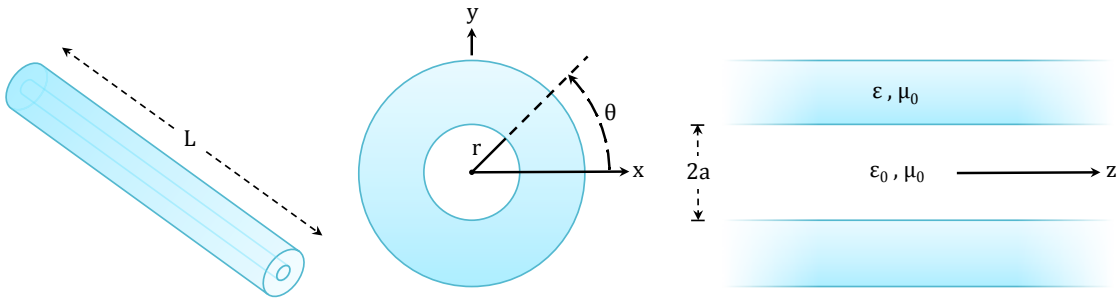

Figure 1.23: Illustrations of the hollow waveguide geometry.

Marcatili solved for the full electromagnetic field components for the hollow waveguide modes in [79]. Appendix A contains detailed information on the waveguide modes and a comparison to Gaussian beams. Here, the mode that most closely resembles a linearly-polarized Gaussian mode (the EH_{11} mode) will be investigated (though the TE and TM "doughnut" modes can be used to

drive HHG, as will be discussed in Section 5.1). For the purposes of phase-matching, the complex wavenumber γ_{pq} is of primary importance:

$$\gamma_{pq} = k\left[1 - \frac{1}{2}\left(\frac{u_{pq}}{ka}\right)^2\left(1 - \frac{i}{ka}\frac{(n^2+1)}{\sqrt{n^2-1}}\right)\right] \tag{1.85}$$

Here, J_p is a p^{th} order Bessel function of the first kind, u_{pq} is the q^{th} root of the equation $J_{p-1}(u_{pq}) = 0$, $n = \sqrt{\epsilon/\epsilon_0}$ is the complex refractive index of the waveguide material, $k = 2\pi/\lambda$, and a is the inside radius of the hollow waveguide.

For the EH_{pq} mode, $k_{waveguide}(\omega) = Re[\gamma_{pq}(\omega)]$. Neglecting the small real contribution resulting from $Im\left[n^2\right]$, the wavevector mismatch from the waveguide mode can be easily obtained:

$$\begin{aligned}\Delta k_{waveguide} = k_{waveguide}(q\omega_L) - qk_{waveguide}(\omega_L) &\cong \frac{u_{pq}^2\lambda_L(q^2-1)}{4\pi q a^2} \\ &\cong \frac{qu_{pq}^2\lambda_L}{4\pi a^2} \quad (\text{for } \; q >> 1)\end{aligned} \tag{1.86}$$

Because the waveguide confines the light, each mode will propagate independently and without any change in shape or phase (barring any nonlinear effects that may exist during strong field processes like HHG). In the linear regime, there are no Gouy phase or radius of curvature effects. For low loss modes ($Im[\gamma_{pq}] * L_{waveguide} << 1$) and low levels of ionization, there would be a negligible longitudinal gradient in the intensity, so $\Delta k_{\nabla I_L} \cong 0$ on-axis. $\Delta k_{waveguide}$ would be the only geometrical component. Generally, however, the imaginary component of γ_{pq} leads to a nonzero gradient of $|E_{pq}(r,z)|^2$ along the propagation direction:

$$\frac{\partial}{\partial z}|E_{pq}(r,z)|^2 = -2Im[\gamma_{pq}]\,|E_{pq}(r,z)|^2 \tag{1.87}$$

Since $|E_{pq}(r,z)|^2$ decays exponentially as a function of z, so does $\Delta k_{\nabla I_L}$ for this geometry. Ultimately, the total wavevector mismatch on-axis for the hollow waveguide geometry is:

$$\begin{aligned}\Delta k &= \underbrace{\Delta k_{atoms}}_{<0} + \underbrace{\Delta k_{ions}}_{<0} + \underbrace{\Delta k_{plasma}}_{>0} + \underbrace{\Delta k_{waveguide}}_{>0} + \underbrace{\Delta k_{\nabla I_L}}_{\cong 0} \\ &= q\bar{P}\left[-\sum_{i=0}^{Z}\left(\eta_i\frac{2\pi}{\lambda_L}(\Delta\delta^i + n_2^i\, I_L)\right) + \eta_{tot}N_a r_e \lambda_L\right] + \frac{qu_{pq}^2\lambda_L}{4\pi a^2} + \frac{q_e^2\tau_f}{4\hbar m_e\omega_L^2}\boldsymbol{\nabla}|E_{pq}(r,z)|^2\end{aligned} \tag{1.88}$$

Phase-matching in the waveguide geometry is possible by balancing the phase-mismatch contribution from the medium with that from the waveguide: $\Delta k_{medium} + \Delta k_{waveguide} = 0$. Recall that the medium contribution is either positive or negative depending on the ionization level. Only for $\eta_1 < \eta_c$ can $\Delta k_{medium} = \Delta k_{atoms} + \Delta k_{ions} + \Delta k_{plasma} < 0$. Furthermore, the medium contribution depends linearly on the pressure. Thus, as long as the ionization level is below the critical level, there is a route to achieving phase-matching by adjusting $\bar{P}$.

Perfect phase-matching ($\Delta k = 0$) during HHG creates restrictions on the driving conditions of the process. Because the ionization level has an upper bound η_c, the driving laser cannot produce an excess level of ionization within the medium due to its high intensity. For driving pulses with long durations, the ionization fraction builds to high levels before the peak of the pulse arrives. In this case, the peak intensity must be reduced such that phase-matching may occur at the pulse's peak (thus limiting the single atom cutoff that scales as $I_L \lambda_L^2$). Alternatively, the pulse duration may be reduced to limit the accumulation of plasma before the center of the pulse, thus allowing higher peak intensities to be achieved at the phase-matched ionization level. The pulse duration can only be reduced so far (a single cycle), imposing a maximum intensity achievable for perfect phase-matched conditions. Single-cycle drivers can also have group velocity walkoff issues that limit the medium length over which HHG is generated efficiently. Ultimately, the phase-matching constraint effectively reduces the scaling law for the harmonic cutoff energy to the phase-matching cutoff [160]:

$$E_{PMC} \propto \lambda^{(1.6-1.7)} \tag{1.89}$$

1.4.4 Quasi-Phase-Matching

Even if the driving laser pulse has enough intensity to result in very high single atom cutoff energies, perfectly phase-matched emission would be impossible at any energies that exceed E_{PMC} (using a standard single-beam geometry). It is possible to bypass the phase-matching cutoff using a technique called quasi-phase-matching (QPM). Through QPM, the ionization limitation η_c can be exceeded to result in a nonzero phase-mismatch ($\Delta k \neq 0$), resulting in a finite coherence length

L_{coh}. Typically, this scenario would result in the coherent buildup of harmonic light during the first portion of the medium (up to L_{coh}), but in the next length of medium ($L_{coh} < z < 2L_{coh}$) any additional generated harmonic light would deconstructively interfere with the existing harmonic emission. To reduce or avoid the cancellation effect in this second region of the medium, the phase-mismatch Δk can be altered or the harmonic emission can be shut off in this latter region. By repeating this process in a periodic way, the total harmonic emission at photon energies that are conventionally unachievable can grow to moderately bright levels.

A simple model of the generation of harmonic light can be modeled as follows:

$$E_q \propto \int_0^{L_{med}} A_q e^{-i\Delta k z} dz, \tag{1.90}$$

where A_q represents the transverse spatially- and time-integrated dipole emission strength per unit length of the HHG process of order q. In QPM, an additional factor is included in the integral:

$$d(z) = d_{eff} \sum_{m=-\infty}^{\infty} G_m e^{iK_m z}, \tag{1.91}$$

where $K_m = 2\pi m/\Lambda$ is the effective wavevector of the QPM scheme, m is the order of the QPM process, and d_{eff} and G_m are amplitudes that allow $d(z)$ to be a general periodic function. Defining $\Lambda = 2L_{coh}$ and adding $d(z)$ to Eq. (1.90) reveals that the brightest harmonic emission occurs for $K_1 = \Delta k$ and $G_m = \delta_{m,1}$. However, enhanced emission can occur for higher order QPM (odd values of m). Ultimately, the phase-mismatch equation is modified in QPM:

$$\Delta k_{QPM} = \frac{\pi}{L_{coh}} = \Delta k_{medium} + \Delta k_{geometry} - K_m \tag{1.92}$$

Larger values of K_m (smaller periodicity Λ) can compensate for a larger conventional Δk, and therefore higher levels of ionization within the medium.

There are various approaches to achieve QPM. Periodic modulation of the medium can be achieved through waveguides with longitudinally-varying radii and through pressure modulations created by multiple gas sources (successive gas jets or alternating gas supply/pump holes in a waveguide). Additional light waves can also be implemented to achieve QPM [24, 176]. These schemes are shown in Fig. 1.24.

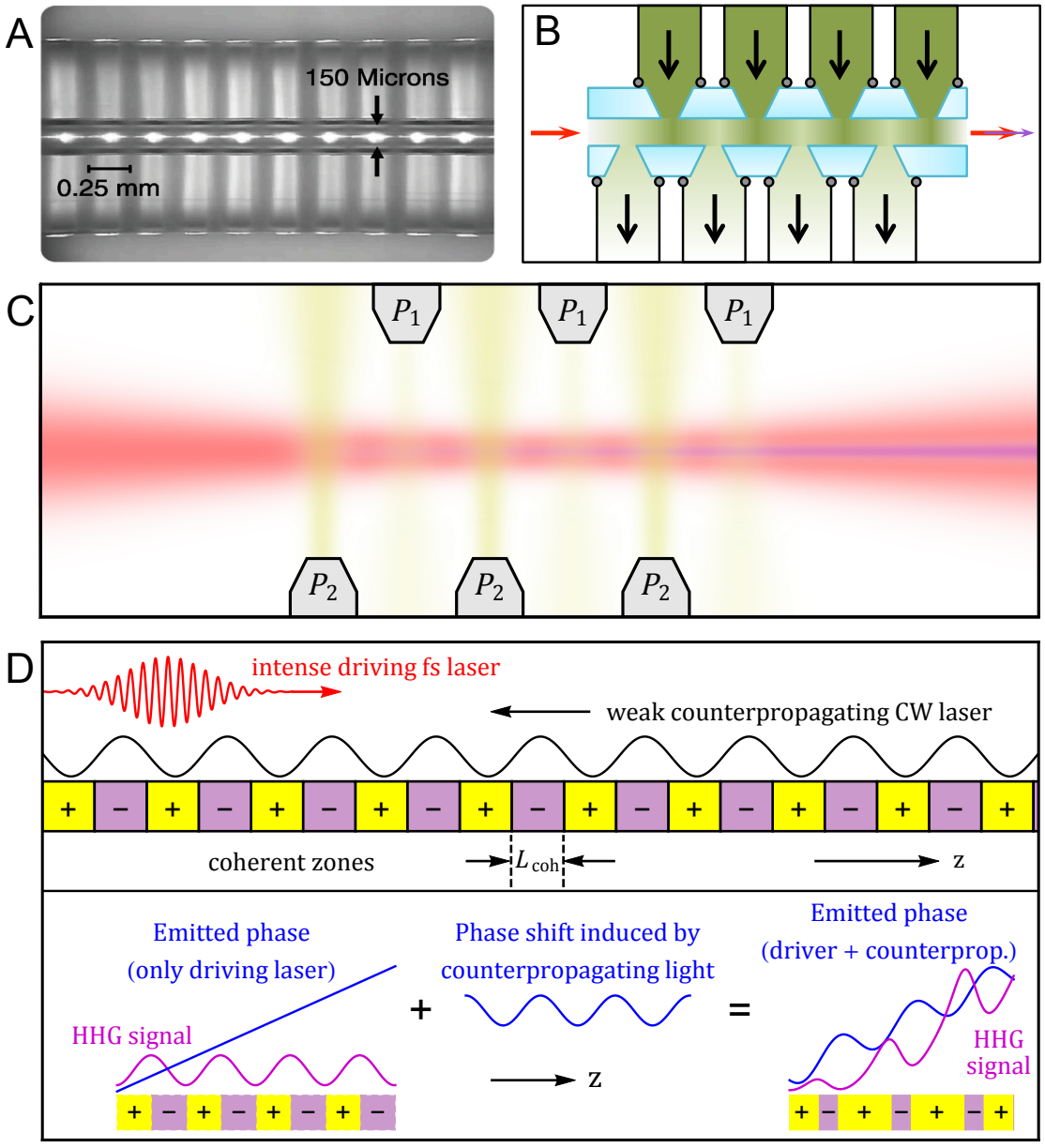

Figure 1.24: QPM schemes for HHG. (A) Waveguides with modulated inner diameters [93, 136]. (B) Pressure modulation in waveguides. (C) Pressure modulation through successive gas jets [147]. (D) Grating-assisted phase-matching through counterpropagating CW laser light (adapted from [24]).

Table 1.4: A table of absorption lengths for light with various photon energies propagating through a number of gases relevant to HHG. The gas pressure is 1 atm in all cases.

	$L_{abs,0}(E)$					
E	He	Ne	Ar	Kr	Xe	Air
30 eV	7.2 µm	4.5 µm	1.5 µm	2.4 µm	5.2 µm	9.3 µm
100 eV	93 µm	9.8 µm	30 µm	17 µm	1.5 µm	201 µm
300 eV	2.3 mm	108 µm	13 µm	10 µm	24 µm	37 µm
500 eV	11 mm	408 µm	34 µm	21 µm	39 µm	55 µm
1 keV	1.0 m	156 µm	181 µm	99 µm	19 µm	231 µm

1.4.5 Reabsorption

In the macroscopic picture of HHG, the generation and coherent superposition of harmonic light is only part of the full story. Harmonic light is also reabsorbed by the same medium that generates it. To accurately predict the final harmonic flux from a medium, one must consider generation, phase-matching, and reabsorbtion simultaneously. Constant *et al.* provide a simple 1-D approach to model the harmonic flux as a function of longitudinal position [25]. Their analysis assumes a constant phase-mismatch, but can be extended to longitudinally-varying mismatch (i.e. pressure profile) as is investigated here.

The transmission of harmonic light through an absorbing medium can be determined using data from the Center for X-ray Optics (CXRO) database [63]. For a gas at a given pressure P and light at a particular photon energy E, one can define an absorption length $L_{abs}(E,P)$ for the medium through which the transmission is $1/e$. Table 1.4 lists absorption lengths for several gases and photon energies at a pressure of 1 atm, which we define as $L_{abs,0}(E) = L_{abs}(E, 1\text{atm})$. To calculate the absorption length of a medium at a different pressure: $L_{abs}(E,P) = \left(\frac{1\text{ atm}}{P}\right) L_{abs,0}(E)$. To calculate the transmission of a gaseous medium with length L_{med} at pressure P:

$$T(E,P,L_{med}) = e^{-L_{med}/L_{abs}(E,P)} \tag{1.93}$$

The simplest 1-D approach to calculate the harmonic flux level at the exit of a uniform gaseous medium is straightforward; the electric field output is simply the integrated sum of the emission for all points along the medium, where each differential position has a local emission amplitude ρA_q

and propagation factor that simultaneously accounts for phase-mismatch and reabsorption:

$$exp\left\{-\left(\frac{1}{2L_{abs}(E,P)}+i\Delta k\right)(z-L_{abs})\right\} \tag{1.94}$$

Ultimately, the harmonic flux is:

$$\frac{\omega_q}{4c\epsilon_0\hbar}\left|\int_0^{L_{med}}\rho A_q\ exp\left\{-\left(\frac{1}{2L_{abs}(E,P)}+i\Delta k\right)(z-L_{abs})\right\}dz\right|^2 \tag{1.95}$$

For a medium with constant pressure and driving laser, the integral evaluates to:

$$\rho^2 A_q^2 \frac{4L_{abs}^2}{1+4\pi^2(L_{abs}/L_{coh})^2}\left[1+exp\left(-\frac{L_{med}}{L_{abs}}\right)-2\cos\left(\frac{\pi L_{med}}{L_{coh}}\right)exp\left(-\frac{L_{med}}{2L_{abs}}\right)\right] \tag{1.96}$$

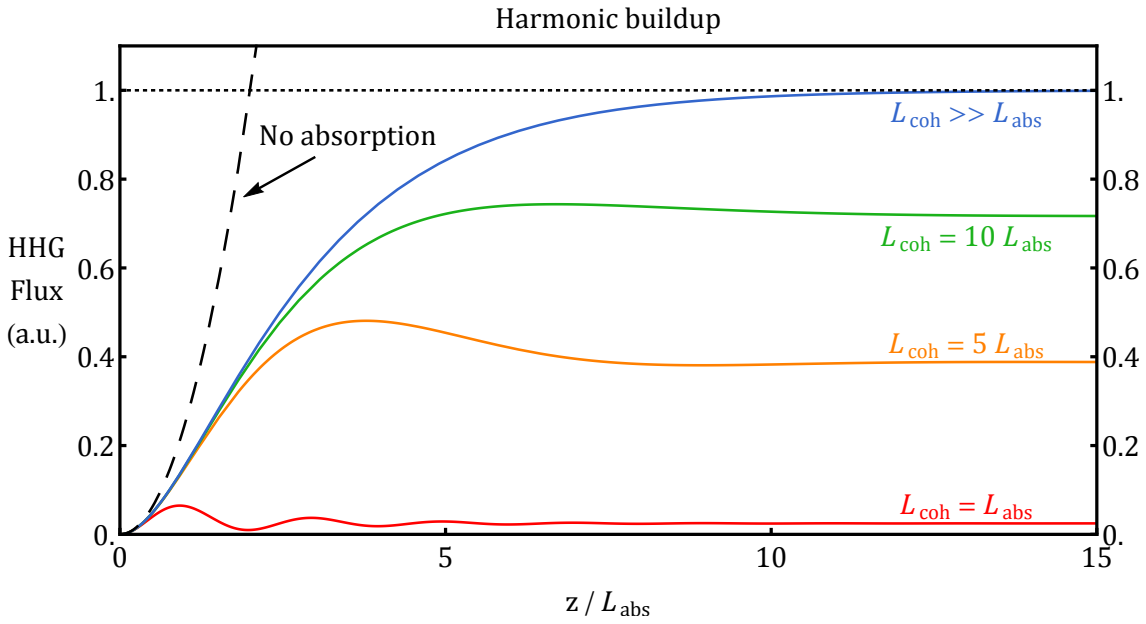

Figure 1.25: Plots of the accumulation of HHG flux as a function longitudinal position within the HHG medium. The ratio between the absorption length L_{abs} and coherence length L_{coh} are varied. For perfect phase-matching, the HHG flux saturates after $\approx 10L_{abs}$.

Equation (1.96) is useful in understanding the general behavior of the harmonic buildup for a variety relative values for L_{abs}, L_{coh}, and L_{med}. Figure 1.25 shows various regimes of harmonic generation along the longitudinal direction. However insightful, Eq. (1.96) is valid for constant medium and driving conditions. In reality, the medium will have a varying pressure profile, and

the driving laser can change in intensity. Maintaining the 1-D dimensionality of the problem but adding the longitudinal variations, Eq. (1.95) can be modified:

$$\frac{\omega_q}{4c\epsilon_0\hbar}\left|\int_0^{L_{med}}\rho(z)A_q(z)\ exp\left\{-\left(\frac{z-L_{med}}{2\overline{L_{abs}}(E,z)}+i\phi_q(z)\right)\right\}dz\right|^2 \tag{1.97}$$

Here, $\overline{L_{abs}}(E,z)$ represents the average absorption length for the remainder of the medium from z to L_{med}, and $\phi_q(z)$ is the exit phase of the harmonic emission from position z. Numerical evaluation of Eq. (1.97) is straightforward to perform in a step-wise manner. The details of the calculation involve keeping track of the total harmonic flux in each differential section dz, adding to it the emission from that section, developing its phase according to the local index, and reducing its magnitude as a result of reabsorption from that section.

1.4.6 Characteristics of Macroscopic HHG Emission

The importance of phase-matching during HHG cannot be underestimated. Applications of the HHG light source typically require a high level of photon flux for sufficient signal-to-noise ratios in the experiment. Phase-matching must be satisfied, so the limitations associated with the phase-matching constraint are unavoidable in standard, single-beam HHG geometries. Equation (1.89) describes one macroscopic limitation. The cutoff photon energy cannot scale as favorably as in the single-atom picture $\sim I_L\lambda_L^2$. Instead, the phase-matching constraint reduces the scaling to $\sim \lambda^{(1.6-1.7)}$ [160]. This scaling has been experimentally verified, as demonstrated in Fig. 1.26. It is possible to overcome the macroscopic cutoff energy limitations through multi-beam geometries, which will be further investigated in Section 5.3.

Another macroscopic effect is the ability to preferentially select particular trajectories in a Gaussian free-focus geometry. Depending on the location of the gas jet with respect to the focus, long or short trajectories can be preferentially phase-matched, as described in Section 1.4.3.

The effect of reabsorption within the HHG medium limits the harmonic flux that can be achieved. Even in perfect phase-matching conditions, the harmonic signal saturates after a distance of $\sim 10L_{abs}$. Furthermore, realistic experimental conditions will have pressure profiles that vary

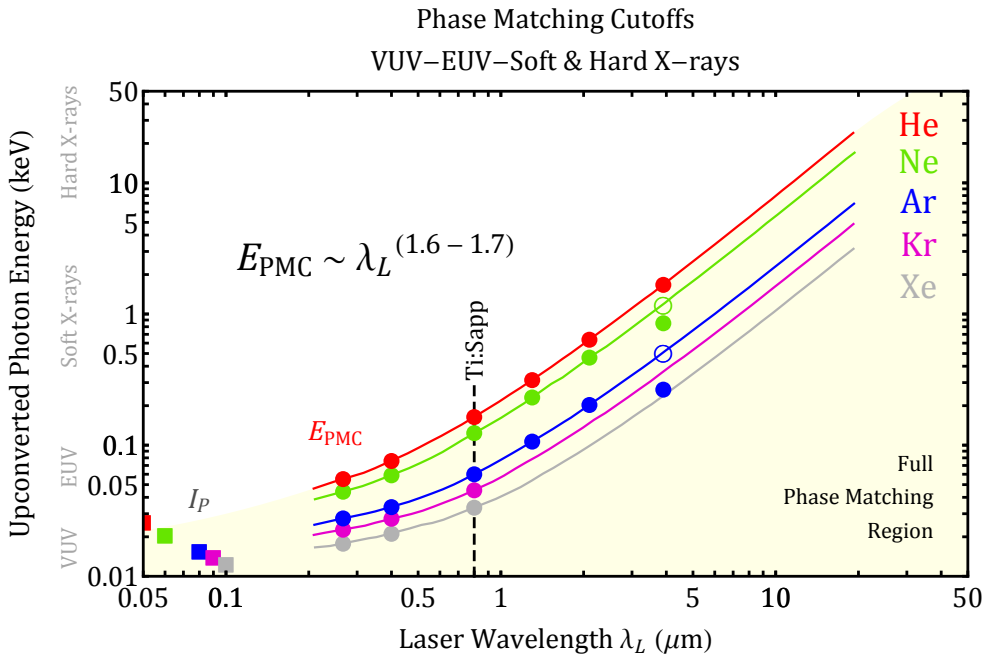

Figure 1.26: Experimentally-verified scaling of the macroscopic HHG cutoff photon energy E_{PMC} as a function of driving laser wavelength. Open circles represent the predicted harmonic cutoff without reabsorption limitations that are present during experiment. Adapted from [160].

longitudinally. Even if a constant pressure region can be created for perfect phase-matching, there will be a subsequent transition region before vacuum is reached. The transition region will have reabsorption without phase-matched generation, again limiting the practical flux achievable.

Finally, the phase-matching constraint has two main contributions that must cancel: $\Delta k_{geometry}$ and Δk_{medium}. We have shown that the medium contribution can be positive or negative depending on the ionization content. As the driving wavelength is increased, the index of refraction $n(\lambda_L)$ for the driving field generally approaches unity (far from resonances). This results in a decreased value of $\Delta\delta^0$. Since the atom contribution is proportional to $\Delta\delta^0$ as well as λ_L^{-1}, while the plasma contribution is proportional to λ_L, the critical ionization level decreases for increasing λ_L. Another consequence is that for a given geometry and ionization level $\eta < \eta_c$, there is a route to achieve phase-matching through the gas pressure $\bar{P}$. However, the geometric term tends to increase in magnitude with λ_L, which ultimately results in the phase-matching pressure $\bar{P}_{PM}$ increasing with λ_L. Figure 1.27 indicates this pressure dependence on wavelength.

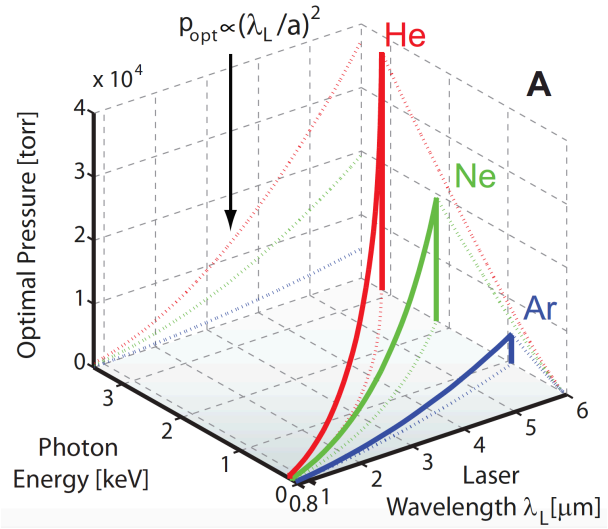

Figure 1.27: Pressure and harmonic cutoff energy scalings with driving laser wavelength. The predicted optimal pressure shows quadratic growth with λ_L. Adapted from [106].

Chapter 2

Phase-Matching Gating during Mid-IR Driven HHG

[1] Once the conceptual and mathematical framework of the microscopic and macroscopic physics of HHG had been developed, the scaling laws revealed a clear route to pushing the technology to higher photon energies. More dramatic frequency conversion could occur according the scaling of the cutoff harmonic photon energy with driving laser wavelength: $E_{PMC} \propto \lambda^{(1.6-1.7)}$. Experiments using long wavelength drivers have been designed in order to investigate the spectral capabilities and limitations of the HHG process.

Due to the need for ultrafast pulses for phase-matched HHG, and due to the lack of conventional laser oscillators that are ultrafast and operate beyond the near-infrared region, one of the most practical approaches to achieve appropriate mid-infrared drivers is through optical parametric amplification (OPA). In OPA, an ultrafast pulse with near infrared or visible wavelength is used to pump a second-order nonlinear frequency conversion process. The energy of a single pump photon gets split between two photons with tunable wavelengths. Thus, an input laser pulse with short wavelength can be converted into two output laser pulses with longer wavelengths (signal and idler beams). In this chapter, an experiment will be discussed in which two OPA output wavelengths were utilized. Ultrafast laser light with wavelengths between 1.2 µm and 2.4 µm were achieved through the use of an 800 nm-driven OPA (Light Conversion HE:TOPAS). Signal light at 1.3 µm and idler light at 2.1 µm were chosen for this study.

[1] The experiment and results described in this chapter are published in [18].

2.1 Grating Spectrometer Limitations

As described in Section 1.2.4, HHG emission in the temporal domain has a number of characteristics. First, the half-cycle symmetry of the HHG process results in bursts of harmonic pulses every half-cycle of the driving laser. Thus, a pulse-train of HHG is emitted in the microscopic picture. Consequently, the spectral domain contains signatures of the interferences between the individual pulses in the time domain, indicated by the odd harmonic spectral peaks. In many low-order spectroscopy experiments, observation of these odd harmonics is common. However, the spectrometer in the experiment must have sufficient spectral resolution to identify individual harmonics, as opposed to measuring a broad continuum. For visible and near-infrared driven HHG, this resolution requirement is not an issue; the moderate-energy driving photons cause the separation between odd harmonics to be relatively large, while the phase-matching cutoff energy makes the total HHG spectral range to be relatively small. Thus, CCDs with 1024 pixels along one dimension can easily span the spectral range while resolving individual orders. Assuming a nearly-linear dispersion of the spectral orders, the requirement for a CCD to adequately resolve individual harmonics while spanning the entire HHG bandwidth is given by:

$$\frac{E_{PMC}}{\hbar\omega_L} \leq \frac{N_s}{2}, \tag{2.1}$$

where N_s is the number of sample points in the spectral domain (the number of transverse pixels on a CCD).[2] Additionally, a grating spectrometer's ultimate resolving power depends strongly on the number of illuminated grating grooves, the apertures, and any aberrations added to the beam by optical elements.

Moving to longer wavelength drivers in the mid-IR causes the HHG spectral range to increase while the harmonic orders become less separated. To then satisfy Eq. (2.1), the number of spectral sampling points N_s must increase. Using the scaling law described in Eq. (1.89), N_s scales as $\lambda_L^{(2.6-2.7)}$. In practice, satisfying this requirement is difficult. As demonstrated in [161] where 3.9

[2] It is possible to alleviate this constraint by performing a panoramic spectrum measurement, where the spectral area of interest is scanned. This measurement, however, may contain complications if there is a need to use multiple gratings with varying spectral efficiencies in different spectral ranges.

µm drivers generated soft X-ray light up to 1.6 keV, the very broad measured spectrum could not resolve individual harmonic orders. Therefore, it is unclear whether the harmonics in that experiment truly possessed a broadband super-continuum spectrum (and thus a single, isolated burst of HHG), or whether individual harmonics were indeed present (indicating a pulse-train of harmonics in the time domain). In response to this uncertainty, a new experiment was designed that would investigate the temporal and spectral domains simultaneously. This would be possible through measurement of the electric field autocorrelation of the HHG signal for a variety of driving laser conditions.

One powerful technique for characterizing the ultrafast temporal structure of a laser pulse is through Frequency-Resolved Optical Gating (FROG). FROG describes an intensity autocorrelation measurement that relies on the nonlinear response of an optical medium to measure both the amplitude and phase of the laser pulse, both of which are required to obtain a full characterization of the temporal structure of the pulse [164]. This technique requires a nonlinear medium with high transmission at the laser wavelength. Unfortunately, such media do not exist for EUV and X-ray light, making standard FROG measurements for HHG impractical. Alternative approaches exist that can indirectly measure the amplitude and phase of HHG light, such as attosecond streaking [144]. However, for the purposes of determining whether a train of HHG pulses exists (and a corresponding spectral supercontinuum) the full amplitude and phase are not absolutely necessary. Instead, a high-resolution measurement of only the spectral amplitude can be adequate when paired with knowledge of the coherent nature of the HHG driver and its emission. The first component of this formula can be obtained through an electric field autocorrelation measurement of the HHG emission.

2.2 Electric Field Autocorrelation

In an electric field autocorrelation, a laser pulse is interfered with a delayable duplicate of itself. When the two pulses are not overlapped in time, the incoherent sum of their energies is measured on the detector. When overlapped, the interference between the electric fields will

increase or decrease the measured signal. Mathematically, the measured intensity is:

$$I_M(\tau) = \int_{-t_I/2}^{t_I/2} |E(t) + E(t-\tau)|^2 \, dt \tag{2.2}$$

Here, t_I is the integration time of the detector, and τ is the temporal delay between the two laser pulses ($t_I >> \tau$). Expanding Eq. (2.2) yields:

$$\begin{aligned} I_M(\tau) &= \int_{-t_I/2}^{t_I/2} \left(|E(t)|^2 + |E(t-\tau)|^2\right) dt \\ &+ \int_{-t_I/2}^{t_I/2} E(t)E^*(t-\tau)dt + \int_{-t_I/2}^{t_I/2} E^*(t)E(t-\tau)dt \\ &= 2I_0 + A(\tau) + A^*(\tau) \end{aligned} \tag{2.3}$$

Thus, the measured signal on the detector is the sum of the pulses' average intensities (I_0) plus the field autocorrelation function $A(\tau)$ and its complex conjugate. According to the Wiener-Khinchin theorem, the Fourier transform of $A(\tau)$ is the power spectrum of $E(t)$ (though the spectral phase cannot be extracted through $A(\tau)$). Measurement of $A(\tau)$ is the basis for Fourier transform spectroscopy.

The electric field autocorrelation of the HHG signal provides a solution to the challenge of a spectral measurement with simultaneously high resolution and range. These characteristics of the measurement do not rely on a physical number of CCD pixels, but instead rely on the number and spacing of delays τ. For a measurement with N_τ delay positions, each spaced $\delta\tau$ apart (giving a temporal range $\Delta\tau = N_\tau \delta\tau$), the spectral range ΔE and spacing δE that can be achieved are:

$$\begin{aligned} \Delta E &= \frac{2\pi\hbar}{\delta\tau} \\ \delta E &= \frac{2\pi\hbar}{\Delta\tau} = \frac{2\pi\hbar}{N_\tau \delta\tau} \end{aligned} \tag{2.4}$$

2.3 HHG Pulse Train and Coherence

For a particular half-cycle of the driving laser pulse, electrons will tunnel ionize, propagate, and recombine during the following half-cycle. In the quantum picture of HHG, emission results from two parts of the electron wavefunction interfering with themselves. Because both components of the electron wavefunction stem from the same initial state, there is a strong coherence between

the two portions and the quantum phase upon recombination should develop in a consistent way. Aside from possible scattering from adjacent atoms, there is no reason to believe decoherence should occur during the three step model. Additionally, the electron dynamics during the three-step model are inherently coupled to the driving laser dynamics, so it follows that the HHG emission will be coupled to and coherent with the driving laser. Finally, for a monochromatic driver, the microscopic picture of HHG should be consistent between neighboring half-cycles (aside from a sign-flip). As such, there is no reason to believe that a burst of harmonics originating from a given half-cycle should have a random phase offset compared to a neighboring harmonic burst. There can be phase shifts associated with a temporally-varying driving envelope or with chirped driving pulses, but these phase shifts would not be random. Therefore, there would be some amount of coherence between the different pulses within the train of HHG emission. In fact, the characteristic HHG spectrum that contains harmonics separated by $2\omega_L$ demonstrates that coherence must be maintained across different pulses in the HHG train (since random phase variations would wash out the modulations observed in the spectral domain).

This conclusion pertains to the measurement of the electric field autocorrelation since delaying the HHG pulse train with respect to itself will inevitably result in pulses overlapping and interfering with different pulses within the train. Consistent interference signatures would not be measurable if there were a mechanism for random phase decoherence between neighboring pulses. As an example, consider a train of $N+1$ pulses:

$$E_{train}(t) = \sum_{n=-N/2}^{N/2} E_n \; exp\left[-\frac{\left(t - n\frac{\lambda_L}{2c}\right)^2}{dt^2}\right] e^{i(\omega_q t + \phi_n)} \tag{2.5}$$

Here, each pulse has its own field amplitude E_n and absolute phase ϕ_n. Inserting this into Eq. (2.3):

$$I_M(\tau) = \left(\sum_{n=-N/2}^{N/2} I_{0,n} + A_n(\tau) + A_n^*(\tau)\right) + \left(\sum_{n\neq m} X_{nm}(\tau) + X_{nm}^*(\tau)\right) \tag{2.6}$$

where $A_n(\tau)$ is the individual field autocorrelation function for pulse n (neglecting all other pulses),

and:

$$X_{nm}(\tau) = \int_{-t_I/2}^{t_I/2} E_n E_m exp\left[-\frac{\left(t - n\frac{\lambda_L}{2c}\right)^2 + \left(t - \tau - m\frac{\lambda_L}{2c}\right)^2}{dt^2}\right] e^{i(\omega_q \tau + \phi_n - \phi_m)} dt \qquad (2.7)$$

The interaction between different pulses within the train (inter-pulse cross-correlations) is contained within X_{nm}, which will result in a nonzero contribution for delays near $\tau = l\frac{\lambda_L}{2c}$, where l is an integer spanning from $-N$ to $+N$, excluding 0. Considering the contributions from $A_n(\tau)$ and $X_{nm}(\tau)$, $P_M(\tau)$ will result in a total of $2N+1$ interference signatures (for $N+1$ pulses in the original train).

From a temporal perspective, the HHG field autocorrelation can provide a direct measurement of the number of pulses within the HHG pulse train. By removing the DC contribution ($\sum_n P_{0,n}$) and performing a Fourier transform, the HHG power spectrum is acquired. Thus, measuring the electric field autocorrelation is a powerful approach to probe temporal and spectral aspects of the HHG source with high resolution in both domains, despite the lack of temporal phase information. Although the field autocorrelation can measure spectral bandwidths (and thus transform-limited pulse durations), it cannot be used to measure the actual HHG pulse duration, which may be broadened due to chirp.

2.4 Experimental Apparatus

To drive the experiment, a 1-kHz Ti:sapphire laser is used to supply near-infrared 0.8 µm light. It is also used to pump a three-stage optical parametric amplifier (Light Conversion HE:TOPAS) to generate 1.3 and 2.0 µm light. All three wavelengths are then used to drive HHG in a 2-mm-long, Ar-filled gas cell in a Gaussian focus geometry (Fig. 2.1). Second-harmonic FROG was used to measure the pulse durations for all three driving wavelengths, and these were adjusted to ensure consistent $\sim$ 10 cycle pulses (24 fs at 0.8 µm - 9.5 cycles, 35 fs at 1.3 µm - 8 cycles, and 90 fs at 2.0 µm - 13.5 cycles). The resulting harmonic cutoff energies were used to estimate the laser peak intensities in the focus, using the single-atom cutoff scaling from Eq. (1.22). Optimal phase-matching was obtained via longitudinal translation of the focusing lens, which adjusts the focal position with respect to the medium (Section 1.4.3).

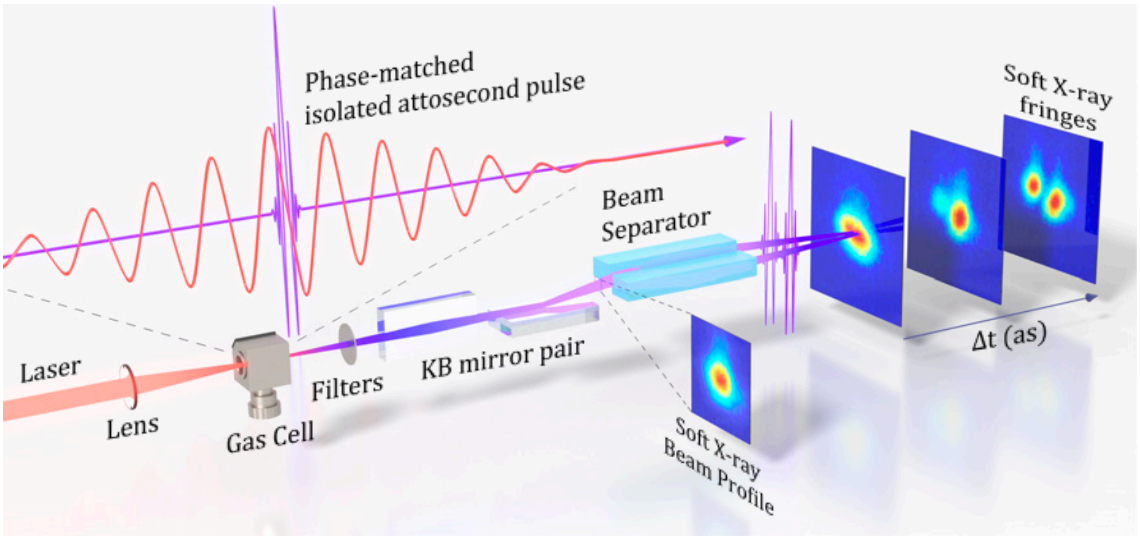

Figure 2.1: Experimental apparatus used to measure the HHG field autocorrelation. Phase-matched harmonics are generated in an Ar-filled cell, transmit through thin metal filters (eliminating the residual fundamental beam), refocused by a Kirkpatrick-Baez mirror pair, spatially split and temporally delayed by a beam separator, and finally measured on an X-ray CCD. Adapted from [18].

To perform the electric field autocorrelation, the HHG output was sent through a glancing incidence interferometer consisting of refocusing optics (a Kirkpatrick-Baez cylindrical mirror pair) and an in-line partially-split-mirror spatial beam separator. The separator is able to delay one half of the beam with respect to the other half with a temporal resolution of ~ 1.5 as (Fig. 2.1). After some propagation, the two halves of the HHG mode overlap and interfere at an X-ray CCD (Andor), where the field autocorrelation of the HHG pulse is acquired. Spatial fringes arise from the crossing of the two replicas of the HHG beam at the CCD. Because the beam is focusing as it reflects from the beam separator, each half of the mode will have opposing transverse wavevectors $\vec{k}_{1,x} = -\vec{k}_{2,x}$. At the CCD, the measured intensity is:

$$\begin{aligned} I_{CCD}(x,y) &= \left| E_1(x,y)e^{i(k_{1,z}z+k_{1,x}x-\omega_q t)} + E_2(x,y)e^{i(k_{2,z}z+k_{2,x}x-\omega_q(t-\tau))} \right|^2 \\ &= |E_1(x,y)|^2 + |E_2(x,y)|^2 + E_1(x,y)E_2^*(x,y)e^{i(2k_{1,x}x-\omega_q\tau)} + c.c. \end{aligned} \tag{2.8}$$

The third term and its complex conjugate result in a spatial modulation factor $\cos(2k_{1,x}x - \omega_q\tau)$. As τ is varied, the absolute phase within the cosine will change, shifting the observed fringes along the x-direction.

To extract the autocorrelation, the amplitude at a single pixel on the CCD could be monitored as a function of delay, yielding a signal of the form described in Eq. (2.6). However, the selection of a single pixel is fairly arbitrary and does not make use of the information gathered by other pixels. An effective alternative would use all of the modulation information, which can be obtained through the use of a spatial Fourier transform of the CCD image. The result will be an image in the spatial frequency domain, where there will be a large DC peak corresponding to $\mathfrak{F}\{|E_1(x,y)|^2+|E_2(x,y)|^2\}$, as well as two side peaks corresponding to $\mathfrak{F}\{\cos(2k_{1,x}x - \omega_q\tau)\}$. By extracting the amplitude and phase of one of these side peaks as a function of τ, the field autocorrelation function $A(\tau)$ is immediately obtained. Figure 2.2 shows an example of this procedure using real data. This technique can improve the fidelity of the autocorrelation because the side peaks represent the integrated modulation signal across the entirety of the overlap area of the crossed beams.

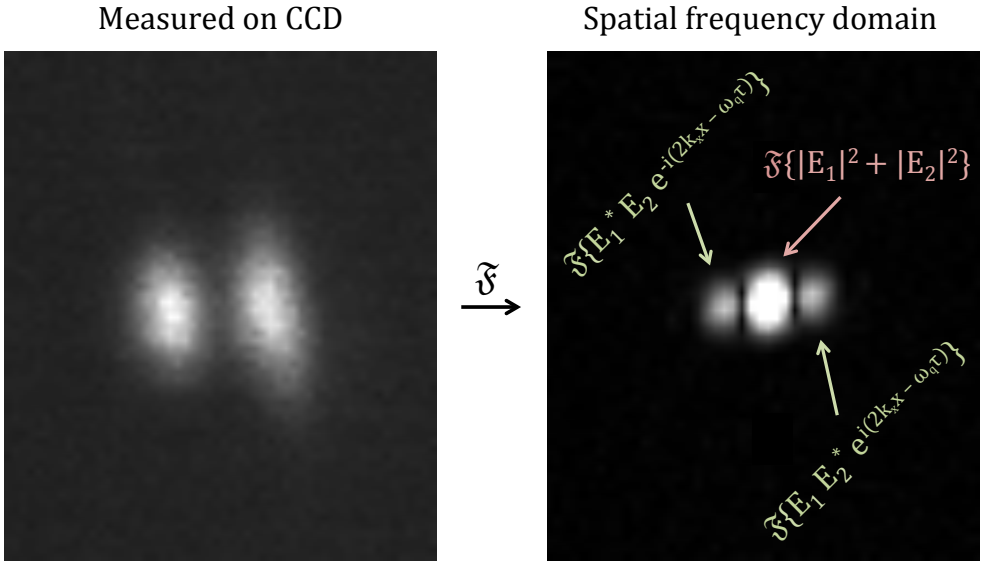

Figure 2.2: Spatial interference measured on a CCD from an HHG beam crossed with a replica of itself for a single delay τ. Performing a Fourier transform yields three peaks: one corresponding to the DC signal and two from the modulation signal. A single side peak contains information about the field autocorrelation function $A(\tau)$.

2.5 Field Autocorrelation Results

Figure 2.3 shows the measured HHG field autocorrelations and the resulting spectra (via Fourier transforms) using low and high laser intensity conditions for each of the three driving laser wavelengths mentioned above. The HHG cutoff energy and flux from Ar was optimized through the driving intensity, which identifies the high-intensity case that is plotted. Reducing the intensity to shift away from optimal HHG conditions then gives the results for the low-intensity case. For a 0.8 µm driver, the low and high intensities are 1.5×10^{14} and 2.6×10^{14} W/cm^2, which result in 15 and 9 X-ray bursts observed in the autocorrelation, respectively. For a 1.3 µm driver, the low and high intensities are 1.3×10^{14} and 2.1×10^{14} W/cm^2, which result in a faster reduction in measured X-ray bursts: 9 to 4. Finally, for a 2 µm driver, we measure a single isolated burst of harmonics for the high intensity case of 1.6×10^{14} W/cm^2. Furthermore, the single burst case (high intensity) corresponds to higher HHG flux than the HHG pulse train case (low intensity). The HHG spectrum from the 2 µm, high-intensity driver spans from 90 to 180 eV with a FWHM bandwidtih of $\sim$ 60 eV. This spectrum has a transform-limited pulse duration of $\sim$ 35 as, verified by the measured electric field autocorrelation that has a 70 as FWHM (as expected for Gaussian-like pulses). As discussed through Fig. 1.14, the HHG emission is expected to be emitted with linear chirp, giving a predicted pulse duration of $\sim$ 300-as (discussed below). To our knowledge, our temporal/spectral measurement of the 2 µm, high-intensity driven HHG has, to date, the highest photon energy and broadest bandwidth of any measured isolated attosecond pulse [112]. Following suggestions by previous experiments [123, 143], we also have concluded that the HHG spectrum and number of pulses are not dependent on the carrier-envelope phase (CEP) of the driving laser, since the CEP of the 2 µm laser was varied in our experiment with no observed change.

We assert that as long as the harmonic emission maintains pulse-to-pulse coherence (as described in Section 2.3 and being consistent with previous studies of HHG [94, 90]), then the field autocorrelation measurements presented here are sufficient to support the wavelength and intensity scalings of a phase-matching gating effect in the temporal domain, as detailed in the next

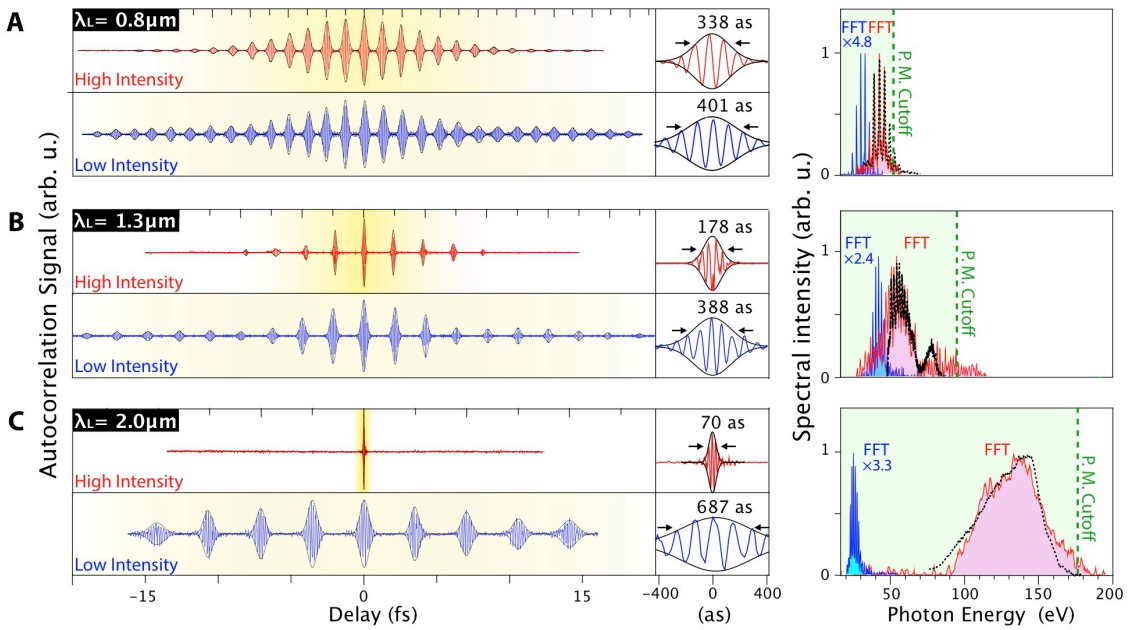

Figure 2.3: Comparison of the measured HHG field autocorrelation data from Ar, driven by ~ 10 cycle laser pulses at wavelengths of (A) 0.8 μm, (B) 1.3 μm, and (C) 2 μm under high and low laser intensity conditions (red and blue lines) described in the text. (Left) Field autocorrelation of the HHG field and enlarged view near time 0 with the coherence time of the central pulse envelope. The temporal phase-matching window is highlighted in yellow. Note that the bandwidth-limited pulse duration is half of this coherence time. (Right) HHG spectra obtained from the FFT of the field autocorrelation traces (filled-area plots), showing excellent agreement with the spectra obtained using a Hettrick grating spectrometer (black dotted lines). The low-intensity spectra are enhanced to see their harmonic structure. The predicted phase-matching cutoffs are indicated by green dashed lines. Adapted from [18].

section. This assertion, reliant on the temporal coherence of the harmonic emission, is further supported by the high level of spatial coherence measured across the entire beam of phase-matched HHG driven by mid-IR lasers [149, 161, 155]. Additionally, simulations have been performed to represent the unphysical case of drastically different chirps between neighboring HHG bursts. Even in these simulations, the electric field autocorrelation would contain indications of multiple pulses interfering at the detector.

Presented as an alternative to attosecond streaking, the field autocorrelation gives a direct measurement of the number of pulses in the HHG train (i.e. a total of $2N + 1$ fringes will be measured if there are $N+1$ bursts in the pulse train). This can be useful in providing fast feedback in the experiment when optimizing the HHG source. Observing a supercontinuum spectrum from a grating spectrometer could be considered for fast feedback, but the spectrometer's resolution would need to be able to sufficiently resolve individual harmonics. Due to the limitations of grating spectrometers explained in Section 2.1, the field autocorrelation could be more effective, especially for harmonics driven by long wavelength, low individual photon energy lasers. Through the fast Fourier transform (FFT), the spectral resolving power is governed by Heisenberg's uncertainty relation: $\delta E = 2\pi\hbar/\Delta\tau$, where δE is the FFT spectral resolution and $\Delta\tau$ represents the maximum temporal delay range. Our spatial beam separator is capable of a delay range of $\Delta\tau \sim 300$ fs, corresponding to an impressive spectral resolution of $\delta E \sim 0.01$ eV (2.0 µm driven odd harmonics would be separated by 0.62 eV). This level of spectral resolution is necessary to unambiguously determine whether the HHG spectrum contains individual harmonics or is supercontinuous, particularly since mid-IR driven HHG can contain orders up to 5,000 [161]. Finally, this technique directly probes the temporal domain, giving insight into the dynamic phase-matching conditions of the HHG process and its trends with driving intensity and wavelength.

2.6 Phase-Matching Gating Theory

The decreasing trend in number of pulses within the HHG pulse train as the driving wavelength and intensity are increased can be explained through a dynamic picture of phase-matching.

Phase-matching is supported only during a narrow temporal window within the laser pulse. On the leading edge of the laser pulse, the laser phase velocity $v_\phi < c$ (speed of light) due to the dominance of neutral atoms. In contrast, on the trailing edge, the laser phase velocity $v_\phi > c$ due to ionization of the gas beyond the critical ionization level, which terminates phase matching [160]. In the case of mid-IR driving lasers, three factors lead to a much shorter phase-matching window compared with 0.8 µm lasers: the harmonic order is higher, the period of the driving wave is longer, and the phase-matching pressure and ionization density are higher. Each of these factors contributes to a larger phase shift within each half-cycle and, therefore, to a shorter phase-matching window (Fig. 2.4). In contrast, for laser intensities below the critical ionization limit, optimal pressure and ionization are low, the harmonic order is low, and phase matching extends over many laser cycles. The practical consequence of this physical scaling is that for any driving laser wavelength, the temporal phase-matching window can be narrowed by increasing the driving laser intensity and gas pressure. However, for longer driving laser wavelengths, the temporal narrowing effect is much stronger, making isolated attosecond pulse generation more robust and natural.

The phase-matching theory detailed in Section 1.4.1 supports these findings when calculated dynamically. The terms of the phase-mismatch equation that vary with respect to time are those that have dependence on the ionization level. Thus, Δk_{medium} is the only dynamic component to consider, while the geometric terms remain constant. Taking a temporal derivative of Equation (1.73) yields:

$$\begin{aligned} \frac{\partial \Delta k(t)}{\partial t} &\approx q\bar{P}\left[\frac{2\pi}{\lambda_L}\Delta\delta^0 + N_a r_e \lambda_L\right] \cdot \frac{d\eta_1(t)}{dt} \\ &\propto q\bar{P}\lambda_L \frac{d\eta_1(t)}{dt} \end{aligned} \tag{2.9}$$

The rate at which $\Delta k(t)$ sweeps past zero (compared to the period of the driver) provides an indication for the number of half-cycles that can be phase-matched. Note the neutral gas dispersion contribution in Eq. (2.9) is negligible compared with the free-electron dispersion contribution, especially for long-wavelength driving lasers. At low laser intensities, the harmonic order q and $d\eta_1(t)/dt$ are small, which suppresses phase-matching gating, in agreement with the data of Fig. 2.3

(low intensity autocorrelation). Near optimal phase-matching, the pressure $\bar{P}_{PM}$, and the central harmonic order q_{PM} scale by the laser wavelength as $\bar{P}_{PM} \propto \lambda_L^2$ and $q_{PM} \propto \lambda_L^{2.7}$, as have been observed experimentally [160, 149, 161]. The scaling of q_{PM} arises from two contributions: a factor of $1/2 \cdot \lambda_L^{1.7}$ because the central energy of the attosecond burst is half the phase-matching cutoff [160], and an additional factor of λ_L from the fundamental laser photon energy. Thus, under optimal phase-matching conditions, Eq. (2.9) can be approximated by $\partial \Delta k(t)/\partial t \propto \lambda_L^{5.7} \cdot d\eta_1(t)/dt$, which scales strongly with the wavelength of driving laser. The combined effects of higher pressures, higher harmonic orders, and stronger free-electron dispersion for long-wavelength driving lasers creates a large phase-mismatch jump between adjacent half-cycles of the driving laser. Note that the larger separation between half-cycles for long wavelength driving lasers further isolates the attosecond bursts. Consequently, a longer wavelength driving laser can much more easily induce strong phase-matching temporal gating. Figure 2.4 depicts the time-gated phase-matching effect using the conditions of the experiment.

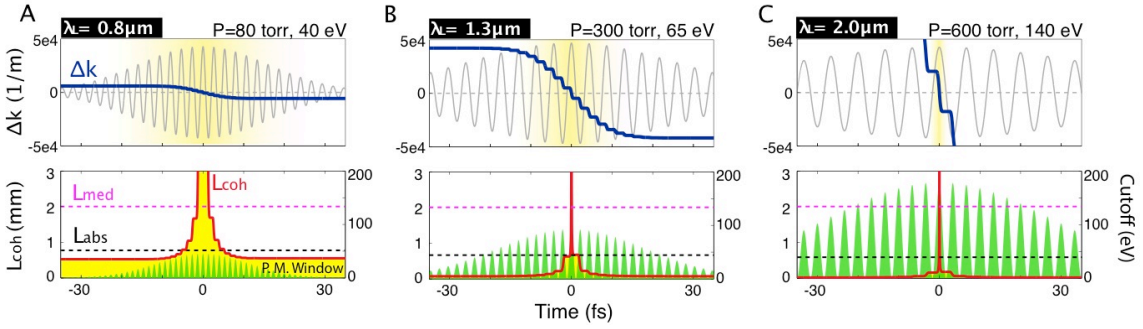

Figure 2.4: Calculated phase mismatch Δk (blue line), L_{coh} (red line and yellow highlight), and instantaneous HHG cutoff photon energy (green) for HHG in Ar driven by 10-cycle laser pulses: (A) 0.8 μm, 2.42×10^{14} W/cm^2; (B) 1.3 μm, 1.87×10^{14} W/cm^2; and (C) 2.0 μm, 1.5×10^{14} W/cm^2. The temporal window during which phase matching occurs is highlighted in yellow. Adapted from [18].

In addition to the analytic approach to understand the phase-matching gating effect, an advanced 3D numerical calculation was performed to simulate the microscopic generation of HHG and its macroscopic propagation to the detector. The gas medium is discretized into individual

radiators, whose emission is individually propagated to the detector:

$$E_j(r_d, t) = \frac{q_j \hat{\boldsymbol{s}}_{\boldsymbol{d}}}{c^2 |\boldsymbol{r_d} - \boldsymbol{r_j}|} \left[\hat{\boldsymbol{s}}_{\boldsymbol{d}} \times \boldsymbol{a_j} \left(t - \frac{|\boldsymbol{r_d} - \boldsymbol{r_j}|}{c} \right) \right] \tag{2.10}$$

where q_j is the charge of an electron at position j, $\hat{\boldsymbol{s}}_{\boldsymbol{d}}$ is the unitary vector pointing from that electron to the detector, and $\boldsymbol{r_d}$ and $\boldsymbol{r_j}$ are the position vectors of the detector and of the elementary radiator, respectively. Each radiation source has a dipole acceleration $\boldsymbol{a_j}$ that is calculated using SFA+, an advanced strong-field approximation (SFA) method [98]. $\boldsymbol{a_j}$ gives rise to coherent radiation that propagates at a phase velocity c to the far-field detector, where the coherent sum of all of the emitters' contributions is calculated. Macroscopic effects are incorporated into the calculation through the fundamental field, which exhibits time-dependent phase- and group-velocities. Dispersion from plasma and neutral atoms are considered, and Beer's law accounts for the reabsorption of the harmonics by the gas in the 2 mm argon gas cell assuming uniform density, for a variety of pressures. The 2 µm fundamental field was modeled using an 8-cycle FWHM Gaussian envelope in the time domain (53 fs). A peak intensity of 1.2×10^{14} W/cm^2 was chosen to satisfy phase-matching ($\Delta k = 0$) at the center of the pulse.

In Fig. 2.5, the HHG emission for single-cycle and multicycle drivers (1.5-cycle and 8-cycle pulses, respectively) are contrasted for low, moderate, and high pressures. Group velocity walk-off effects are evident in the single-cycle results, whereas strong phase-matching gating is observed for the multicycle case at high pressure. Figure 2.5 A-F show the fundamental laser field at the entrance and exit of the gas medium. For higher pressures and multicycle drivers, the neutral atom contribution is large for the front of the pulse, creating a phase shift at early times. The time-varying plasma content in the middle and end of the pulse creates a chirp for later times. These effects confine the temporal window over which phase-matching occurs, down to a suboptical cycle duration (300 as) near the center of the pulse. Figure 2.5 H reveals that an isolated attosecond HHG pulse is emitted with linear chirp (group delay dispersion ~ 0.005 fs^2). For high pressures and 1.5-cycle drivers, the group velocity walk-off causes the fundamental laser field envelope to shift away from the initial phase-matching window. Through propagation, the effective phase-matching

window is nonexistent, thus preventing bright HHG for the single-cycle case.

Group velocity walk-off does occur for longer duration drivers (Fig. 2.5 F), but the envelope varies slowly enough in intensity that the walk-off does not significantly reduce the phase-matching conditions at the center of the pulse. In both the low pressure (5 Torr, Fig. 2.5 G) and high pressure (600 Torr, Fig. 2.5 H) cases, the positive slope of the emission structure in chronocyclic space indicates the short electron trajectories are phase-matched (recall Fig. 1.14). Despite the chirp that stretches the HHG pulse to ~ 300 as, the phase-matched HHG bandwidth obtained from Fig. 2.5 H (~ 60 eV FWHM) corresponds to a transform-limited pulse duration of ~ 35 as. These spectral and temporal characteristics agree with the empirical measurements to a high degree.

2.7 Phase-Matching Gating Summary

In summary, we present an alternative method to measure the temporal and spectral characteristics of HHG emission through the use of an electric field autocorrelator. To our knowledge, we have observed the first isolated attosecond pulses measured in the soft X-ray region, with sufficient temporal resolution (1.5 as) to resolve individual harmonic bursts (and harmonic orders). Through phase-matching gating, we demonstrate the benefit of mid-IR lasers to naturally and robustly produce bright isolated attosecond pulses up to 180 eV. This also represents, to our knowledge, the first experimental verification of the time-dependent balance of plasma and neutral atom dispersions through a direct measurement of the HHG emission in the time domain. We present a new understanding of the wavelength, pressure, and intensity scalings of the phase-matching dynamics, which surprisingly indicate that efficient generation of bright isolated bursts of harmonics in the EUV necessitate multicycle driving pulses to avoid group velocity walk-off effects. Additionally, CEP-stabilization and few-cycle laser technologies are not necessary to produce stable, isolated attosecond pulses. It is predicted that this approach can be extended to generate single digit attosecond and even zeptosecond pulses in the keV region [105, 161]. Our results provide further insight into the attosecond physics of high intensity laser-matter interactions and frequency conversion driven by mid-IR laser light.

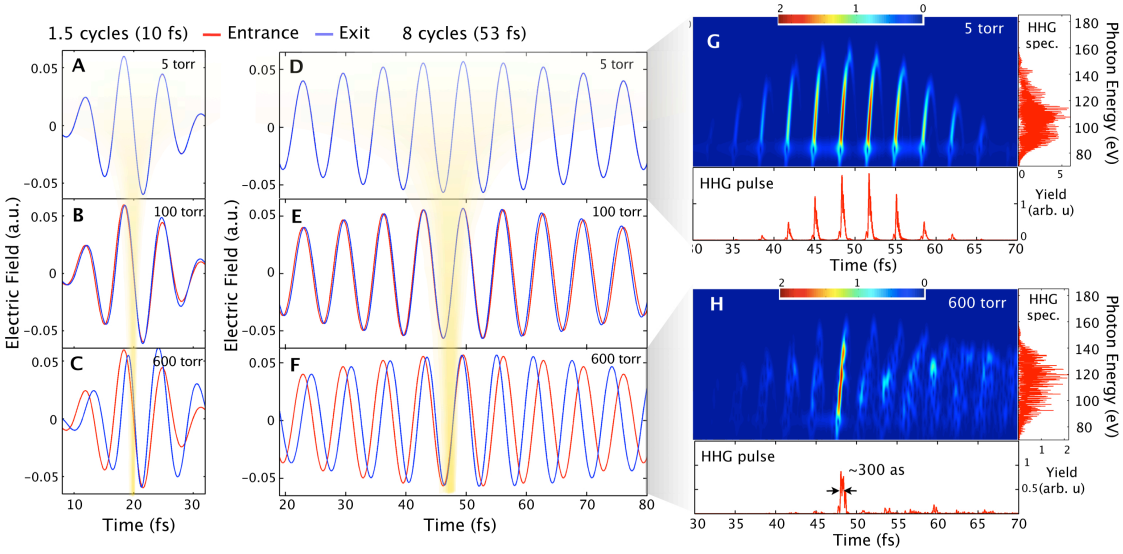

Figure 2.5: SFA+ calculations of microscopic and macroscopic HHG emission, demonstrating phase-matching gating and group velocity walk-off effects for 1.5-cycle and 8-cycle drivers at low (5 Torr), moderate (100 Torr), and high (600 Torr) pressures. For a 2 mm argon gas cell, entrance (red) and exit (blue) laser fields are plotted in A-F. Phase-matching intensities of 1.3×10^{14} W/cm^2 and 1.2×10^{14} W/cm^2 are used for the single- and multicycle fields, respectively. The driving laser mode was assumed to be a Bessel profile of radius 60 µm. The phase-matching gating window is highlighted in yellow. The HHG emission in chronocyclic space is plotted for the 8-cycle driver at (G) 5 Torr and (H) 600 Torr. Isolation of a 300 as chirped pulse occurs for the high pressure scenario (H). Phase-matching over an extended distance is not possible for a 1.5-cycle driver due to group velocity walk-off effects. Adapted from [18].

Chapter 3

Water Window and Soft X-ray HHG Spectroscopies

[1] Aside from the complex temporal aspects of mid-IR driven HHG, the spectral characteristics have been shown to follow the macroscopic cutoff scaling law from Eq. (1.89): $E_{PMC} \propto \lambda^{(1.6-1.7)}$. Mid-IR drivers are especially suitable for generating broad supercontinua with utility in spectroscopy applications. In this chapter, we demonstrate the use of table-top HHG sources for the spectroscopic interrogation of thin samples with absorption edges in the water window (defined by the K-edges of C and O: 284–541 eV) and soft X-ray regimes ($>$ 1 keV) (Fig. 3.1). The 1.2 - 2.4 µm output from the HE:TOPAS described in Chapter 2 is used, in addition to 3.9 µm idler light from a 1.064 µm pumped, 1.460 µm seeded OPCPA [139, 161]. Aside from HHG spectroscopies being useful in determining the elemental composition of unknown samples, the nanoscale atomic structure of pure samples can be revealed through a measurement called X-ray Absorption Fine Structure (XAFS). Three experimental XAFS measurements using the two aforementioned mid-IR HHG drivers will be detailed here.

3.1 XAFS Theory

Atomic absorption spectra contain sharp features corresponding to energetic transitions. From a single-atom perspective, electron transitions govern the spectral locations of the observed absorption edges. Photon absorption can result in electron transitions between bound orbitals as well as photoionization to continuum electron states. In molecules, elemental absorption edges and

[1] The experiment and results described in this chapter have been submitted for publication [135].

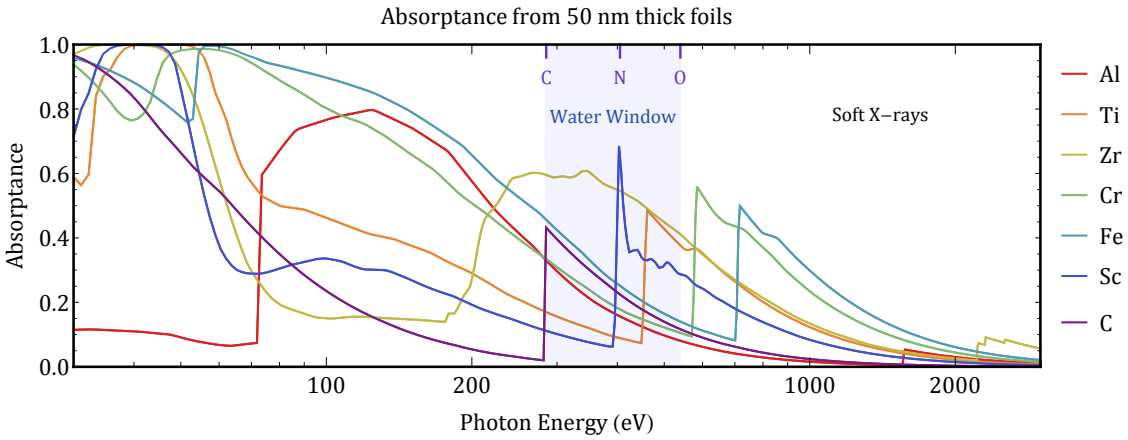

Figure 3.1: Absorption spectra for various elements in the water window and soft X-ray regimes. A material thickness of 50 nm is used for all curves. Data retrieved from the CXRO database [63].

the surrounding spectral structure can be modified due to the presence of neighboring atoms and the chemical bonds that are formed. Several molecular factors can influence the near-edge absorption structure (NEXAFS), such as oxidation and magnetic states, or localized charge to specific atoms in the molecule or lattice. Spectroscopic measurements near the absorption edge can give information about the electronic band structures, as well as orbital and spin ordering phenomena. The molecular orientation with respect to the incident light wave's polarization can also influence the NEXAFS measurement.

In ordered solids, atoms form a crystallographic lattice with consistent inter-atomic spacing. Even with one type of element present, the single-atom absorption spectrum can be modified due to the presence of neighboring atoms. This phenomenon can be understood in a three-step quantum model, where an atom absorbs an incident X-ray, causing it to eject a core-shell photoelectron. Scattering of the photoelectron from neighboring atoms leads to quantum interferences between the outgoing and incoming electron waves (Fig. 3.2). The interferences produce modulations in the X-ray absorption spectrum past the absorption edge, and can extend to significantly larger photon energies. The information contained within the interference structure is not limited to only single rescatterings, but can also be influenced mulitple scattering events. In the electron scattering picture, an XAFS function $\chi(k)$ can be used to model the absorption probability of the incident X-ray photon:

$$\frac{\mu - \mu_0}{\Delta\mu_0} = \chi(k) \cong \sum_i \frac{N_i f_i(k)}{kR_i^2} \sin(2kR_i + \delta_i(k)) e^{-2k^2\sigma_i^2 - 2R_i/\lambda(k)} \tag{3.1}$$

Here, the left hand side is measured experimentally; μ is the total absorption coefficient for the lattice or molecule, while μ_0 corresponds to the absorption from an isolated atom. The right hand side of Eq. (3.1) is the theoretical formula used to fit the data; different electron scattering paths labeled by i generate different modulation frequencies in the XAFS absorption spectra. $f_i(k)$ is the backscattering amplitude, N_i is the number of scattering atoms in a particular shell (Fig. 3.2), $\delta_i(k)$ is the total phase shift from both absorption and rescattering, $\lambda_i(k)$ is the electron mean free path, R_i is the half path length between the absorbing atom and the i coordination shell of

scattering atoms (for single scattering), σ_i is a disorder parameter, and k is the electron wave number: $k\left[\text{Å}^{-1}\right] \approx 0.512\sqrt{(E - E_{edge})[eV]}$.

Due to the tight packing of atoms within the lattice, the interferences occur on very short time scales. This results in long periodicity modulations in the spectral domain, requiring a broad spectral probe that extends well past the absorption edge to sufficiently resolve the modulations. Thus, measuring the fine structure of solid samples with Å-resolution is labeled extended-edge XAFS (or EXAFS). Figure 3.2 depicts the electron interferences and chemical environments that result in EXAFS and NEXAFS effects.

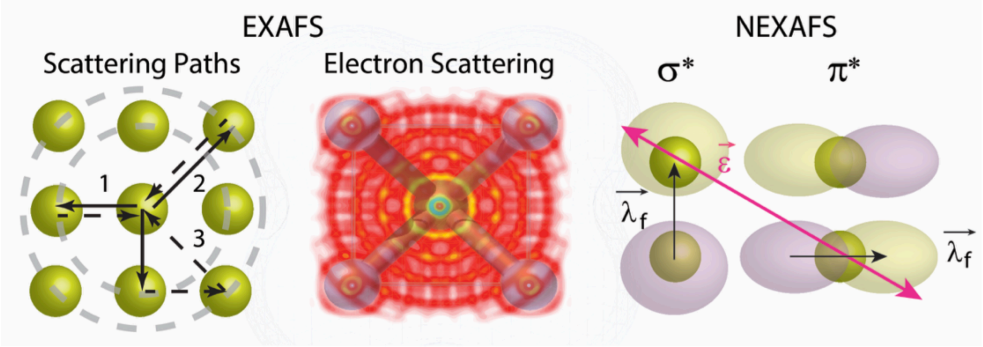

Figure 3.2: (Left) Illustration showing the scattering paths of photoelectrons from the first (path 1) and second shell (path 2), as well as secondary rescattering (path 3). (Center) Photoelectron scattering and interference of the electron-wave packet for a 2D planar lattice. (Right) XAFS sensitivity to the polarization $\vec{\epsilon}$ and final $\vec{\lambda}_f$ orbital direction. Adpated from [135].

3.2 NEXAFS in Polymers

To measure the NEXAFS signatures at the carbon K-edge near 284.2 eV, water-window HHG light is produced using an OPA pumped by a 19.5 mJ, 20 fs, 1 kHz repetition rate Ti:Sapphire laser. Because of the high peak intensities achievable with these laser specifications, nonlinear effects in air can prove detrimental to the experiment and OPA process. Thus, the 20 fs Ti:Sapphire pulses are stretched to $>$ 150 fs to reduce the peak intensity for beam paths before the OPA. The pulse is then recompressed just before each stage of the OPA using chirped mirrors. This allows the beam to maintain excellent mode quality and pulse shape for efficient generation of several-cycle mid-IR

light. The OPA output at the idler wavelength of 2.1 µm is set to an energy of 2.75 mJ and a duration of $\sim$ 26 fs (four cycles). The signal at 1.5 µm wavelength is produced with an energy of 4.5 mJ and a duration of $\sim$ 24 fs (five cycles). These driving pulses are then coupled into hollow dielectric waveguides (Appendix A) with inner diameters ranging from 150 and 400 µm and lengths between 1 and 5 cm. $\sim 10 - 20$ atm of helium gas is supplied to the waveguide for phase-matched HHG at these mid-IR wavelengths. The signal driver results in a HHG supercontinuum spanning photon energies up to 360 eV, while the idler produces a supercontinuum up to 550 eV. A photon flux of $> 10^9$ photons/s/1% bandwidth was measured in the water window region: three orders of magnitude larger than previously demonstrated [149, 121].

Following the HHG medium, our experimental beamline consists of an X-ray spectrometer (Hettrick) with a resolution in the EUV and soft X-ray regions of $\lambda/\Delta\lambda > 1000$. The XAFS samples and metal filters are placed between the spectrometer grating and the X-ray CCD camera (Andor). Metal filters are used to reject the fundamental driver from the HHG supercontinuum, while also allowing calibration of the spectrometer using characteristic absorption edges of foil filters. Differential measurements with and without the XAFS samples allow the determination of the spectrally-resolved absorptivity with high accuracy. The data is then analyzed with Athena and Artemis software [107].

The HHG spectrum resulting from the 1.5 µm driver is plotted in pink in Fig. 3.3. This broadband source was used to illuminate two polymers, mylar and parylene, which contain similar carbon structures but different neighboring elements. Figure 3.4 shows the experimental results, demonstrating the ability of HHG spectroscopy to differentiate between chemical compounds using NEXAFS, despite the degree of chemical similarity and the common probe of the carbon K-edge. Our measurements have a spectral resolution 0.2 eV, which is sufficient to identify a 0.2 eV difference in the $\sim$ 285 eV absorption peak between the mylar and parylene samples. In both samples, this peak near 285 eV corresponds to electron transitions from the 1s core shell of carbon to the molecular antibonding π^* orbital for unsaturated C=C bonds (sp^2 hybridization). The energy shift between the two samples is clear for this absorption peak. There is an additional peak near $\sim$ 289 eV

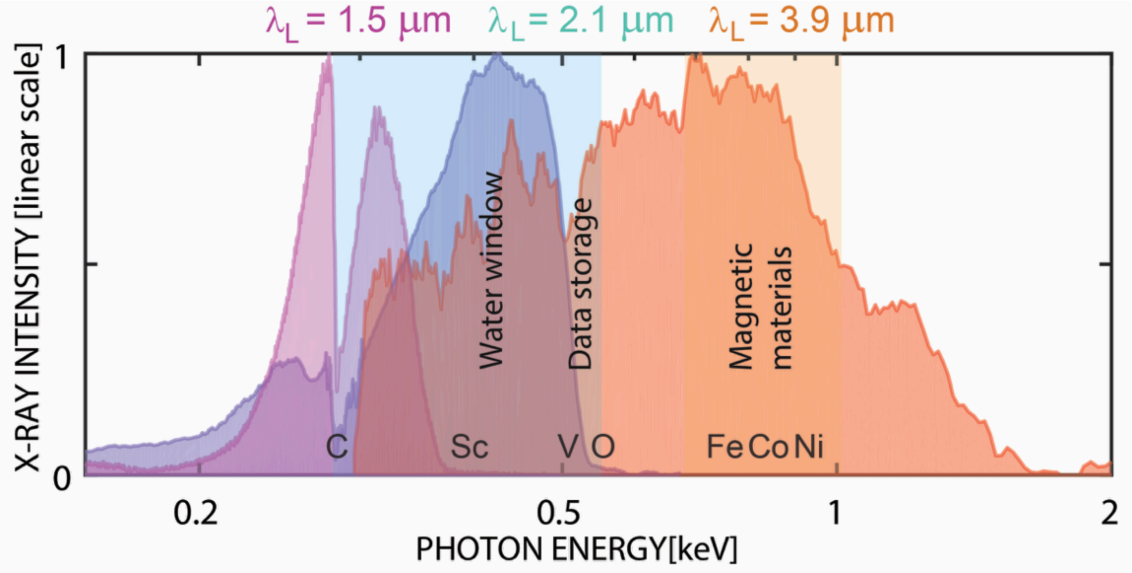

Figure 3.3: Broadband soft X-ray supercontinua generated using phase-matched HHG. Photon energies up to 0.36 keV, 0.55 keV, and 1.6 keV are generated in He gas using mid-IR driving lasers at 1.5 µm (OPA signal), 2.1 µm (OPA idler), and 3.9 µm (OPCPA idler), respectively. Adapted from [135].

corresponding to electron transitions from two contributions: the 1s core shell to the antibonding σ^* molecular orbital, as well as the 1s core shell to the Rydberg-like 3p orbitals of the aromatic ring (benzene) [76]. One consideration for this measurement is the relative angle between the HHG polarization ($\vec{\varepsilon}$) and the molecular orientation (final orbital direction $\vec{\lambda}_f$), an angle $\vartheta_{\vec{\varepsilon},\vec{\lambda}_f}$ that introduces an absorption probability factor of $\cos^2(\vartheta_{\vec{\varepsilon},\vec{\lambda}_f})$. The polarization $\vec{\varepsilon}$ in our experiment lies within the plane of the samples.

3.3 XAFS in Scandium

Using the 2.1 µm OPA idler to drive HHG results in the purple HHG spectrum in Fig. 3.3, which covers a significant range of photon energies beyond the scandium L-edge. Figure 3.5 shows the experimentally extracted XAFS function at the L-absorption edge of a monoatomic hexagonal-close-packed (hcp) Sc thin foil at the 398 eV L-absorption edge at room temperature, both in k-space and in real space. By taking a Fourier transform of the XAFS function in k-space (Fig. 3.5B), the interatomic spatial distributions can be obtained (Fig. 3.5C). Using the Athena and Artemis software [107], the spatial distribution data was fit to Eq. (3.1) to yield first- and second-shell distances of 3.25 ± 0.05 Å(six-fold degenerate) and 3.30 ± 0.05 Å(six-fold degenerate), respectively. Our spectral measurements agree very well with the CXRO database [63], and the extracted shell distances agree well with the expected interatomic lengths for a Sc hcp bulk lattice. Thus, our thin film samples ($\sim$ 150 nm) are confirmed to have lattice constants similar to bulk values.

3.4 EXAFS in Iron

To investigate the extended-edge XAFS signal (EXAFS) of a material, significant source spectrum is required beyond an absorption edge. Investigating a magnetically relevant material such as iron would then require HHG signal well beyond its L-edges near 0.7 keV. To achieve such a broadband spectrum, an OPCPA with an idler wavelength of 3.9 µm was used [139]. The OPCPA operated at a repetition rate of 20 Hz with 80 fs pulse duration, ultimately producing an HHG

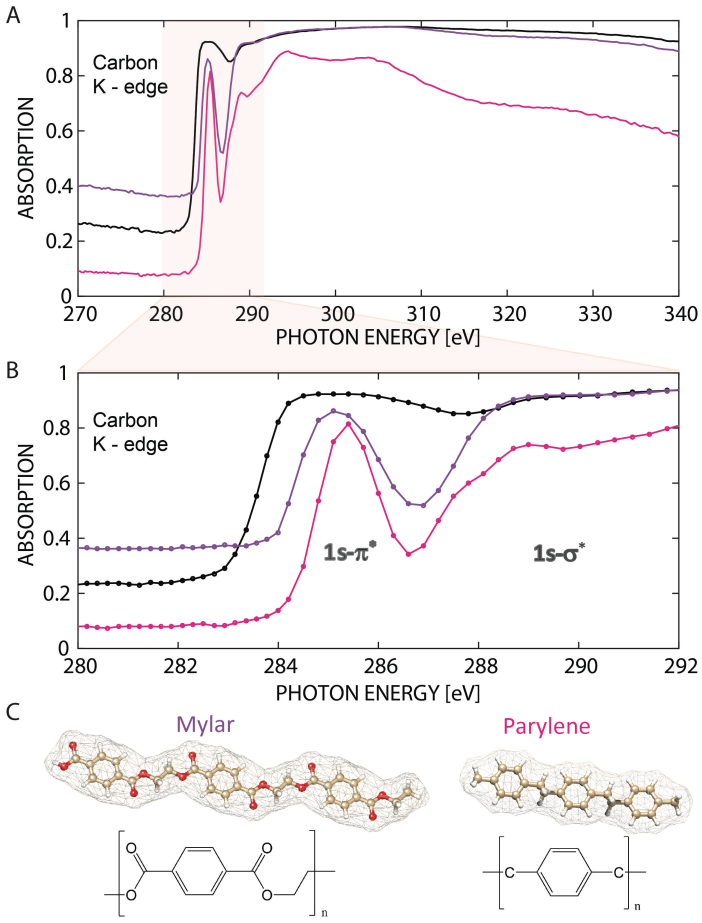

Figure 3.4: Experimental NEXAFS spectroscopy near the carbon K-edge using a 1.5 µm-driven HHG supercontinuum up to 360 eV. A) NEXAFS of C-containing polymers (mylar (violet) and parylene (pink)), at the carbon K-edge. Also plotted is the experimental absorption spectrum of a carbon thin film (black) for reference. B) Close-up view showing peaks due to transitions from 1s to both π^* and σ^* orbitals. C) Molecular structure of mylar and parylene rendered for trimers (C atoms in brown, O in red, H in white). Adapted from [135].

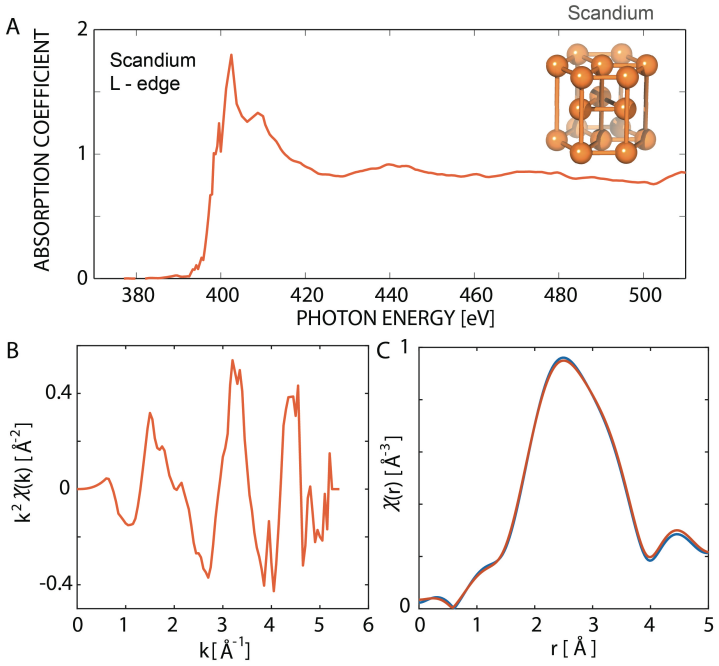

Figure 3.5: Experimental XAFS spectroscopy near the Sc L-edge, using a 2 µm-driven HHG supercontinuum up to 550 eV. (A) The normalized absorption coefficient of Sc near the L-absorption edge at 398 eV. (B) k^2-scaled EXAFS function in k-space extending to $> 5\text{Å}^{-1}$. (C) Experimental R-space XAFS function (blue), not corrected for δ phase shifts, and fitted (red) to Eq. 3.1. The real space XAFS function exhibits a broad peak. Inset shows a Sc hcp unit cell. Adapted from [135].

supercontinuum spanning the EUV and into the soft X-ray spectral region up to 1.6 keV ($\sim$ 7.7 Å) with $\sim 2 \times 10^6$ photons/s/1% bandwidth at $\sim$ 1 keV (orange spectrum in Fig. 3.3).

Figure 3.6 shows the k-space and real space XAFS function obtained at the L-absorption edges of a room-temperature monoatomic body-centered-cubic (bcc) Fe thin foil. The fitting procedure yields first- and second-shell distances of 2.48 ± 0.03 Å(eight-fold degenerate) and 2.87 ± 0.03 Å(six-fold degenerate), respectively. The latter distance is the lattice constant for a bulk bcc Fe unit cell. Figure 3.7 shows X-ray diffraction measurements on the same sample, independently confirming the bcc crystal structure with a lattice constant of 286.68 ± 0.03 pm.

It can be challenging to distinguish features from multiple rescattering paths, so we also decompose the XAFS function terms using a continuous Cauchy wavelet transform (CCWT) (Figure 3.6A [89]). This 2D plot can help discriminate shell distances by providing information regarding the k and R ranges that each nearest neighbor shell can contribute to (Figure 3.6C).

3.5 XAFS Summary

Through the use of state-of-the-art OPA and OPCPA laser technologies, broadband HHG spectra were obtained with unprecedented photon energies and fluence. Utilizing these broad HHG sources for XAFS spectroscopies yielded chemically- and structurally-sensitive data that agree with theory and independent measurements. This work represents a new benchmark for broadband, static spectroscopic applications, and can easily be extended to dynamic spectroscopies through the inherently ultrafast nature of the HHG source (currently under investigation). Coherent, ultrafast light sources with broader spectral bandwidths than achieved here are limited, and HHG beyond the soft X-ray regime is yet to be observed. The theoretical limits of long wavelength-driven HHG will be investigated in Chapter 4, revealing the feasibility of generating higher cutoff harmonics that could be used for further spectroscopic applications.

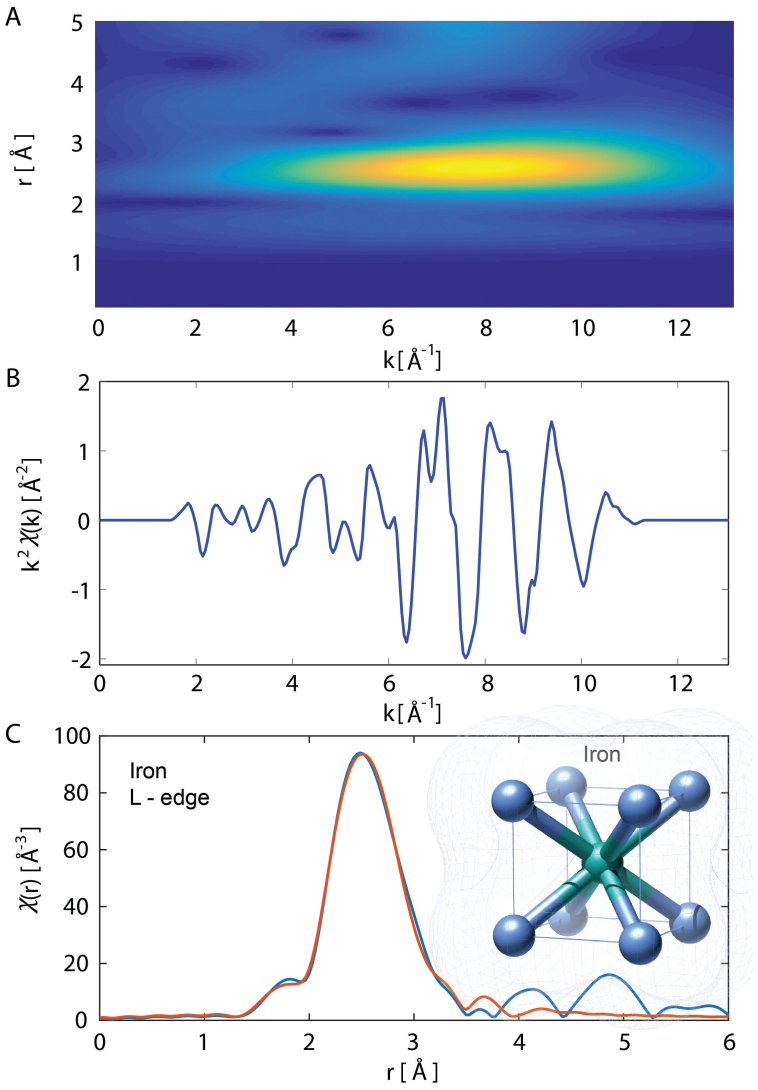

Figure 3.6: Experimental EXAFS spectroscopy of a Fe thin film using a 3.9 µm driving laser (orange soft X-ray spectrum from Fig. 3.3). (A) CCWT analysis (modulus) near the Fe L-edge (0.7 keV); (B) k^2-scaled EXAFS function in k-space extending to 12 Å^{-1}. (C) Experimental real-space EXAFS function (blue), uncorrected for δ phase shifts, with the first peak fitted to the theoretical Eq. (3.1) (red). Inset shows a Fe bcc unit cell. Adapted from [135].

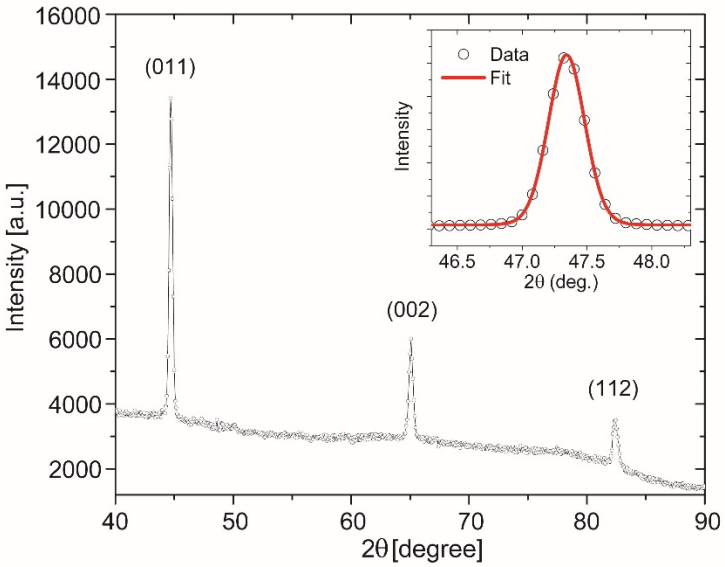

Figure 3.7: X-ray diffraction data showing the first few diffraction peaks for the Fe thin film sample. The data indicates a body-centered-cubic (bcc) structure with a lattice constant of 286.68 ± 0.03 pm. Adapted from [135].

Chapter 4

The Lorentz Force during HHG

[1] To date, HHG has been demonstrated with energies up to a record level of 1.6 keV using 3.9 µm drivers [161]. This achievement was possible according to the phase-matching cutoff scaling law: $E_{PMC} \propto \lambda_L^{(1.6-1.7)}$. To extend the HHG photon energy further, increasing the driving laser wavelength is an obvious route (although more complex geometries described in Chapter 5 and HHG from ions using ultraviolet drivers [134] are alternative approaches). One consideration that might limit HHG driven by long wavelengths is the unfavorable flux scaling of $\lambda_L^{-(5-9)}$ [161, 120, 42, 98]. Fortunately, many more emitters can be present in very high pressure gases that satisfy long wavelength phase-matching conditions, which can compensate for the low single-atom HHG yield. However, acquiring a driving laser that has both ultrafast pulse duration (a requirement for phase-matched HHG) and central wavelength beyond 4 µm proves to be a challenge. To our knowledge, there are currently no commercially available broadband gain media that would enable ultrafast oscillators and amplifiers at mid-infrared wavelengths beyond 4 µm. OPA and OPCPA technologies are possible solutions using appropriate frequency conversion media in multi-stage configurations [111], or possibly a single stage pumped using a relatively new ultrafast laser technology operating near 2.5 µm, Cr:ZnS and Cr:ZnSe [166]. Spectral broadening through self-phase modulation using 10 µm CO_2 lasers provides another possibility, but this approach can require further compression or might result in a multi-pulse structure [104, 101, 100].

Despite the present difficulty in performing HHG experiments with suitable long wavelength

[1] The work presented in this section is published in [43] and has been submitted for publication [102].

drivers, a theoretical investigation of the fundamental physics can be performed. Section 1.2 covers the zero-order physics of HHG, providing an explanation of the mechanism and predictions that are consistent with observed phenomena to date. However, several assumptions have been made during the derivations that hold true only for short wavelengths, non-relativistic intensities, and plane-wave driving fields. Testing the validity of these assumptions for the case of long wavelength drivers and realistic laser modes is an important step toward understanding the spectral limitations of HHG technology. A primary effect that might limit HHG at long wavelengths is the trajectory of the ionized electron and how it might be influenced by the full Lorentz force.

4.1 The Full Lorentz Force

As previously described by Eq. (1.16), the full Lorentz force that the electron experiences once ionized is:

$$\boldsymbol{F}(t) = \frac{d\boldsymbol{p}(t)}{dt} = q_e \left[\boldsymbol{E}_L(t) + \boldsymbol{v}(t) \times \boldsymbol{B}_L(t)\right] \tag{4.1}$$

By neglecting the magnetic component of the Lorentz force (assuming non-relativistic motion), one arrives at Eqs. (1.17–1.19). These equations of motion are true to zero-order, and can be used as a basis to which relativistic (and non-plane-wave) perturbations can be applied. The zero-order equations of motion are reproduced here (assuming the ionized electron is initially stationary at the origin):

$$\boldsymbol{a}_0(t) = \frac{q_e}{m_e} E_{L0} \cos(\omega_L t + \phi_0)\hat{\boldsymbol{y}} \tag{4.2}$$

$$\boldsymbol{v}_0(t) = \frac{q_e}{m_e \omega_L} E_{L0} [\sin(\omega_L t + \phi_0) - \sin(\phi_0)]\hat{\boldsymbol{y}} \tag{4.3}$$

$$\boldsymbol{x}_0(t) = -\frac{q_e}{m_e \omega_L^2} E_{L0} [\cos(\omega_L t + \phi_0) + \omega_L \sin(\phi_0) t - \cos(\phi_0)]\hat{\boldsymbol{y}} \tag{4.4}$$

The equations of motion can then be rewritten in terms of the zero-order solutions and first order perturbations:

$$\begin{aligned} \boldsymbol{a}(t) &= \boldsymbol{a}_0(t) + \boldsymbol{a}_1(t) \\ &= \boldsymbol{a}_0(t) + \frac{q_e}{m_e}\left[\boldsymbol{E}_{L1}(t) - E_{L0}\,\cos(\omega_L t + \phi_0)\frac{\boldsymbol{v}_0(t)}{c} \times \hat{\boldsymbol{x}}\right] \end{aligned} \tag{4.5}$$

$$\begin{aligned} \boldsymbol{v}(t) &= \boldsymbol{v}_0(t) + \boldsymbol{v}_1(t) = \boldsymbol{v}_0(t) + \int_0^t \boldsymbol{a}_1(t')dt' \\ &= \boldsymbol{v}_0(t) + \frac{q_e}{m_e}\left[\int_0^t \boldsymbol{E}_{L1}(t')dt' + \frac{q_e E_{L0}^2}{2m_e\omega_L^2 c}\left[\sin(\omega_L t + \phi_0) - \sin(\phi_0)\right]^2 \hat{\boldsymbol{z}}\right] \end{aligned} \tag{4.6}$$

$$\begin{aligned} \boldsymbol{x}(t) &= \boldsymbol{x}_0(t) + \boldsymbol{x}_1(t) = \boldsymbol{x}_0(t) + \int_0^t \boldsymbol{v}_1(t')dt' \\ &= \boldsymbol{x}_0(t) + \frac{q_e}{m_e}\left[\int_0^t \left(\int_0^{t''} \boldsymbol{E}_{L1}(t')dt'\right)dt'' + \frac{q_e E_{L0}^2}{8m_e\omega_L^3 c}\Upsilon(t,\phi_0)\hat{\boldsymbol{z}}\right] \end{aligned} \tag{4.7}$$

where:

$$\begin{aligned} \Upsilon(t,\phi_0) = 4\omega_L t + 4\sin(\omega_L t + 2\phi_0) - 2\omega_L t\cos(2\phi_0) - \\ - 4\sin(\omega_L t) - 3\sin(2\phi_0) - \sin(2\omega_L t + 2\phi_0) \end{aligned} \tag{4.8}$$

Here, we have included a perturbation to the electric field $\boldsymbol{E}_{L1}(t)$, which will be necessary when considering non-plane-wave driving fields.

Equations (4.5–4.8) clearly contain two perturbing contributions. The first is from the first-order electric field $\boldsymbol{E}_{L1}(t)$, and the second is from the magnetic Lorentz force arising from $\boldsymbol{v}_0(t) \times \boldsymbol{B}_L(t)$. Already, the perturbative effect of the magnetic Lorentz force can be calculated to yield a $\boldsymbol{v} \times \boldsymbol{B}$ drift at the time the electron would typically recollide with its parent ion, which we define as:

$$\delta_{\boldsymbol{v}\times\boldsymbol{B}} = \frac{q_e^2 E_{L0}^2}{8m_e^2\omega_L^3 c}\Upsilon(\tau_f,\phi_0)\hat{\boldsymbol{z}} \tag{4.9}$$

where the displacement is evaluated at the return time $t = \tau_f$. From Eq. (4.9), it is clear that the magnetic Lorentz force causes the electron to drift along the z-direction, and its magnitude scales as $\delta_{\boldsymbol{v}\times\boldsymbol{B}} \propto I_L\lambda_L^3$ for a constant value of ϕ_0. For all returning trajectories $\phi_0 \in [0, \pi/2)$, $\Upsilon(\tau_f, \phi_0)$ is

positive, meaning the magnetic Lorentz drift is always in the positive z-direction. This is true for electrons ionized during an up-cycle of the electric field or a down-cycle.

Previous work has considered the effect of the magnetic Lorentz force during strong field ionization and recollision processes [72, 167, 49, 87, 57, 21], including a work by Walker *et al.* in which recollision was suggested to be greatly reduced for driving lasers with $\lambda_L \geq 6$ µm [92]. However, the laser intensities used in these calculations were much larger than are relevant for HHG, and a plane-wave driving field was used (i.e. the field's transverse extent is infinite and $\boldsymbol{E}_1(t) = 0$). In the following sections, the full Lorentz drift during HHG-relevant conditions will be considered.

4.2 Field Components for Finite Laser Modes

By removing the assumption of a plane-wave driver, additional field components arise that can influence the trajectory of the ionized electron. This is a consequence of satisfying Maxwell's equations in free-space using finite transverse spatial modes. In particular, a longitudinal electric field component necessarily arises in linearly-polarized beams:

$$E_z(t) = \frac{i}{k}\frac{\partial E_\psi(t)}{\partial \psi}, \tag{4.10}$$

where ψ represents the polarization direction (for all derivations here, $\psi = y$). This holds true for the first-order field equations for waveguide modes expressed in Eq. (A.2) in Appendix A, and is also true for Gaussian modes, as described in [23]. For both a Gaussian mode and the EH_{11} waveguide mode, the longitudinal electric field $E_z(t)$ qualitatively takes on a two-lobed amplitude profile with opposing signs for each half, and has a $\pi/2$ phase shift with respect to $E_y(t)$ and $B_x(t)$. Importantly, $E_z(t) = 0$ for all locations with $y = 0$, which includes the center of the mode. Figure 4.1 depicts the amplitude profiles for these geometries.

Equation (4.10) indicates that the temporal dependence of $E_z(t)$ is the same as that of $E_y(t)$, except for a $\pi/2$ phase shift. The amplitude of $E_z(t)$ is proportional to $E_{L0}\lambda_L/w$ for a Gaussian mode, or $E_{L0}\lambda_L/a$ for the EH_{11} waveguide mode. Thus, it is straightforward to show that the

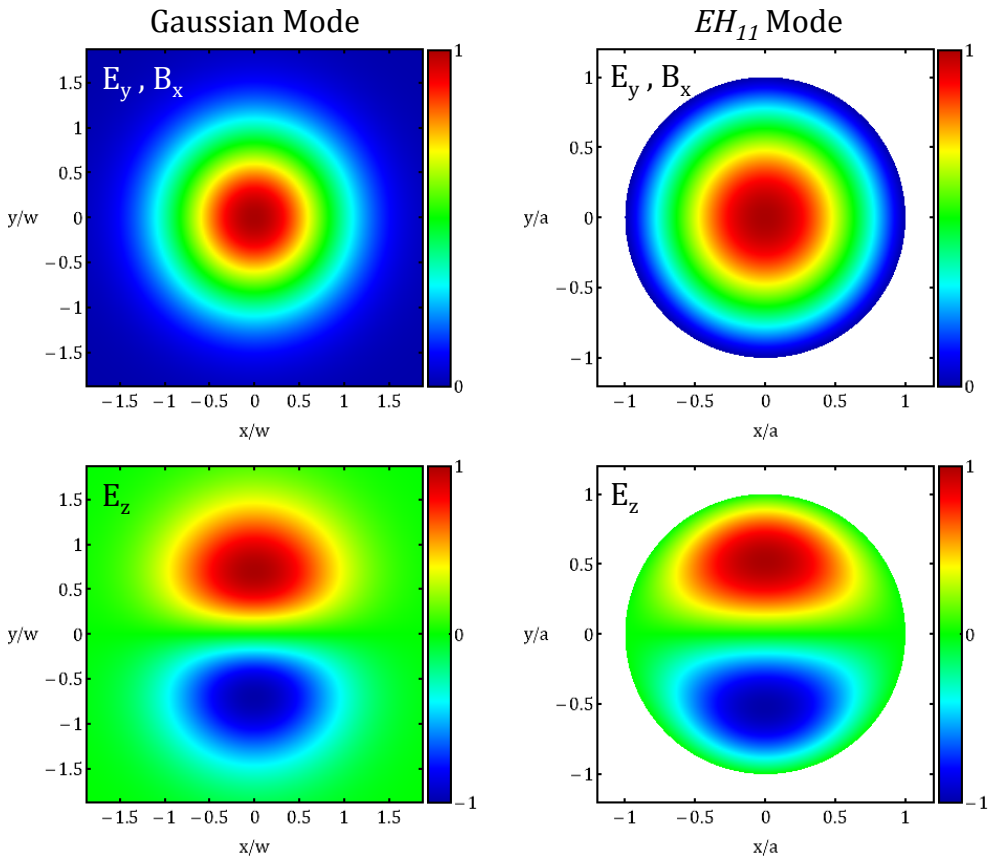

Figure 4.1: Transverse (top) and longitudinal (bottom) field components for Gaussian (left) and EH_{11} (right) modes. The axis ranges for the two geometries are chosen to give comparable mode sizes. Scale bars are normalized.

perturbation to $\boldsymbol{x}(t)$ resulting from $E_z(t)$ is:

$$\begin{aligned}\delta_{E_z} &= \frac{q_e}{m_e}\int_0^t \left(\int_0^{t''} E_z(t')dt'\right)dt'' \\ &= \frac{-q_e E_z(x,y)}{m_e\omega_L^2}\left[\omega_L t\cos(\phi_0) - \sin(\omega_L t+\phi_0) + \sin(\phi_0)\right]\end{aligned} \tag{4.11}$$

where $E_z(x,y)$ represents the spatially varying amplitude of $E_z(t)$ and contains the $E_{L0}\lambda_L/w$ proportionality. Ultimately, the displacement from the E_z component of the driving field scales as $\delta_{E_z} \propto I_L^{1/2}\lambda_L^3 w^{-1}$.

For both longitudinal drifts, the scaling with τ_f, or more fundamentally ϕ_0, cannot be described in a simple form; however, the magnitudes of these drifts generally decrease as ϕ_0 increases from 0 to $\pi/2$. The total longitudinal drift resulting from the Lorentz force will be the sum $\delta_L = \delta_{\boldsymbol{v}\times\boldsymbol{B}} + \delta_{E_z}$, and the interplay between the two drift components can result in large or small total Lorentz drift depending on the relative signs of the two drifts, which varies spatially as discussed in Section 4.5.

4.3 Recombination Probability with Lorentz Drift

If the electron is treated classically, one would expect there to be greatly reduced probability for the electron to recombine with its parent ion if there is a longitudinal drift larger than a Bohr radius or so. However, due to the quantum nature of the electron, the electron wavepacket diffuses transversely as it travels in the continuum, as described in Section 1.3.2. Thus, for any finite spatial overlap between the diffused wavepacket ψ_d and the wavefunction of a bound electron ψ_b, the probability P_R of recombination and emission of a photon is nonzero and modeled by:

$$P_R = \int_{\mathbb{R}} d^3\boldsymbol{r}\,\psi_d^*(\boldsymbol{r}, t=\tau_f)\psi_b(\boldsymbol{r}) \tag{4.12}$$

One may also describe the harmonic yield as originating from a time-varying dipole moment, arising from the interference of $\psi_d(\boldsymbol{r},t)$ with $\psi_b(\boldsymbol{r},t)$. In either case, the photon yield will be proportional to P_R as well as the ionization rate at the time the electron was ionized $\omega_{ADK}(\boldsymbol{r}_0, t=0)$ [68, 72, 30].

When $\psi_d(\boldsymbol{r},t)$ is evaluated for even the shortest wavelength considered here (0.8 µm), it becomes evident that the integral describing R_P can be reduced. The diffused wavepacket $\psi_d(\boldsymbol{r},\tau_f)$

returns with a width that is orders of magnitude larger than the width of $\psi_b(\boldsymbol{r})$. For the purposes of integration, $\psi_b(\boldsymbol{r})$ can be approximated as a delta function. Instead of applying the Lorentz drift δ_L to ψ_d it is straightforward to apply it to ψ_b, representing it as a shifted delta function: $\psi_b(\boldsymbol{r}) = \delta(\boldsymbol{r} - \delta_L \hat{\boldsymbol{z}})$. Considering only the wavefunction amplitude, the form of P_R can be rewritten: $P_R = |\psi_d(\delta_L, \tau_f)|$. Note that the drift-induced quantum phase dynamics of the electron can shift the absolute positions of the harmonic peaks in the spectral domain [102], but should not change the overall single-atom spectral shape. Only amplitude effects will be considered here.

To determine how the Lorentz drift influences the high harmonic flux, a comparison must be made between the case when the Lorentz drift is included, and the case when it is assumed to be zero. The relevant comparison is the ratio of recombination probabilities for the two cases, expressed as a recombination probability ratio (RPR) defined as:

$$RPR = P_R(\delta_L)/P_R(0) = \frac{|\psi_d(\delta_L, \tau_f)|}{|\psi_d(0, \tau_f)|} \tag{4.13}$$

The RPR is defined for a single electron ionized during a particular half-cycle of the driving laser, and has a maximum value of unity corresponding to zero displacement. In the following section, we quantify how this recombination probability ratio scales with wavelength, indicating a drift-induced reduction in HHG fluence as the wavelength is increased.

4.4 RPR Scaling with Wavelength

In order to study Lorentz displacement effects under conditions applicable to HHG, the intensity of the driving laser must be chosen to achieve bright, phase-matched HHG flux. Constraining the intensity to the wavelength also simplifies the investigation by reducing the parameter space. We assume the target gas is helium and the peak intensity of the driver is optimized for maximal, mode-averaged, phase-matched HHG flux driven by an 8-cycle pulse, as depicted in Figure 1.20. With this assumption, and using reasonable values for the laser mode size ($w \sim 50$ µm), it becomes evident that the Lorentz displacement produces a non-negligible effect for wavelengths larger than ~ 6 µm. Table 4.1 summarizes the relevant wavelength-dependent parameters and the resulting

Table 4.1: Lorentz displacement results for selected laser wavelengths. The driving laser mode is assumed to be 100 µm in diameter, and the ionization phase $\phi_0 = 18°$. Maximum values within the spatial mode are presented for $|\delta_{\boldsymbol{v}\times\boldsymbol{B}}|$ and $|\delta_{E_z}|$, whereas $|\delta_L|_{\text{symm}}$ represents the total Lorentz displacement at the spatial location along the polarization axis where $|\delta_{\boldsymbol{v}\times\boldsymbol{B}}| = |\delta_{E_z}|$. The reported RPR_{symm} values are for the same location.

λ_L (µm)	I_L ($\times 10^{14}$ W/cm^2)	$\lvert\delta_{\boldsymbol{v}\times\boldsymbol{B}}\rvert$ (Å)	$\lvert\delta_{E_z}\rvert$ (Å)	$\lvert\delta_L\rvert_{\text{symm}}$ (Å)	$\sigma(\tau_f)$ (Å)	RPR_{symm}
0.8	7.58	0.372	0.293	0.455	19.1	0.9997
3.0	4.20	10.9	11.5	15.0	71.1	0.9779
6.0	3.26	67.7	81.1	103	142	0.7671
8.0	2.97	146	183	223	189	0.5000
10.0	2.77	266	346	406	237	0.2298
15.0	2.45	794	1,100	1,213	355	0.0029
20.0	2.25	1,731	2,507	2,648	474	10^{-7}

displacements and RPR values. The net Lorentz drift magnitude $|\delta_L|$ varies across the transverse spatial dimensions, but a symmetric net drift $|\delta_L|_{\text{symm}}$ can be defined at the location where $\delta_{\boldsymbol{v}\times\boldsymbol{B}}$ is the same magnitude as δ_{E_z}. This symmetric net drift is listed in Table 4.1, and provides a metric to estimate when the field-driven electrons will be displaced far enough to miss the ion during one half-cycle, while trajectories during the next half-cycle (when $\delta_{\boldsymbol{v}\times\boldsymbol{B}}$ and δ_{E_z} have opposite sign) directly recollide with the ion. It is important to note that δ_{E_z} has a magnitude $\geq \delta_{\boldsymbol{v}\times\boldsymbol{B}}$ when using the harmonic cutoff ionization phase $\phi_0 = 18°$. Even when considering the Lorentz force in ultra-strong field experiments, the driving laser typically must be tightly focused to achieve relativistic intensities ($I_L > 10^{18}$ W/cm^2), in which case the contribution from E_z is large and cannot be ignored. Figure 4.2 serves as a visual aid for the field and drift components in a Gaussian focus geometry.

Although we have previously derived a λ_L^3 scaling for each of the longitudinal drift components, the optimal intensity for HHG flux scales close to $\lambda_L^{-0.4}$. Thus, the final scaling of the total Lorentz drift will be close to $\lambda_L^{2.6}$. Figure 4.3 shows the magnitude of the net Lorentz drift $|\delta_L|_{\text{symm}}$ plotted as a function of wavelength, where its measured slope of 2.62 verifies the wavelength scaling. The width of ψ_d upon return to the parent ion $\sigma(\tau_f)$ scales linearly with wavelength, and is also plotted in Fig. 4.3. The inset of Fig. 4.3 shows the effect of $|\delta_L|_{\text{symm}}$ on the RPR for adjacent

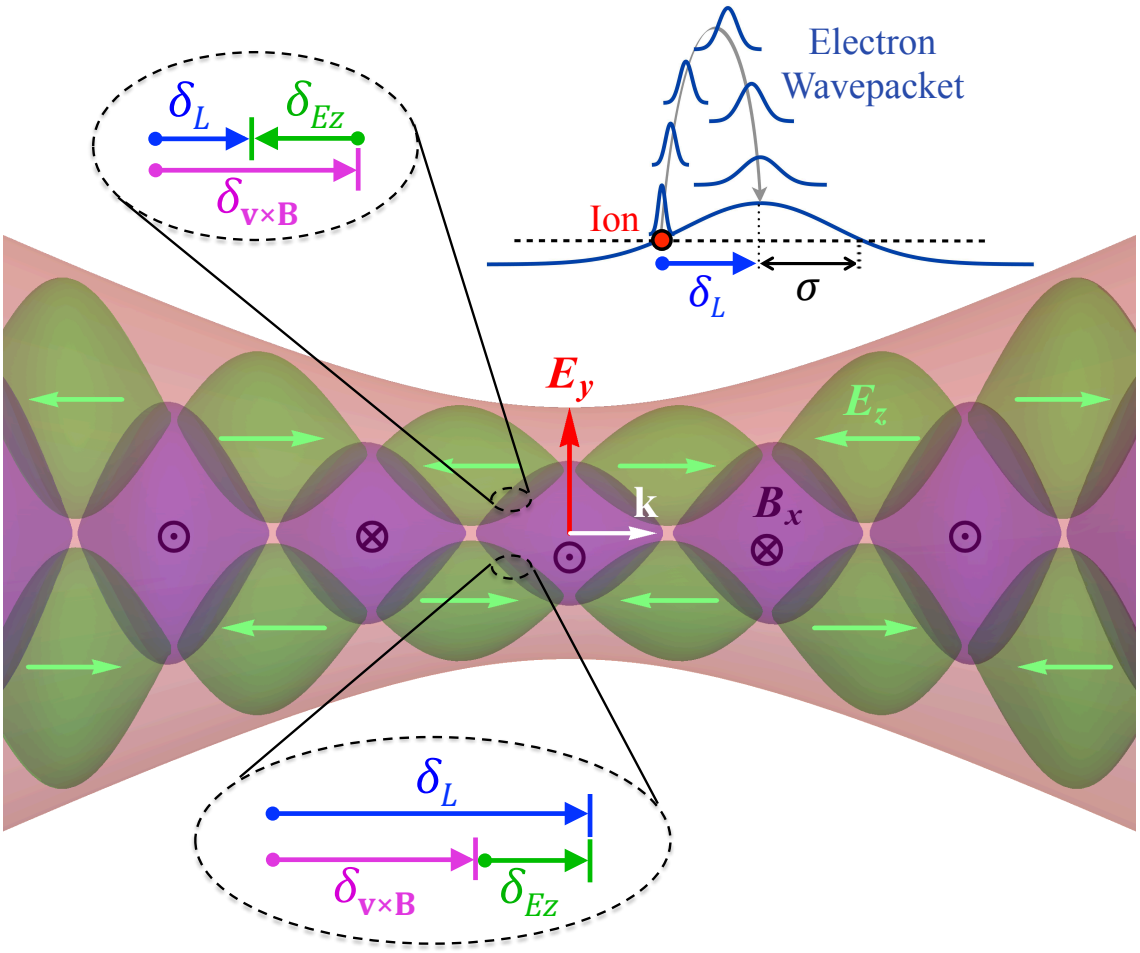

Figure 4.2: Field components of a Gaussian free focus (in the waveguide case, the fields are similar but the guided beam does not diverge). The Gaussian mode envelope is depicted in red, the transverse fields E_y and B_x oscillate like the purple regions, and the longitudinal field E_z is depicted by the green regions. The longitudinal displacements due to the $\boldsymbol{v} \times \boldsymbol{B}$ force ($\delta_{\boldsymbol{v}\times\boldsymbol{B}}$), the longitudinal electric field (δ_{E_z}), and the total Lorentz force (δ_L) are shown in two locations in the focus, where the net displacement changes in magnitude. Top-right: Visualization of the electron wavepacket drift. Quantum diffusion of the electron wavepacket enables recollision in spite of significant Lorentz drift.

half-cycles. For one of the half-cycles $\delta_{\boldsymbol{v}\times\boldsymbol{B}}$ cancels δ_{E_z}, whereas they add in the next half-cycle. Thus, the RPR alternates between unity and RPR_{symm}.

The Lorentz displacement $|\delta_L|_{\text{symm}}$ increases at a rate $\lambda_L^{1.62}$ faster than the diffused wavepacket width. Accounting for the Gaussian form of ψ_d, the resulting scaling of RPR_{symm} (and the total HHG flux attenuation from the Lorentz drift) is given by:

$$RPR_{\text{symm}} \sim exp\left[-\left(\frac{\delta_L}{\sigma}\right)^2\right] \sim exp\left[-\left(\left\{\frac{\delta_L}{\sigma}\right\}^{1.62}\right)^2\right] \sim exp\left[-\left(\frac{\lambda_L[\mu\text{m}]}{8.7}\right)^{3.24}\right] \tag{4.14}$$

The fitting parameter D was calculated to nicely fit the RPR_{symm} trend using the data in Table 4.1. Fitting to the mode- and ϕ_0- integrated RPR_{symm} for harmonics $> 2U_p$ causes the D parameter to increase to ~ 13.3, with some underestimation at longer wavelengths. The super-Gaussian form of Eq. (4.14) encapsulates the initially slow onset of the Lorentz displacement, followed by a steep reduction of RPR_{symm} for $\lambda_L > 6$ µm. Note that this flux scaling only accounts for the Lorentz displacement and will act in addition to the $\lambda_L^{-(5-6)}$ scaling from quantum diffusion. Additionally, it is only true for half-cycles where the two drift components have the same sign. Interestingly, the flux attenuation due to quantum diffusion is dominant even up to 20 µm drivers, indicating that the Lorentz drift is not the limiting factor with respect to high harmonic flux driven by long wavelengths.

4.5 Lorentz Drift Spatial Profiles

In addition to attenuating the total high harmonic flux, the Lorentz displacement also has a spatial dependence that influences the HHG mode. Figure 4.4 shows the Lorentz displacements and RPR profile using a Gaussian focus geometry for a single half-cycle of a 10 µm driving laser, assuming the electron is ionized at the harmonic cutoff phase $\phi_0 = 18°$. The energy of an emitted harmonic will be 3.17 times the local ponderomotive potential ($U_{p,\text{loc}}$), which depends on the local intensity. This local energy can be rewritten in terms of the maximum harmonic energy $3.17U_p$, occurring at the center of the mode where the intensity is the highest (I_L). In Fig. 4.4(d), rings are plotted where the local cutoff energies correspond to 1 and 2 times the maximum U_p. Note that

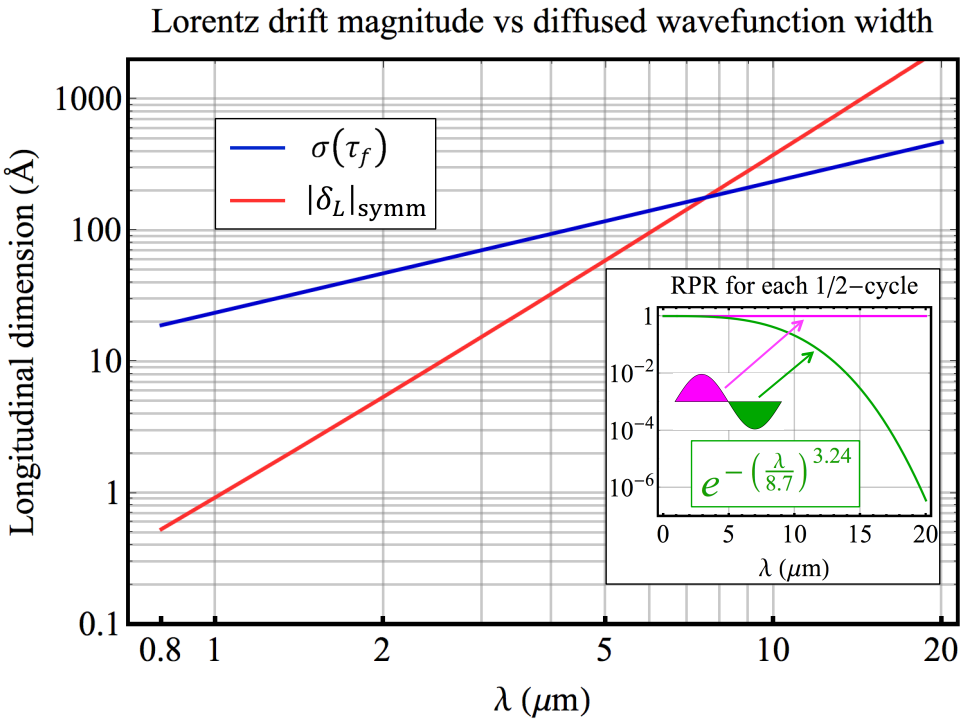

Figure 4.3: Total Lorentz drift magnitude (red) and diffused electron wavepacket width (blue) as a function of driving laser wavelength. The electron is assumed to be ionized at 18°, and the laser intensities used are those that maximize phase-matched HHG flux in Helium. $|\delta_L|_{\text{symm}}$ is calculated at the spatial location along the polarization axis where $|\delta_{\boldsymbol{v}\times\boldsymbol{B}}| = |\delta_{E_z}|$. The lines intersect at $\lambda_L = 7.4$ µm and 175 Å, after which the Lorentz drift exceeds the wavepacket width. The inset shows the RPR for adjacent half-cycles where $|\delta_L|_{\text{symm}}$ is calculated, indicating a harmonic efficiency that is modulated in the time domain with λ_L-periodicity.

the plots would be reflected about the x-axis for the next half-cycle, due to the sign flip of δ_{E_z} but not $\delta_{\boldsymbol{v}\times\boldsymbol{B}}$.

Figure 4.5 shows the same plots as Fig. 4.4, but for a waveguide geometry with an inside diameter (I.D. = $2a$) resulting in an equivalent mode size ($w = 0.6435a$, Fig. A.2). Note that the separate components of the Lorentz drift δ_{E_z} and $\delta_{\boldsymbol{v}\times\boldsymbol{B}}$ add in one half of the mode, while they cancel in the other half. While this is, from a flux perspective, detrimental for one half of the mode, the other half can benefit from the drift cancellation. If the flux for only the highest harmonics ($> 2U_p$) is to be optimized, the drift cancellation should occur as close to the center of the mode as possible. By definition, the E_z field is zero at the center, so its resulting drift cannot cancel the $\boldsymbol{v} \times \boldsymbol{B}$ drift, which is maximal at the center. To shift the location of drift cancellation closer to the center, one can simply inspect the drift scaling laws ($\delta_{\boldsymbol{v}\times\boldsymbol{B}} \propto I_L\lambda_L^3$ and $\delta_{E_z} \propto I_L^{1/2}\lambda_L^3 w^{-1}$) to conclude that the driving laser mode size should be reduced. By changing the relative magnitude of δ_{E_z} with respect to $\delta_{\boldsymbol{v}\times\boldsymbol{B}}$, one can control the spatial position of drift cancellation. In fact, by specifying a driving wavelength and constraining the intensity to be optimal for HHG, the only free parameter to control the RPR mode profile is the mode size.

In Fig. 4.6, the HHG photon energy at the location of drift cancellation is plotted as a function of wavelength and mode size. Generally, the RPR approaches unity at a higher harmonic energy in waveguides than in a Gaussian focus, for comparable mode sizes. For a 20 µm driver with optimal intensity of 2.77×10^{14} W/cm^2 in a 250 µm I.D. waveguide, the HHG energy that has $RPR = 1$ is approximately $2U_p$ which is ≈ 17 keV. This shows that even very high energy harmonics in the hard X-ray region can be produced through HHG without the Lorentz drift shutting off the recollision process. Furthermore, Fig. 4.6 can be used as a guide to select the mode size necessary for drift cancellation and efficient generation of a desired HHG photon energy.

Although the single-phase harmonic cutoff results in Figs. 4.4–4.6 are informative, the total HHG mode emitted from a single half-cycle would result from electrons ionized at all phases within $[0, \pi/2)$. Ionization phases closer to the peak of the field ($\phi_0 \sim 0$) have the highest ionization rate (ω_{ADK}), but these electrons spend more time (τ_f) free from the parent and have a lower

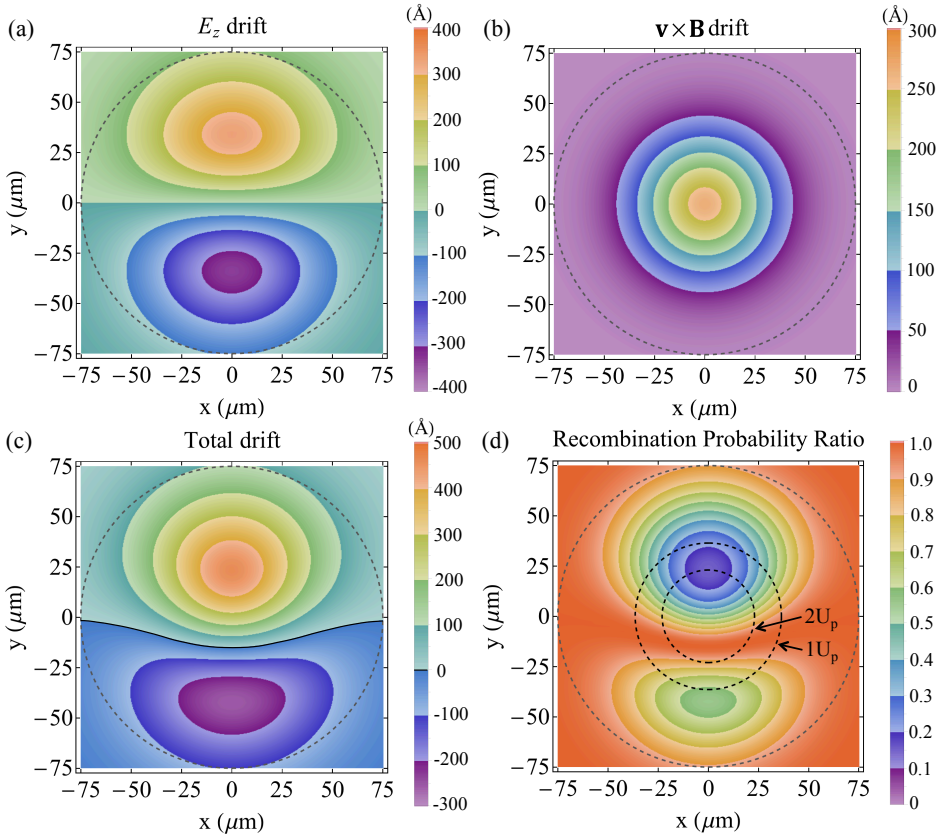

Figure 4.4: Spatially-resolved Lorentz displacements and resulting recombination probability ratio (RPR) for a Gaussian focus with $\lambda_L = 10$ µm ($I_L = 2.77 \times 10^{14}$ W/cm^2, $w = 50$ µm, $\phi_0 = 18°$). (a) δ_{E_z}, (b) $\delta_{\boldsymbol{v}\times\boldsymbol{B}}$, (c) δ_L, (d) RPR. The outer dashed circles represent the inside wall of a waveguide that this Gaussian mode would couple to optimally. The middle and inner dashed circles in (d) represent the radii within which $1U_p$ and $2U_p$ HHG can be generated, corresponding to 2.5 keV and 5.1 keV, respectively.

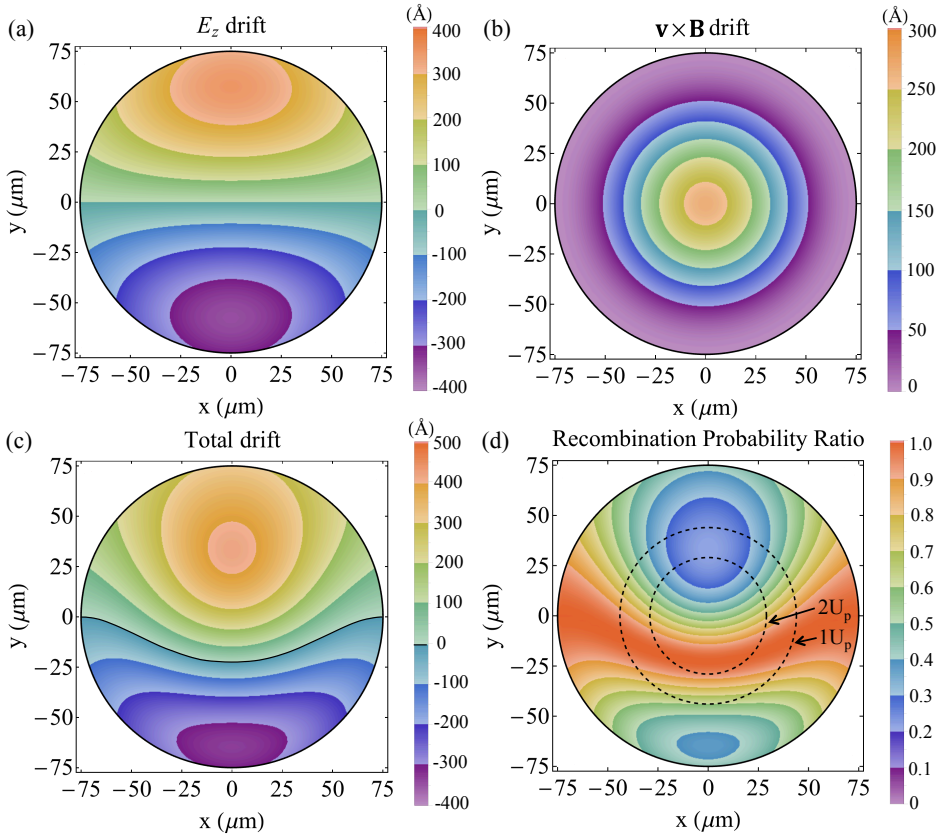

Figure 4.5: Spatially-resolved Lorentz displacements and resulting recombination probability ratio (RPR) for a EH_{11} waveguide mode with $\lambda_L = 10$ μm ($I_L = 2.77 \times 10^{14}$ W/cm^2, I.D. $= 2a = 150$ μm, $\phi_0 = 18°$). (a) δ_{E_z}, (b) $\delta_{\boldsymbol{v}\times\boldsymbol{B}}$, (c) δ_L, (d) RPR. The outer and inner dashed circles in (d) represent the radii within which $1U_p$ and $2U_p$ HHG can be generated, corresponding to 2.5 keV and 5.1 keV, respectively.

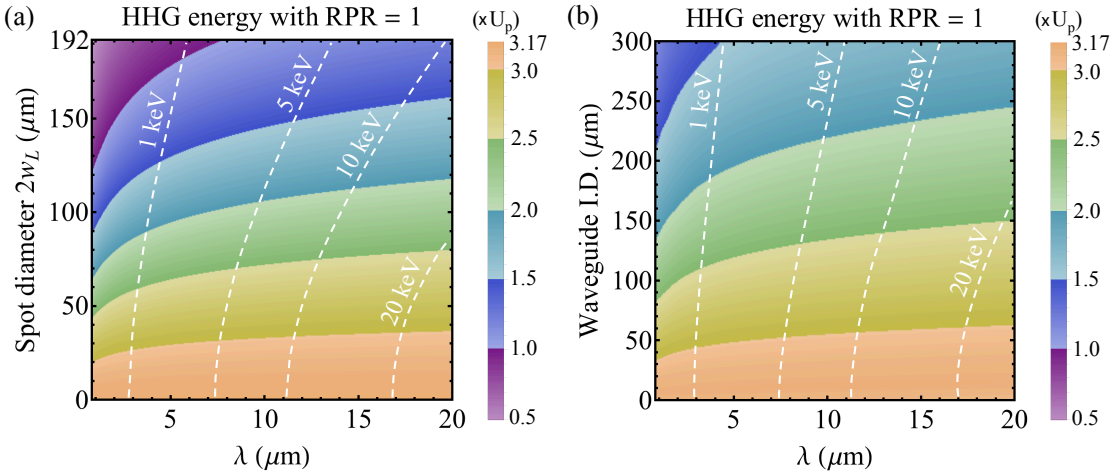

Figure 4.6: Energy of the harmonic emitted at the location of drift cancellation, corresponding to $RPR = 1$. The color scale corresponds to energies in terms of the ponderomotive potential $U_p \propto I_L \lambda_L^2$, while the dashed lines indicate energy contours in keV. The cutoff ionization phase $\phi_0 = 18°$ is used. The Gaussian focus geometry is shown in (a), while the waveguide geometry is shown in (b). The vertical axes of both plots give comparable mode sizes.

probability of recombining. For later phases, the low field strength results in reduced ionization rates, and thus, reduced harmonic emission. Performing a weighted integral of the recombination probability ratio over the entire phase range can provide an approximation of the total half-cycle HHG mode. The appropriate weighting function $f(\phi_0)$ to incorporate the phase-dependent effects follows the harmonic yield scaling described in [53] Eqs. (5)-(7):

$$f(\phi_0) = \omega_{ADK}(\phi_0) \times \tau_f^{-3}(\phi_0)/E_L^2(\phi_0), \tag{4.15}$$

Figure 4.7 shows the phase-integrated RPR for all harmonic energies in both the Gaussian focus (a) and waveguide (b) geometries. Figures 4.7(c) and 4.7(d) are identical to 4.7(a) and 4.7(b), but only HHG energies above $1U_p$ contribute. Primarily due to differences in mode shape, there is a larger area with nonzero RPR in Fig. 4.7(d) than in Fig. 4.7(c), indicating a mode-averaged flux advantage for the waveguide case over the Gaussian focus case. It is important to note that different ionization phases will have different spatial profiles for the individual drifts, and thus, the final RPR profile. As a result, different spectral regions will be emitted with different spatial modes, giving rise to complicated spectral-spatial dynamics when propagation and phase-matching are considered.

4.6 Lorentz Force Compensation through Noncollinear Geometries

The analysis in the previous sections relies on the interplay between the two components of the Lorentz drift in finite laser modes, δ_{E_z} and $\delta_{\boldsymbol{v}\times\boldsymbol{B}}$. However, the magnitude of δ_{E_z} can only be comparable to $\delta_{\boldsymbol{v}\times\boldsymbol{B}}$ when the mode size w approaches λ_L. If drift cancellation is desired in a large mode scenario ($w >> \lambda_L$), then it is impractical to rely on the inherent E_z field of the single-beam mode. Additional fields would then be necessary.

Recent work in HHG has been performed using two-beam noncollinear geometries with linear or bi-circular polarizations, which in itself has interesting phase-matching and selection rules [51, 145, 96, 94, 40, 14, 130, 129]. Here we propose a similar method that can generate a forwards field ellipticity that can act in the same direction as the magnetic Lorentz force, thereby enabling

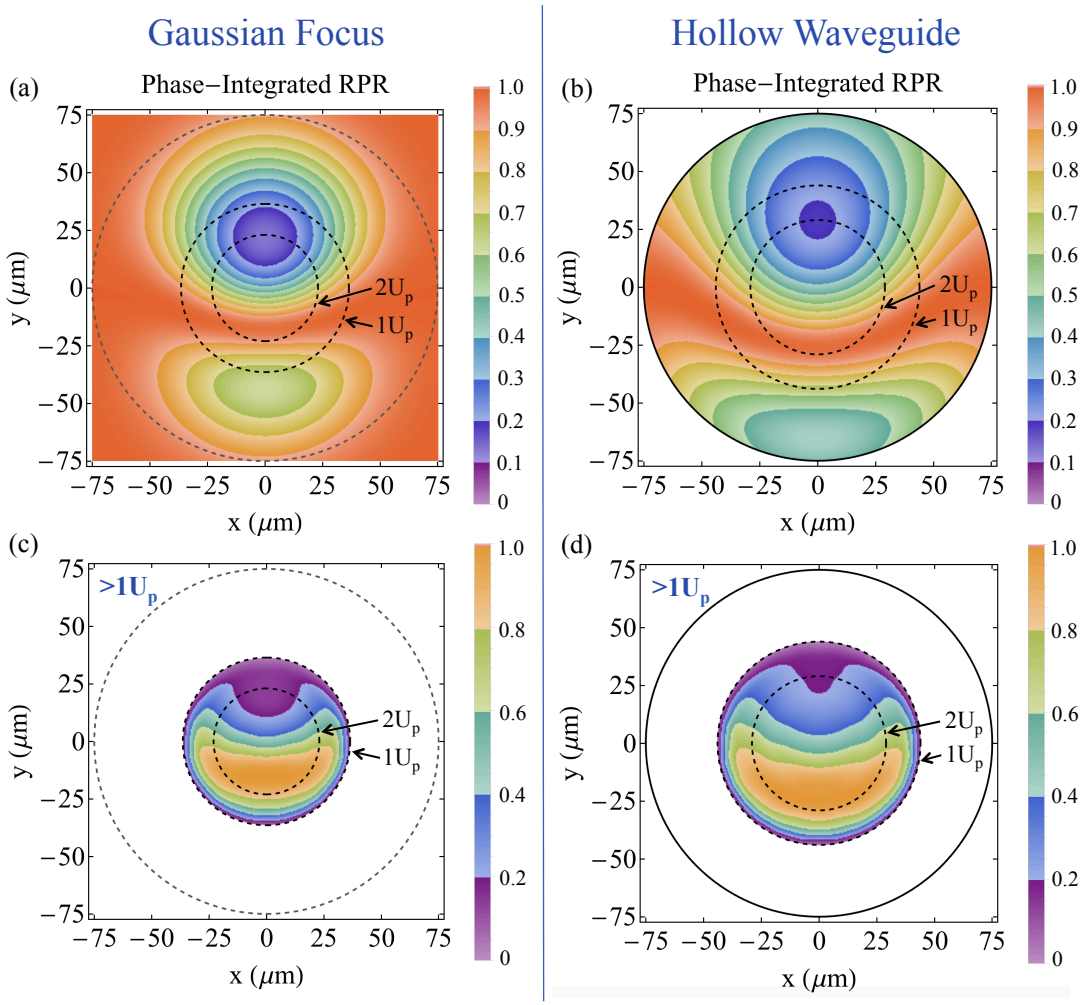

Figure 4.7: Spatially-resolved, phase-integrated recombination probability ratio (RPR) for all harmonics vs plateau and cutoff harmonics. Plots (a) and (c) correspond to a Gaussian focus geometry, while plots (b) and (d) correspond to a waveguide geometry. All harmonic energies contribute in (a) and (b), while only energies above 1Up contribute in (c) and (d). For all cases, the driving laser has wavelength $\lambda_L = 10$ µm, spot radius $w = 50$ µm (I.D. $= 2a = 150$ µm), and peak intensity $I_L = 2.77 \times 10^{14}$ W/cm^2.

drift cancellation. The experimental geometry uses two noncollinear, counter-rotating, circularly polarized beams of equal intensity and wavelength, as shown in Fig. 4.8(a). In a collinear geometry, adding counter-rotating circular polarizations with the same amplitude and frequency yields a linear polarization, where the polarization angle depends on the relative phase between the two added beams; in a noncollinear geometry, however, there is a projection of the fields along the forward direction defined by the bisecting centerline between the two crossing beams (defined as the z-direction here). Certain locations within the overlapping region will result in the constructive addition of these z-field projections, which when combined with the transverse field results in a forwards ellipticity. In other words, the major axis of the elliptical polarization will lie within the x-y plane, while the minor axis is along the z-direction.

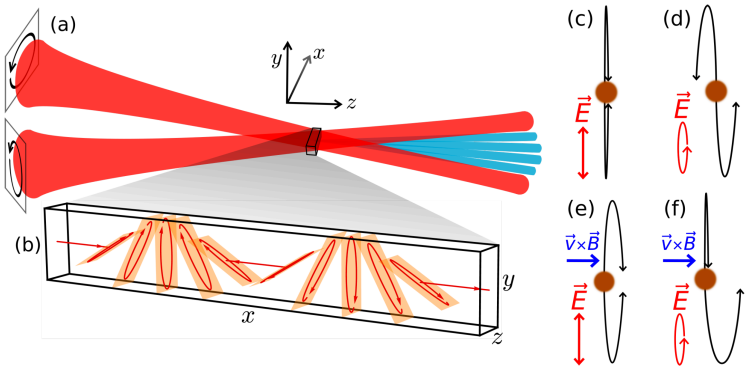

Figure 4.8: Two noncollinear, circularly polarized beams (a) produce a polarization gradient across their focus in the transverse direction (b), including points with forwards ellipticity. This makes the usual linear trajectories (c) take paths that miss the ion (d), which when added to the effect of the magnetic Lorentz force (e) achieve one recollision per cycle (f), re-enabling the harmonic emission. Adapted from [102].

Because the z-directed force from the forward ellipticity oscillates in sign, the electron will experience an alternating forward and backward drift each half-cycle (Fig. 4.8(d)). Even in the noncollinear beam case, the magnetic $\boldsymbol{v}\times\boldsymbol{B}$ drift will be along the forward z–direction (Fig. 4.8(e)). Again, the electron will experience additive and canceling drift components in neighboring half-cycles (Fig. 4.8(f)). As a result of the half-cycle symmetry breaking of the electron's trajectories,

the resulting harmonic emission from neighboring half-cycles can be viewed as an unbalanced interferometer, giving a high sensitivity measure of how the magnetic Lorentz force influences the ionized electron during the HHG process.

A quantum mechanical analysis of the harmonic emission can be performed for the non-collinear, bi-circular geometry following similar steps as presented in Section 1.3.1. In this geometry, the laser vector potential is modified from the plane-wave form of Eq. (1.38), with the following form (at $z = 0$ and small crossing angle):

$$\boldsymbol{A}(\boldsymbol{r}, t) \approx -\frac{E_{L0}}{\omega_L} \begin{pmatrix} \cos(kx \sin(\theta)) \\ sin(kx \sin(\theta)) \\ 0 \end{pmatrix} \cos(\omega_L t) \tag{4.16}$$

Although the small angle approximation results in near-zero amplitude for A_z, larger crossing of the two beams results in a periodic modulation along the z-axis. A maximal forwards-ellipticity is achieved when $kx \sin(\theta) = \pi/2$, in which case:

$$\boldsymbol{A}(\boldsymbol{r}, t) = -\frac{E_{L0}}{\omega_L} \begin{pmatrix} 0 \\ \cos(\omega_L t) \\ \sin(\theta) \sin(\omega_L t) \end{pmatrix} \tag{4.17}$$

Because there is an experimental mechanism to adjust the forward ellipticity (crossing half-angle θ), it can be varied to control the amount of drift cancellation with $\delta_{\boldsymbol{v}\times\boldsymbol{B}}$ as well as measure it. Because of the half-cycle asymmetry of the total drift, the returning electron's wavefunction overlap with the bound electron can be reduced for large drift (Eq. (4.12)), but small drifts can still produce electron phase asymmetries, leading to the possibility to generate even harmonics. The strength of the even harmonics should depend on the forward ellipticity, which varies spatially. As a result, the far-field emission pattern of the even harmonics is predicted to be influenced by this spatially-varying pattern. Recent experiments have used beam half-angles θ on the order of a few degrees [130], resulting in ellipticities $\epsilon = \sin(\theta) \approx 9\%$ (a sufficient amount to counteract significant magnetic drifts).

With the vector potential from Eq. (4.16), the quantum action $S(\boldsymbol{p}, t, t')$ can be calculated, leading to a nonzero harmonic dipole for even and odd harmonic frequencies. For a single atom located in a maximal ellipticity region, the dipole emission strength was calculated and plotted for various driving parameters in Figures 4.9 and 4.10. For $I_L = 10^{17}$ W/cm^2 (nearly relativistic intensity) [2] and a relatively short wavelength of 800 nm (Fig. 4.10), the magnetic Lorentz drift is shown to significantly reduce the harmonic emission from the ideal dipole scenario [21]. Partially compensating for the magnetic component by introducing a slight crossing ($\theta = 2°$), the harmonic emission largely recovers and could be improved further.

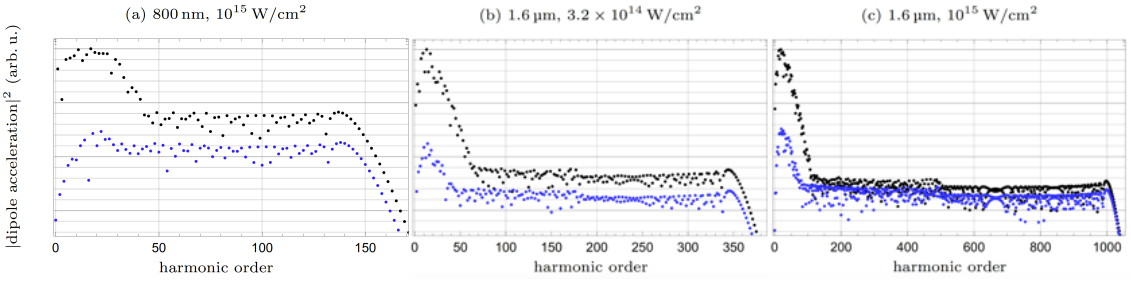

Figure 4.9: Nondipole calculations of odd (black) and even (blue) harmonics produced in helium for driving wavelengths 800 nm and 1.6 μm, intensities of 3.2×10^{14} and 10^{15} W/cm^2, and a crossing half-angle of $\theta = 4°$. The arbitrary vertical scale is logarithmic, and z-polarized harmonics are removed from the result. Even and odd harmonics are emitted with intensity ratios of $\sim 10^{-3}$ for 800 nm drivers and $\sim 10\%$ for strong mid-IR fields at 1.6 μm and 10^{15} W/cm^2. Adapted from [102].

The importance of these findings is that the half-cycle symmetry breaking in the full quantum calculation predicts the presence of even harmonics at much lower intensities and shorter wavelengths than the semi-classical, amplitude-only approach would suggest. Even harmonics resulting from nondipole effects should be detectable (within 2–3 orders of magnitude of the odd harmonics) even for 800 nm drivers, and certainly for 1.6 μm drivers at 10^{15} W/cm^2. This new result from the full quantum calculation indicates that the harmonic spectrum has a sensitive dependence on the quantum phase asymmetry of the returning electron. It is predicted that using

[2] Note that this toy problem only considers microscopic emission, and macroscopic effects could prohibit phase-matched HHG in such high intensity regimes, where the ionization levels would be large. Possible exceptions are described in Section 5.3.

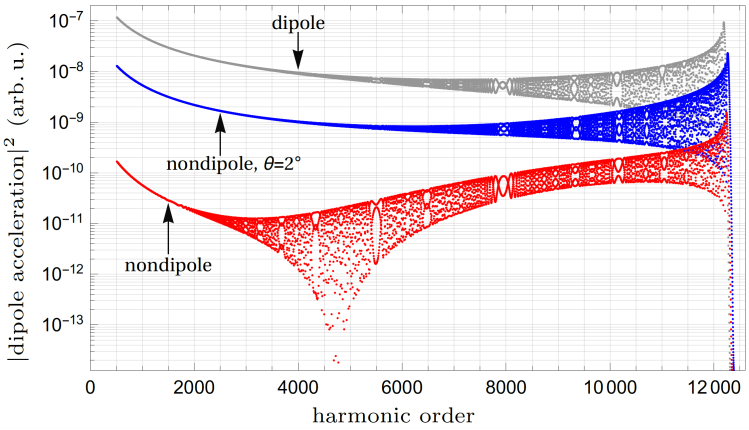

Figure 4.10: Calculations of the above-threshold harmonic emission from the Ne^{6+} ion for an 800 nm, $I_L = 10^{17}$ W/cm^2 driver. The first pair of quantum orbits and the uniform approximation were used for the calculation, and z-polarized harmonics were discarded. For zero crossing angle (linear polarization), nondipole effects ($\boldsymbol{v} \times \boldsymbol{B}$) reduce the emission by two orders of magnitude compared to the emission using the dipole-approximation. With $\theta = 2°$, the resulting forward ellipticity causes the harmonic emission to partially recover. Adapted from [102].

current OPA technology to achieve moderate mid-IR wavelengths, nondipole effects during non-collinear, bi–circular HHG should be measurable through the spectrum. Importantly, the reduction of total HHG flux as a result of Lorentz drift effects is not expected to be significant until driving wavelengths ~ 6 µm are approached (using optimal intensities) as discussed in Section 4.5.

In addition to being nonzero, the even harmonics can be easily distinguished from the typical odd harmonics through their natural angular separation in the noncollinear geometry. As demonstrated in [130] for odd harmonics, momentum and energy conservation dictates that for an odd photon to be emitted, an odd number of driving photons must be added together. Further, conservation of spin angular momentum for bi-circular drivers dictates that n photons are taken from one beam and $n+1$ taken from the other, giving the harmonic a net transverse momentum of $\pm\hbar k_x = \pm\hbar k \sin(\theta)$ [103, 122]. For even harmonics, an even number of photons are added through parametric conversion via the tensor operator $\hat{\boldsymbol{r}} \otimes \hat{\boldsymbol{p}} : \boldsymbol{\nabla A}$. Ultimately, the even harmonic can absorb -2, 0, or 2 units of $\hbar k_x$ transverse momentum, giving linear or circular polarizations. As a result, the odd and even harmonics will be emitted at different angles and should be distinguishable at a detector without the need for a grating spectrometer.

4.7 Experimental Signatures of the Lorentz Drift

There are a number of experimental indicators that can confirm the Lorentz drift effects predicted in this chapter. One of the most important challenges when using mid-IR drivers is the reduction in total HHG flux. It may be experimentally possible to distinguish the super-Gaussian scaling due to the Lorentz drift in Eq. (4.14) from the polynomial scaling due to quantum diffusion, but would likely prove difficult. The quantum diffusion scaling is dominant and would obscure the Lorentz drift contribution.

The Lorentz displacement is also expected to affect the HHG spatial mode. It has been demostrated that as the laser wavelength is increased, the HHG emission from only one half-cycle of the driver is fully phase-matched, generating a single X-ray burst even for a multi-cycle driver (Chapter 2, [18]). Therefore, for sufficiently long driving wavelengths and ideal phase-matching

conditions, an isolated HHG pulse should be produced with an asymmetric mode profile along the polarization direction, as indicated by Fig. 4.7. Further, varying the intensity or carrier-envelope-phase (CEP) of the driving pulse can cause the particular half-cycle that is phase-matched to change, thus causing the asymmetric HHG mode to flip about the x-axis. Imaging this mode onto an X-ray CCD camera and adjusting the intensity or CEP could reveal a signature of the spatially-dependent Lorentz drift. In contrast, for the lower photon energy range where multiple half-cycles contribute to the HHG signal, a more symmetric mode is expected that could obscure the Lorentz drift signature, but a full spatio-temporal attosecond pulse characterization technique could be employed to reveal the spatio-temporal asymmetry [58].

When multiple half-cycles of the driver contribute constructively to HHG, individual harmonics are spectrally resolved. Using single-color drivers, only odd order harmonics are observed due to the emission of HHG bursts every half-cycle. This typical twice-per-cycle emission in the time domain causes the energy spacing of harmonics in the spectral domain to be twice the fundamental photon energy. Even harmonics are, therefore, not allowed. However, the Lorentz displacement can break the half-cycle symmetry in some spatial regions and thus give rise to even harmonics. Section 4.6 provides a method for observing even harmonics when using a noncollinear bicircular geometry. For single beam drivers with finite spatial modes, even harmonics can also be observed. Looking off-axis in Fig. 4.7, the recombination probability ratio is close to unity in the lower half of the mode (i.e. δ_{E_z} cancels $\delta_{\boldsymbol{v}\times\boldsymbol{B}}$). In the next half-cycle, this spatial location will not experience the same drift cancellation due to the sign flip of δ_{E_z} but not $\delta_{\boldsymbol{v}\times\boldsymbol{B}}$. At this spatial position, there will be bright emission, followed by weak emission during the next half-cycle, and so on. A portion of this signal will have the usual $\lambda_L/2$ periodicity, which produces odd harmonics. Additionally, there will be a portion that has λ_L periodicity that will give rise to every harmonic, including the even orders. By analyzing the asymmetry of Fig. 4.7, it is possible to predict the mode profile of the even and odd harmonics. By using an imaging spectrometer that can separate the individual harmonics of a 10 µm driver near $1U_p$, one would expect to observe a signal similar to that shown in Fig. 4.11. Here, the peak intensity of the even harmonics is close to 30% that of the odd harmonics,

but this ratio approaches unity as the driving wavelength and harmonic energy are increased (i.e. 20 µm and $2U_p$). Again, note that this result includes only the modulations in amplitude, and that half-cycle asymmetries in the electron's quantum phase can shift the absolute spectral positions of the harmonics [102]. Experimentally, resolving the individual harmonics with such long driving wavelengths and large harmonic energies would prove to be difficult, but might be possible with the use of a Fourier transform spectrometer, similar to the one used in Chapter 2, [18].

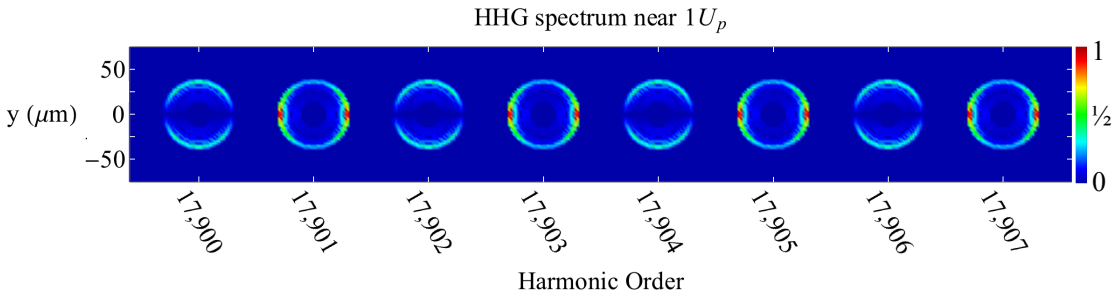

Figure 4.11: Predicted HHG spectrum near $1U_p$ using a driving laser with $\lambda_L = 10$ µm, $w = 50$ µm, and $I_L = 2.77 \times 10^{14}$ W/cm^2. The moderate spatial and temporal asymmetry of the Lorentz drift gives rise to even harmonics with a two-lobed structure along the polarization direction (y).

4.8 Lorentz Drift Summary

The theory presented in this chapter has provided a deeper investigation of the full Lorentz force and its effect during strong field ionization and recollision-based processes such as HHG. From the analysis, it is clear that the Lorentz drift should not significantly affect the probability of recollision for driving laser wavelengths less than 6 µm and moderate intensities $I_L < 10^{15}$ W/cm^2. For longer wavelengths, the magnetic Lorentz force can result in non-negligible electron drifts, but this drift can be canceled by the influence of the longitudinal electric field E_z that arises in a tight focus or in crossed beam geometries. The interplay between the two components produces a spatially-varying drift that is zero in some locations of the mode. Thus, the Lorentz drift should not completely shut off the HHG process, even for hard X-ray HHG driven by 10 µm wavelengths or longer.

Chapter 5

Pushing HHG to Higher Photon Energies

In Chapter 2, the temporal and spectral properties of HHG emission were investigated when long wavelength, mid-infrared drivers are used. To date, the hard X-ray regime has been inaccessible via HHG. Although there is an obvious route to this spectral region through the $\lambda_L^{(1.6-1.7)}$ macroscopic scaling law, ultrafast driving lasers with wavelength greater than 10 µm would be necessary. The unavailability of such high-power, ultrafast lasers has limited efforts in this regard. It is possible to generate far-infrared light with ultrafast pulse durations using OPA or OPCPA technologies. Additionally, self-phase-modulation of 10 µm CO_2 laser light and pulse compression could result in sufficient bandwidth to support several-cycle pulses at the necessary wavelengths. Furthermore, the full Lorentz force and the associated longitudinal drifts are not expected to completely shut off the HHG process, as determined in Section 4.5. More detrimental to the process would be the unfavorable flux scaling of $\lambda_L^{-(5-9)}$ [161, 120, 42, 98]. This scaling has been overcome in the past by taking advantage of the increased phase-matching pressure for long wavelengths, which results in a larger emitter-density [160]. However, phase-matching pressures quickly reach solid densities when such long wavelengths are considered, introducing further limitations such as the solid medium's damage threshold.

Achieving hard X-ray harmonics can be approached through alternative techniques that do not rely on increasing the driving laser wavelength. The cutoff photon energy scaling of $\lambda_L^{(1.6-1.7)}$ is a macroscopic scaling using a conventional single-beam geometry. The single-atom cutoff scales as $I_L\lambda_L^2$, which indicates that there exists an alternative route to increasing the harmonic cutoff:

through the peak intensity. Of course, the phase-matching requirement cannot simply be neglected, but quasi-phase-matching (Section 1.4.4) is an option that can be considered. Additionally, multi-beam geometries could bypass the typical $\lambda_L^{(1.6-1.7)}$ scaling. A noncollinear geometry that makes use of high-order difference frequency generation (HDFG) is one possible approach that will be discussed in Section 5.3. Alternative modes or polarization states could also alter the typical phase-matching laws, and should be investigated for possible utility in hard X-ray HHG.

5.1 HHG using Cylindrical Vector Beams

Driving HHG with linear polarization has been a successful approach to frequency conversion. The three step model of HHG (Section 1.2) makes use of the 1-D trajectory of the electron to ensure a high probability of recollision and harmonic emission. Motion in non-polarization directions can be detrimental to the HHG process, such as in the presence of significant magnetic Lorentz forces (Chapter 4) or driving fields with elliptical polarizations [154, 130, 129]. Bichromatic, bi-circular drivers can result in high recollision probabilities, but each harmonic pulse in the HHG pulse train has been shown to be locally linear, with an average HHG polarization ellipticity when measured over the entire pulse train [128].

Aside from linear and circular, there are other polarization states that can be explored. Cylindrical vector beams (CVBs) contain unique polarization states that can continuously vary from radial to azimuthal polarizations (Appendix A). Additionally, multiple modes of CVBs can be combined to produce complex, spatially-varying polarization states. The microscopic and macroscopic high harmonic process can possibly be altered under these driving fields. Figure 5.1 shows the spatial intensity distributions and polarization directions for the simplest radial and azimuthal polarization modes (LG_{01}):

$$\mathrm{LG}_{01} = \frac{2}{\sqrt{\pi}\, w(z)^2}\, r\, e^{-r^2/w(z)^2} \tag{5.1}$$

For radially- and azimuthally-polarized CVBs with the "doughnut" modes shown in Fig. 5.1, the microscopic three step model should hold true. Although the polarization varies spatially, it

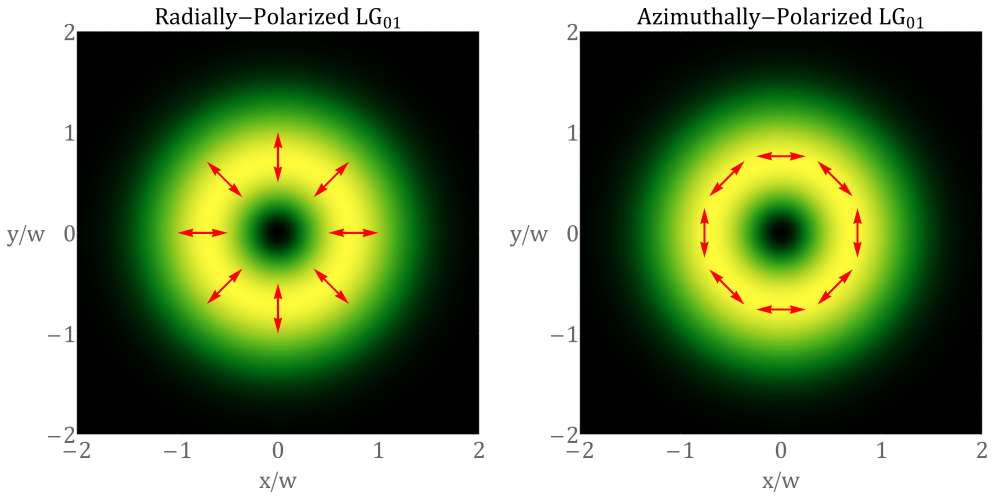

Figure 5.1: Intensity distributions and polarization directions for the radially- and azimuthally-polarized Laguerre-Gauss LG_{01} modes (Appendix A).

is locally linear on the length scale of the electron trajectories (on the order of nanometers for near-infrared wavelengths). Thus, harmonic emission will also be locally linear. Overall, the HHG mode will take on a similar shape and polarization as the driving field, though the nonlinear nature of the harmonic process will increase the amplitude contrast of the HHG mode.

CVBs, like Gaussian beams, exhibit interesting field properties when tightly focused. As explained in Section 4.2, a longitudinal electric field component E_z arises when the mode size w approaches the wavelength λ. In the linearly-polarized Gaussian case, the E_z component takes on a two-lobed spatial structure due to its proportionality with $\frac{\partial E_\psi}{\partial \psi}$, where ψ represents the polarization direction. For the radially-polarized LG_{01} mode, this derivative is largest in the center of the mode. Since the primary polarization component E_r is zero in the center, E_z can be the strongest component in a small region around the center of a tightly focused beam. Figure 5.2 depicts the field strengths of the radial and longitudinal components throughout a tight focus.

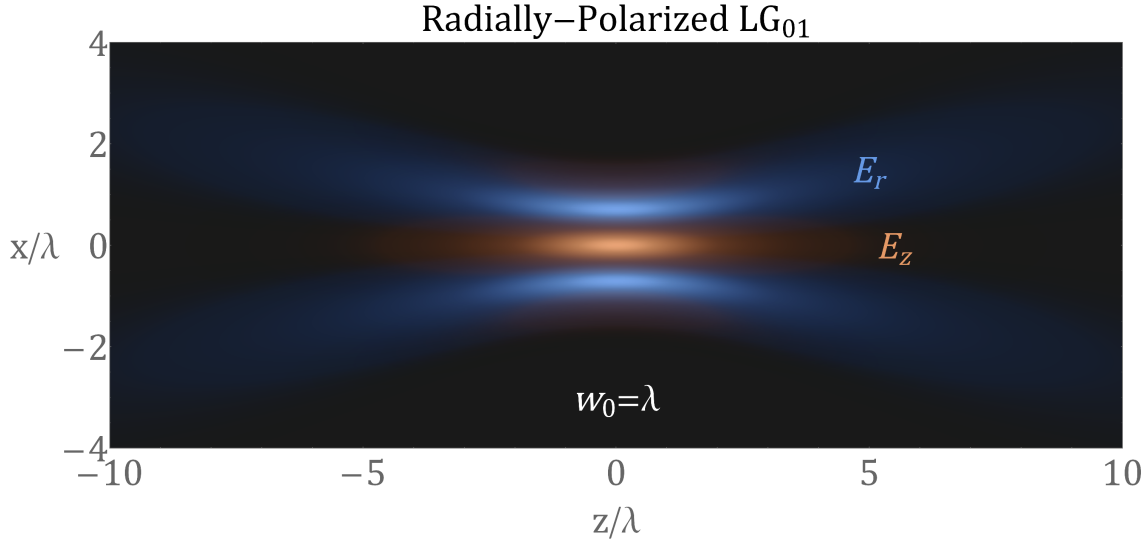

Figure 5.2: Radial and longitudinal field strengths of a radially-polarized LG_{01} mode throughout a tight focus. The longitudinal electric field E_z dominates over the radial component E_r at the center of the mode in the focus.

A possible consequence of this strong longitudinal field is that Lorentz drift compensation

could be performed when driving with long wavelength CVBs. Another possibility is that harmonics could be generated from centrally-localized electrons that take on primarily longitudinal trajectories. Ultimately, the single-atom harmonic emission will take on the Larmor radiation pattern from Fig. 1.15. Looking in the far field but close to the z-axis, this emission pattern takes on a similar "doughnut" mode profile with radial polarization. Furthermore, macroscopic effects can cause the near-axis emission to be enhanced, provided that phase-matching is achieved. Otherwise, phase-matched HHG may be optimized at larger angles off-axis. Ultimately, radially-polarized HHG could be possible by directly driving electrons along the radial directions in a loose focus, or alternatively by driving them in the z-direction in a tight focus.

Because there is roughly zero intensity at the center of a loosely focused CVB mode, it is possible for there to be a phase singularity at that location. This is true for CVBs that contain orbital angular momentum (OAM), which manifests as a continual phase shift along the azimuthal direction: $e^{il\phi}$. That is, following a path along $\hat{\phi}$ from $\phi = 0$ to $\phi = 2\pi$, the phase of the driving beam can shift a total of $2\pi l$, with positive or negative integer l corresponding to the OAM topological charge. Figure 5.3 illustrates the wavefront for such beams. [1] Locally, the field components are unchanged and develop in time according to the laser frequency. Thus, HHG is possible on the microscopic scale. Macroscopically, the harmonic emission would inherit the spiraling phase of the driver. However, due to the nonlinear nature of the process, the integer l would be multiplied by the harmonic order q, resulting in a much more rapidly varying phase and much higher OAM for the harmonic beam [50]. In [59] and [44], multiple OAM driving beams are combined to allow tunability of the OAM contained within the HHG output.

In all of the HHG experiments performed to date using CVB drivers, focusing geometries in gas jets/cells were used. However, gas-filled hollow waveguides are valid candidates for CVB HHG since there exist radially- and azimuthally-polarized guided modes: the TE_{0q} and TM_{0q} modes, respectively (Appendix A). Future work could investigate HHG driven by these guided modes in hollow waveguides, which would result in an HHG flux benefit from the larger pressure-length

[1] Recently, fractional orbital angular momentum beams have been theoretically investigated [165].

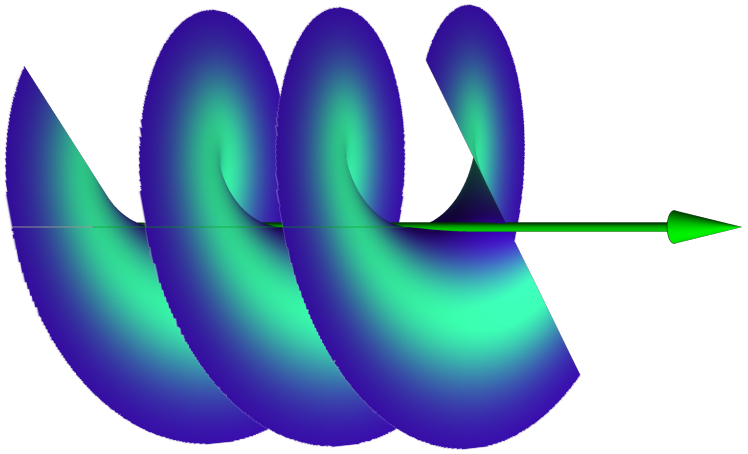

Figure 5.3: Wavefront and intensity shading for a $l = 2$ OAM beam.

products achievable in a guided geometry. Finally, HHG driven by long wavelength CVBs could show advantages in terms of cancellation of the magnetic Lorentz force by the strong E_z field component that is present on-axis in tightly focused CVBs. Therefore, CVB-driven HHG could be a route to reaching the hard X-ray regime.

5.2 HHG in Bragg Waveguides

To date, the highest photon energy measured from an HHG source is in the soft X-ray regime at 1.6 keV, resulting from the use of a long wavelength 3.9 µm driver [161]. The HHG geometry used for this demonstration was a high pressure gas-filled waveguide with an inner diameter of 200 µm and length of 5 cm. The waveguide was supplied with a gas pressure up to 80 atm. Due to harmonic reabsorption concerns (Section 1.4.5), vacuum must immediately follow the high pressure section. Necessarily, there exists a large pressure differential over a relatively short distance after the HHG medium. From basic principles in fluid dynamics, the PV throughput (Q) through a pipe of length L and radius R in the laminar regime is given by:

$$Q_{pipe} = \frac{d(PV)}{dt} = C_{pipe}(P_2 - P_1) = \left[\frac{\pi R^4}{8\eta L}\left(\frac{P_1 + P_2}{2}\right)\right](P_2 - P_1) \tag{5.2}$$

Here, η is the dynamic viscosity of the fluid. It is clear from Eq. (5.2) that the gas flow rate scales strongly with the pressures P_1 and P_2. If the lower pressure is at vacuum $P_1 \approx 0$, then the flow rate $Q \propto P_2^2$. Thus, handling the high gas flows resulting from phase-matching pressures up to 80 atm requires a considerable effort in pumping speed and geometry.

Long wavelength HHG drivers that require higher pressures (Fig. 1.27) represent a significant experimental challenge. The gas flow problem can be partially alleviated by using smaller radius waveguides since the conductance scales as R^4. This solution has the additional advantage of requiring less pulse energy for the driving laser to reach equivalent peak intensities, since the intensity of the driver scales as R^2 (assuming all else held constant). This is especially advantageous in relaxing the front-end laser requirements for long wavelength drivers, since these sources generally require complicated frequency conversion schemes. However, long wavelengths guided in small

diameter capillaries can suffer from significant propagation loss. As described in Appendix A, the complex propagation constant γ_{pq} has an imaginary component that depends on the ratio λ/a, and this imaginary component is responsible for propagation loss. Even in the case described in [161], 3.9 µm light guided through a 200 µm diameter waveguide for 5 cm will only transmit a maximum of 72% of the light coupled in. Decreasing the waveguide diameter further would result in significantly more propagation loss that would influence the ability to ionize and phase-match the HHG process over centimeter length scales.

Eliminating the detrimental effects of high propagation loss is desirable for efficient, phase-matched HHG driven by long wavelengths, while maintaining a manageable gas flow rate. One approach to reduce the propagation loss is to use Bragg waveguides. These waveguides are similar to simple hollow capillaries, except that the inside wall of the waveguide contains a multilayer coating (Fig. 5.4). This multilayer is effectively designed to provide high reflectance of the guided light, similar to Bragg mirrors. Bragg mirrors utilize quarter-wave optical thicknesses for alternatingly high and low index materials, resulting in constructive interference for the reflected beam. The layer thicknesses can be designed to reflect a band of wavelengths, and they must be adjusted to account for the angle of incidence. For a guided EH_{11} mode, the angle of incidence is not immediately apparent since the mode has a flat wavefront and propagates along the length of the waveguide. However, a transverse wavenumber $k_{\perp,\sigma}$ can be determined by taking the standard deviation of the mode's spatial frequency content. The effective incidence angle can then be calculated: $\theta_\sigma = \cos^{-1}(k_{\perp,\sigma}/k)$. The transverse wavenumber $k_{\perp,\sigma}$ is inversely proportional to the waveguide radius a, so the effective incidence angle θ_σ is less glancing as the ratio a/λ decreases. Bragg layers for the inside wall of the waveguide can therefore be designed with θ_σ in mind.

Of course, this simplistic effective-angle approach is a first order approximation. A full electromagnetic solution for the mode and its propagation constant can be numerically calculated, as demonstrated by Badding *et al.* in [17] through the use of COMSOL Multiphysics® software. In their work, alternating layers of silicon and silica are deposited through high-pressure chemical vapor deposition (Fig. 5.4). Silicon and silica are ideal materials for the Bragg layers due to their

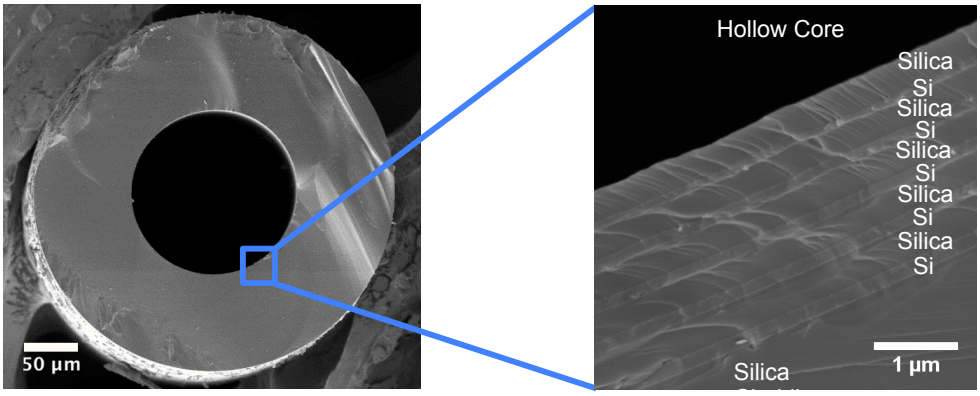

Figure 5.4: Scanning electron microscope image of a Bragg fiber. Alternating Si and Silica layers are visible on the inside wall of the capillary.

high index contrast and high damage thresholds. These Bragg waveguides are ideal for handling the high peak powers and intensities that are present during HHG conditions, and their ability to provide a spectral band of high transmission (even for low values of a/λ) makes them useful for HHG driven by mid-IR light in small diameter capillaries. Experiments are currently being performed to generate and characterize mid-IR driven HHG in small diameter Bragg waveguides. Success in this current effort could provide a bright, stable light source in the water window regime (284–541 eV), lending itself to high resolution microscopies and spectroscopies of biologically-relevant samples.

5.3 Noncollinear High-Order Difference Frequency Generation

In Section 1.4.1, the equations governing phase-matching were presented. Before the standard single-beam scenario was investigated in detail, the general vectorial phase-mismatch was written in Eq. (1.62) as:

$$\begin{aligned} \Delta\boldsymbol{k} &\equiv \boldsymbol{k}_Q(\omega_Q) - \sum_j m_j\, \boldsymbol{k}_j(\omega_j) = 0 \\ \omega_Q &= \sum_j m_j\, \omega_j \end{aligned} \tag{5.3}$$

Here, we see conditions that ensure momentum and energy conservation for the HHG process, regardless of how many beams are involved or what their frequencies and propagation vectors are. However, the integers m_j are not constrained to be positive, indicating that for multi-beam geometries, a high-order difference frequency generation (HDFG) process is possible. In this section, consider two plane-wave driving fields propagating in different directions ($\hat{\boldsymbol{k}}_1$ and $\hat{\boldsymbol{k}}_2$) in the x-z plane, each with its own frequency (ω_1 and ω_2) as depicted in Fig. 5.5. Assume these fields are interacting in a partially ionized gas medium. In this situation, Eq. (5.3) can be written as:

$$\begin{aligned} \Delta\boldsymbol{k} &= \boldsymbol{k}(\omega_Q) - m_1\, \boldsymbol{k}_1(\omega_1) - m_2\, \boldsymbol{k}_2(\omega_2) \\ \omega_Q &= m_1\, \omega_1 + m_2\, \omega_2 \end{aligned} \tag{5.4}$$

To satisfy the phase-matching condition in this vectorial situation, both the harmonic angle θ_Q and magnitude $k_Q(\omega_Q) \equiv |\boldsymbol{k}_Q(\omega_Q)|$ must match the angle and magnitude of the sum $[m_1\, \boldsymbol{k}_1(\omega_1) +$

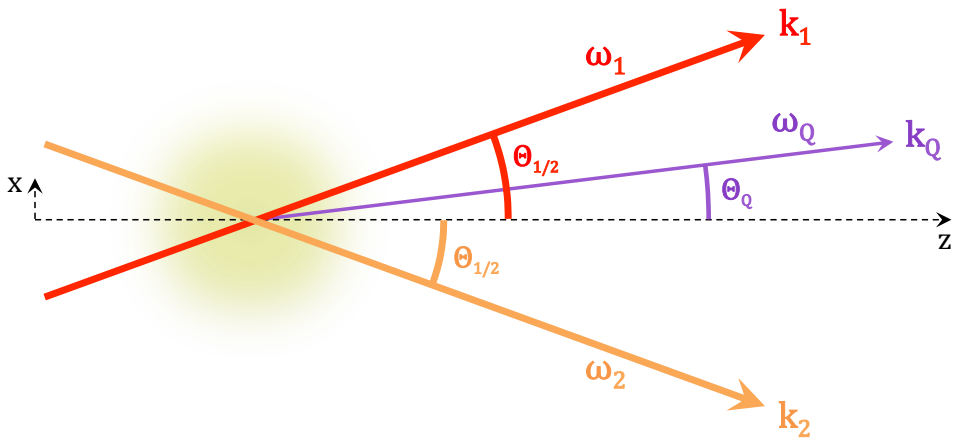

Figure 5.5: Geometry for a two-beam noncollinear frequency upconversion process (HHG or HDFG). Note that for HDFG ($m_1 > 0$ and $m_2 < 0$), the harmonic emission angle lies outside the sector spanned by the two driving vectors: $\theta_Q > \theta_{1/2}$.

$m_2\,\boldsymbol{k}_2(\omega_2)]$. These can be considered separately:

$$\theta_Q = \tan^{-1}\left(\frac{m_1 k_1(\omega_1) - m_2 k_2(\omega_2)}{m_1 k_1(\omega_1) + m_2 k_2(\omega_2)}\tan(\theta_{1/2})\right) \tag{5.5}$$

$$k_Q(\omega_Q) = m_1 k_1(\omega_1)\cos(\theta_{1/2} - \theta_Q) + m_2 k_2(\omega_2)\cos(\theta_{1/2} + \theta_Q) \tag{5.6}$$

The magnitudes for each of the wavevectors can be calculated by summing the vacuum, atom, ion, plasma, and geometrical contributions described in Section 1.4.1. Solving Eq. (5.5) and Eq. (5.6) simultaneously can be performed numerically, allowing straightforward exploration of the large parameter space of the problem $\{\omega_1, \omega_2, m_1, m_2, \theta_{1/2}, \bar{P}, \eta\}$.

HHG in two-beam noncollinear geometries have been experimentally investigated for multiple colors [14] and even bi-circular polarization states [130]. Further, HDFG has been observed experimentally [51, 145]. One benefit to HDFG is that phase-matching can occur at ionization levels that exceed the conventional critical level for single-beam HHG. This is possible by taking advantage of the negative value for m_2 and the large harmonic emission angle, both of which reduce $k_Q(\omega_Q)$ to a greater degree than $k_1(\omega_1)$ or $k_2(\omega_2)$. This was predicted and experimentally verified by L'Huillier *et al.* in [51], where a strong fundamental beam at 800 nm was crossed with a weak (5%) second harmonic beam (400 nm) in an Argon gas cell. The crossing angle was small ($\theta_{1/2} \approx 1$ mrad), the pulse duration was ~ 40 fs, and the peak intensity was approximately 2×10^{14} W/cm^2. They observed HDFG photon energies up to ~ 40 eV, and a maximum of 2 second harmonic photons subtracted ($m_1 = 22$–24, $m_2 = -2$). Although HDFG was demonstrated in this work, the maximum harmonic energy observed (~ 40 eV) did not exceed the single-beam phase-matching cutoff (~ 50 eV for 800 nm in Ar). This could be due to the low peak intensity used, which would give a single-atom cutoff of ~ 54 eV. It is possible the low crossing angle used did not allow phase-matched HDFG up to the single-atom cutoff. However, the ionization level under these phase-matched conditions was approximately 2–3 times the critical ionization level for Ar ($\eta_c \approx 4.5\%$), indicating that HDFG can bypass the conventional phase-matching limitations for single-beam, collinear geometries.

HDFG was again performed in [145], where slightly larger crossing angles $\theta_{1/2} \sim 25$ mrad were used. For the HDFG case presented, a strong 385 nm beam and weaker (10%) 790 nm beam were focused into an Ar gas jet. The pulse duration was 45 fs, and the combined intensity was 3×10^{14} W/cm^2. They report a theoretical maximum HDFG order of 29 (for the 790 nm beam), representing a photon energy of 43 eV, though the maximum measured energy for the strong 385 nm experimental case is not clear from the text. In any case, the conventional phase-matching cutoff in Ar at 400 nm is ~ 29 eV, or ~ 50 eV for 790 nm. Despite phase-matching HDFG in the presence of high ionization levels ($4 \times \eta_c \approx 56\%$), the maximum photon energy observed did not exceed the single-beam phase-matching cutoff for one of the wavelengths used (790 nm: $E_{PMC} \sim 50$ eV), when HDFG should allow phase-matching significantly beyond either of the traditional cutoffs.

It is surprising that even though higher ionization levels can be present during phase-matched HDFG, no experiment has demonstrated photon energies that exceed the typical single-beam phase-matching cutoff E_{PMC} for the contributing wavelengths. This can most likely be attributed to the small crossing angles, low pulse energies, and choice of gas used in the two experiments described above. Increasing the crossing angle $\theta_{1/2}$ allows for more extreme ionization levels to be present while phase-matching HDFG, which would allow higher peak intensities (and therefore higher single-atom cutoffs) to be used. Due to the linear scaling of the single-atom cutoff with intensity, much larger pulse energies might have been necessary to noticeably exceed the conventional phase-matching cutoff. It is not specified in the past work whether significantly increased driving pulse energies were attempted. It is possible that the choice of low-I_p Ar gas for the harmonic medium would cause highly dynamic multiple-ionization that would limit the temporal window over which phase-matched HDFG could occur.

To thoroughly investigate whether HDFG could significantly bypass the restrictive single-beam phase-matching cutoff, a new experiment could be performed with the following conditions:

(1) Large crossing angles $\theta_{1/2}$ that allow phase-matching of HDFG processes even at 100% ionization levels.

(2) Large enough peak intensities for a single-atom cutoff that is significantly greater than the conventional E_{PMC}.

(3) A harmonic medium with high first- and very high second-ionization potentials (He) such that there is a significant portion of time where the ionization level is stabilized close to 100% despite the very high peak intensities present.

The third point can be important for ensuring multiple half-cycles of the driving lasers contribute to the emission, which increases the emitted flux and can eliminate the need for carrier-envelope-phase (CEP)-stable driving lasers. Electrons that contribute to the HDFG signal in this $\sim 100\%$ ionization case would be given from the He^+ ion, resulting in doubly-ionized He while the electron is in its propagation step (HHG from ions is considered in [134]).

As an example, numerical calculations were performed to determine the phase-matching conditions when two crossed driving beams generate extreme ionization levels up to $\sim 100\%$ in He. It is assumed that there is a strong primary driver at 800 nm and a weak secondary beam (to simulate the situation where $m_2 < 0$ and $|m_1| >> |m_2|$, which results in $\theta_Q \approx \theta_{1/2}$). The geometric phase-mismatch terms were ignored, which is reasonable for loose focusing geometries in a gas jet/cell. Table 5.1 shows the calculated phase-matching conditions and the resulting harmonic outputs. Note that for the temporally stable case of $\sim 100\%$ ionized He, there is a range of pulse durations dt that can give the desired ionization level at the peak of the pulse. This is not true for the cases where $\eta < 100\%$, since the ionization level (and $\Delta\boldsymbol{k}$) changes rapidly past $\Delta\boldsymbol{k} = 0$.

The driving wavelengths used in Table 5.1 were chosen since ultrafast laser technology at these wavelengths has reached impressively high peak power levels, enabling the most extreme HDFG configurations listed. Long wavelength drivers in the mid-IR regime could be considered, provided that a stable, high power, ultrafast OPA or OPCPA is available [47, 139]. With such a driving source, the single-atom cutoff can increase dramatically, possibly bringing the hard X-ray regime within reach through phase-matched, mid-IR driven, noncollinear HDFG.

Table 5.1: Calculations for several example driving conditions during noncollinear HDFG where phase-matching is achieved. The gas medium is He. The left side of the table specifies the conditions that satisfy phase-matching. The middle section gives the characteristics of the phase-matched HDFG output. The right side states the minimum laser peak intensity to achieve the the HDFG photon energy $E_{SAC} = E_Q$, and the corresponding pulse duration that results in ionization level η at the center of the pulse.

λ_1 (nm)	λ_2 (nm)	m_1	m_2	$\theta_{1/2}$	$\bar{P}$	η	θ_Q	E_Q (eV)	I_L (W/cm^2)	dt
800	800	250	-1	14°	0.15	40%	14.1°	386	1.9×10^{15}	20
800	800	600	-10	19°	0.5	100%	19.6°	915	4.7×10^{15}	30–100
800	400	400	-5	10°	0.23	90%	10.5°	605	3.1×10^{15}	20
800	400	1000	-8	20°	0.5	100%	20.6°	1,526	7.9×10^{15}	20–40

5.4 Future Work in Mid-IR Driven HHG

Continuing to push the HHG photon energy and flux to higher levels has a number of benefits for materials and light science applications. For instance, coherent diffractive imaging (CDI) is a powerful form of optical microscopy. Using HHG or other X-ray light sources, CDI can obtain the complex transmission/reflection profile of samples at the nanometer scale. In CDI, the achievable spatial resolution achievable is limited by the experimental geometry (NA), the probe wavelength (λ), and its spectral bandwidth ($\Delta\lambda$). To achieve better spatial resolution, a smaller probe wavelength can be used. Extending the HHG probe energy from the EUV (13 nm) into the water window (2.3–4.4 nm) would be a natural next step, particularly because light in the water window region transmits highly through water, making it a strong candidate for performing CDI on biological samples suspended in water/ice. Furthermore, there is a strong need for high resolution lithography and microscopy for quality control in the semiconductor industry, which is continually taking steps to reduce feature sizes.

One difficulty with using a standard HHG light source for water window CDI is that the conventional approach to reaching the water window requires mid-IR drivers, which results in naturally broad spectral bandwidths as discussed in Chapter 2. With such a large value for $\Delta\lambda/\lambda$, there will be a detriment to the spatial resolution achievable through CDI. It is possible to narrow the spectral bandwidth through the use of narrow bandpass dielectric mirrors and an appropriate selection

of foil filters. An X-ray monochromator can also be designed using glancing incidence gratings and mirrors. Unfortunately, these approaches reduce the HHG flux that would be incident on the sample, thus requiring long integration times and high levels of stability. This effect, combined with the unfavorable HHG flux scaling law $\lambda_L^{-(5-9)}$, makes mid-IR driven HHG CDI a challenge, though not impossible. Efforts are currently being made to use the aforementioned methods to achieve new levels of spatial resolution through water window CDI. In particular, the use of long Bragg waveguides designed for mid-IR wavelengths (Section 5.2) can allow a greater level of HHG flux to build up due to the increased pressure-length product.

Furthermore, alternative approaches can be devised to avoid some of the limitations from the conventional HHG bandwidth and flux. For instance, the traditional HHG cutoff energy scales as $\lambda^{(1.6-1.7)}$ according to the phase-matching constraints. This scaling has held true for infrared wavelengths, but has been overcome using ultraviolet drivers to perform HHG in multiply-ionized plasmas. In [134], HHG from ions was demonstrated, resulting in a previously unexpected harmonic cutoff > 280 eV using 270 nm drivers (Fig. 5.6). Furthermore, the HHG flux for these high energy regions were equal to or greater than the flux from longer wavelength drivers, which is predictable from the reduced amount of quantum diffusion. Additionally, the HHG emission was observed in discrete harmonics, as opposed to a supercontinuum, making this UV-driven light source a strong candidate to perform water window CDI. As discussed in Section 5.3, noncollinear high-order difference frequency generation could also be performed to produce high-flux, monochromatic harmonics at photon energies beyond the typical phase-matching cutoff.

HHG at high photon energies, regardless of the driving configuration, is useful for a plethora of applications, ranging from high resolution CDI microscopy to broadband XAFS spectroscopy. The attosecond time-scales of the HHG pulses makes this light source unique and well-suited for dynamic measurements, such as dynamic XAFS. By pumping a thin lattice with visible light, and subsequently interrogating with a broadband HHG probe, the perturbation to the lattice from the pump can be determined. Acoustics, thermal transport, and the density of states for phonons [91, 133, 52] can all be probed on ultrafast time scales in this experiment. Efforts are currently

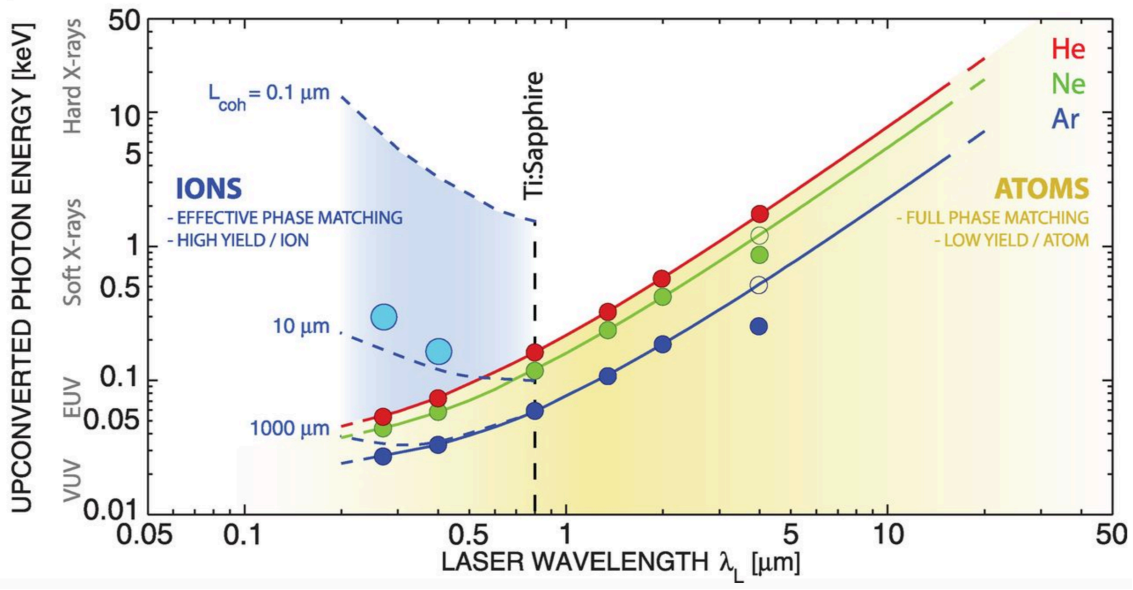

Figure 5.6: Bright HHG from atoms and ions for UV to mid-IR driving lasers. The experimental data are plotted as circles. The solid lines plot the theoretical full phase-matching limits, including only the index of neutral atoms. The dashed lines also include the refractive indices of ions, which extend UV-driven HHG effective phase matching into the soft x-ray region. Adapted from [134].

being made toward this goal of dynamic XAFS probed by mid-IR driven HHG.

Finally, driving with much longer wavelengths beyond 10 µm can bring hard X-ray HHG within reach, but the three step model will be influenced by relativistic Lorentz drift effects (Chapter 4) that should be noticeable in the HHG amplitude for driving wavelengths beyond 6 µm. Experimental verification of the Lorentz drift can be obtained through the approaches detailed in Section 4.7. Furthermore, it is possible to directly measure the Lorentz drift through measurement of the ionized electrons' momenta. Through a technique called velocity map imaging (VMI), ionized electrons can be imaged in a transverse momentum space. A strong laser ionizes atoms in a gas jet, after which the ionized electrons are accelerated by an external electrostatic potential. The potential is designed to form a momentum-space image of the electrons at a microchannel plate detector [33]. For short wavelength drivers, the atomic and molecular states can be probed without the influence of relativistic effects from the laser field. However, long wavelength drivers will generate these effects that could then be observable in the VMI measurement [73]. The magnetic component of the Lorentz force would tend to shift the electron momentum distribution along the forward z-direction of the laser. The E_z component would tend to broaden the distribution due to both the forward and backward contributions. [2] However, if the gas jet size is small compared to mode (and if the mode is sufficiently small for a significant E_z component) then the jet could be translated across the mode, thus sampling different regions of the mode (Fig. 5.7). Thus, the E_z component would vary as a function of the jet's position, giving a direct measurement of the E_z field profile along one dimension. This measurement could impart empirical verification of the theory presented in Section 4.7.

[2] Single-cycle drivers may be necessary to probe just the Lorentz force that exists during the three step model, since the electrons that make it to the VMI detector will inevitably be subjected to the remainder of the field following ionization. The influence of multiple cycles after ionization could distort the desired signal.

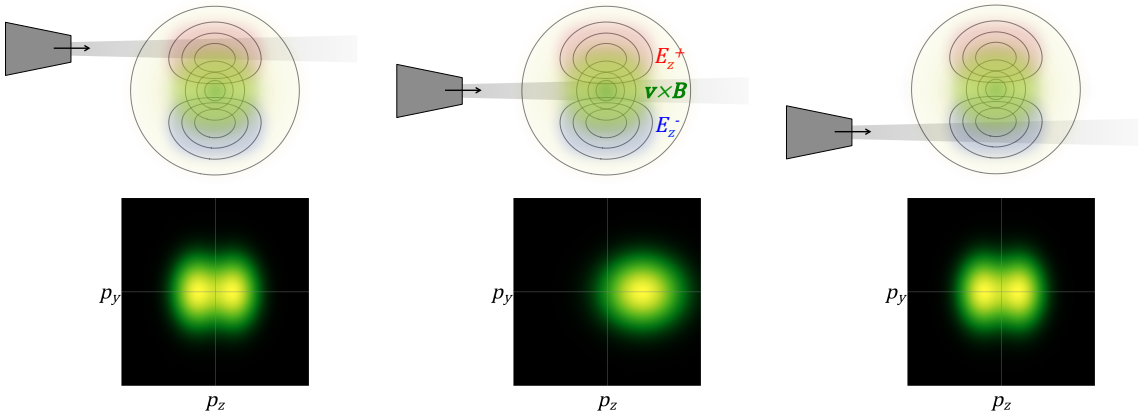

Figure 5.7: Scanning VMI concept to measure the longitudinal Lorentz force during long wavelength strong field ionization in a spatially-resolved way. A small diameter gas jet can be translated across the laser mode to sample the E_z and $\boldsymbol{v} \times \boldsymbol{B}$ contributions separately. A predicted signal at the VMI is shown for three locations of the scan.

Chapter 6

Concluding Remarks

Light is, indeed, an incredibly powerful tool for making observations of the physical world. In particular, light in the EUV and X-ray regimes enable unique and higher resolution measurements than is possible using longer wavelengths. High-order harmonic generation provides a route to produce light in these useful spectral ranges starting with lasers operating at more accessible wavelengths. Free-electron lasers and synchrotrons are complementary technologies that can exceed the capabilities of HHG in some aspects, but have certain drawbacks where HHG can fill the gaps. Investigating the physical mechanisms and limitations of the HHG source can reveal new routes for improving the technology, thus advancing its ability to be applied in highly sensitive experiments. Some examples of applications where HHG has shown unique utility are coherent diffractive imaging, dynamic measurement (Chapter 2), and broadband spectroscopies (Chapter 3).

This dissertation has covered several illuminating studies of HHG in the temporal and spectral domains when the process is driven by long wavelength, mid-infrared light. Interestingly, the characteristics of the harmonic emission are highly dependent on the driving laser parameters and geometries. As the driving laser wavelength is increased, the harmonic cutoff and bandwidth naturally broadens, while the emitted pulse train reduces in length until a single isolated burst of phase-matched harmonics with sub-femtosecond duration is achieved. The resulting supercontinuum has particular utility in X-ray absorption fine structure spectroscopies, where the nanoscale lattice structure can be probed. These spectroscopies have been performed using the broadest HHG

bandwidth achieved to date, extending to 1.6 keV. Pushing this harmonic cutoff further would conventionally require the use of longer wavelength drivers approaching the far-infrared regime. Gaussian focus HHG geometries would typically be necessary for these long wavelengths, but the use of novel Bragg waveguides could enable high flux, high cutoff HHG in waveguides. However, long driving wavelengths can also result in relativistic effects during the three step model of HHG, resulting in longitudinal Lorentz drift effects that could cause the electron to miss its parent ion. Accounting for all of the forces involved does not indicate HHG would be shut off entirely, however, and it is possible for HHG to occur even with driving wavelengths beyond 10 μm and harmonic cutoffs in the hard X-ray regime. The use of cylindrical vector beams or multi-beam geometries can also be used to compensate for relativistic effects, and also to create new phase-matching conditions for sum and difference frequency processes. Through high-order difference frequency generation in a two-beam noncollinear geometry, it could be possible to significantly exceed the conventional phase-matching cutoff, opening up the possibility to reach the soft X-ray regime or further when simply using the intense, highly accessible, and highly HHG-efficient colors from Ti:sapphire lasers (800 nm). Pushing the limits of the HHG spectral characteristics would certainly enable new levels of capability in CDI microscopies, X-ray spectroscopies, and more.

In the past decade, HHG technology and theory have progressed at tremendous rates, and there are many more directions in which HHG can grow. The future looks promising for frequency conversion, especially as driving laser technologies advance to higher intensities, shorter pulse durations, and longer wavelengths. Using next-generation driving lasers in novel geometries, with the guidance of high-level computations, and through collaboration within the expanding HHG science community, it is very likely that hard X-ray harmonics (among other new capabilities) will be achieved within the near future.

Bibliography

[1] R. L. Abrams. Coupling losses in hollow waveguide laser resonators. IEEE Journal of Quantum Electronics, 8(11):838–843, 1972.

[2] D. E. Adams, L. S. Martin, M. D. Seaberg, D. F. Gardner, H. C. Kapteyn, and M. M. Murnane. A generalization for optimized phase retrieval algorithms. Opt. Exp., 20(22):24778–24790, 2012.

[3] P. Agostini, F. Fabre, G. Mainfray, G. Petite, and N. Rahman. Free-free transitions following six-photon ionization of xenon atoms. PRL, 42(17):1127–1130, 1979.

[4] M. V. Ammosov, N. B. Delone, and V. P. Krainov. Tunnel ionization of complex atoms and of atomic ions in an alternating electromagnetic field. Sov. Phys. JETP, 64(6):1191–1194, 1986.

[5] M. R. Matthewsand B.P. Anderson, P.C. Haljan, D.S. Hall, C.E. Wieman, and E.A. Cornell. Vortices in a Bose-Einstein condensate. PRL, 83(13):2498–2501, 1999.

[6] S. M. Angel, T. J. Kulp, and T. M. Vess. Remote-Raman spectroscopy at intermediate ranges using low-power CW lasers. Appl. Spec., 46(7):1085–1091, 1992.

[7] D. Attwood. Soft x-rays and extreme ultraviolet radiation: principles and applications. Cambridge Univ Press, 2007.

[8] P. Balcou, P. Salières, and A. L. L'Huillier. Generalized phase-matching conditions for high harmonics: The role of field-gradient forces. PRA, 55(4):3204–3210, 1997.

[9] M. Bashkansky, P. Bucksbaum, and D. Schumacher. Asymmetries in above-threshold ionization. PRL, 60(24):2458–2461, 1988.

[10] H. H. Bauschke, P. L. Combettes, and D. R. Luke. Phase retrieval, error reduction algorithm, and Fienup variants: a view from convex optimization. JOSA A, 19(7):1334–1345, 2002.

[11] H. H. Bauschke, P. L. Combettes, and D. R. Luke. Finding best approximation pairs relative to two closed convex sets in Hilbert spaces. J. Approx. Theory, 127:178–192, 2004.

[12] C. Benko, T. K. Allison, A. Congöz, L. Hua, F. Labaye, D. C. Yost, and J. Ye. Extreme ultraviolet radiation with coherence time greater than 1 s. Nat. Phot., 8:530–536, 2014.

[13] Helmholtz Zentrum Berlin. BESSY FEMTOSPEX. `https://www.helmholtz-berlin.de/forschung/oe/fg/mi-synchrotron-radiation/synchrotron/photons/x-ray-pulses/femtospex/index_en.html`.

[14] J. B. Bertrand, H. J. Worner, H.-C. Bandulet, É Bisson, M. Spanner, J.-C. Kieffer, D. M. Villeneuve, and P. B. Corkum. Ultrahigh-order wave mixing in noncollinear high harmonic generation. PRL, 106:023001, 2011.

[15] O. Bunk, M. Dierolf, S. Kynde, I. Johnson, O. Marti, and F. Pfeiffer. Influence of the overlap parameter on the convergence of the ptychographical iterative engine. Ultramicroscopy, 108:481–487, 2008.

[16] A. Butler, D. J. Spence, and S. M. Hooker. Guiding of high-intensity laser pulses with a hydrogen-filled capillary discharge waveguide. PRL, 89:185003, 2002.

[17] S. Chaudhuri, J. R. Sparks, R. He, and J. V. Badding. Hollow core silicon-silica Bragg fiber. In CLEO, San Jose, United States, May 10–15 2015. OSA.

[18] M.-C. Chen, C. Mancuso, C. Hernández-García, F. Dollar, B. Galloway, D. Popmintchev, P.-C. Huang, B. Walker, L. Plaja, A. A. Jaron-Becker, A. Becker, M. M. Murnane, H. C. Kapteyn, and T. Popmintchev. Generation of bright isolated attosecond soft x-ray pulses driven by multicycle midinfrared lasers. PNAS, 111(23):E2361–E2367, 2014.

[19] Ming-Chang Chen. Modifying Driving Laser Wavelength to Generate Coherent, Ultrafast X-rays from Phase-Matched High-Order Harmonics. PhD thesis, University of Colorado at Boulder, 2012.

[20] J. Cheng, C.-S. Liua, S. Shang, D. Liu, W. Perrie, G. Dearden, and K. Watkins. A review of ultrafast laser materials micromachining. Optics and Laser Technology, 46:88–102, 2013.

[21] C. C. Chirila, N. J. Kylstra, R. M. Potvliege, and C. J. Joachain. Nondipole effects in photon emission by laser-driven ions. PRA, 66(6):063411, 2002.

[22] I. P. Christov, M. M. Murnane, and H. C. Kapteyn. High-harmonic generation of attosecond pulses in the single-cycle regime. PRL, 78:1251–1254, 1997.

[23] L. Cicchitelli and H. Hora. Longitudinal field components for laser beams in vacuum. PRA, 41(7):3727–3732, 1990.

[24] O. Cohen, X. Zhang, A. Lytle, T. Popmintchev, M. Murnane, and H. Kapteyn. Grating-assisted phase matching in extreme nonlinear optics. PRL, 99(5):053902, 2007.

[25] E. Constant, D. Garzella, P. Breger, E. Mével, Ch. Dorrer, C. Le Blanc, F. Salin, and P. Agostini. Optimizing high harmonic generation in absorbing gases: Model and experiment. PRL, 82(8):1668–1671, 1999.

[26] P. B. Corkum. Plasma perspective on strong-field multiphoton ionization. PRL, 71(13):1994–1997, 1993.

[27] National Research Council. Controlling the Quantum World: The Science of Atoms, Molecules, and Photons. The National Academies Press, Washington, DC, 2007.

[28] N. B. Delone and V. P. Krainov. Energy and angular electron spectra for the tunnel ionization of atoms by strong low-frequency radiation. J. Opt. Soc. Am. B, 8(6):1207–1211, 1991.

[29] Y. Deng, Z. Zeng, Z. Jia, P. Komm, Y. Zheng, X. Ge, R. Li, and G. Marcus. Direct evidences for inner-shell electron-excitation by laser induced electron recollision. ArXiv e-prints, September 2015.

[30] T. Ditmire, K. C. Kulander, J. K. Crane, H. Nguyen, and M. D. Perry. Calculation and measurement of high-order harmonic energy yields in helium. JOSA B, 13(2):406–411, 1996.

[31] A. Dubey. Laser beam machining a review. Int. J. Mach. Tools and Man., 48:609–628, 2008.

[32] J. H. Eberly, J. Javanainen, and K. Rzazewski. Above-threshold ionization. Phys. Rep., 204:331–383, 1991.

[33] A. T. J. B. Eppink and D. H. Parker. Velocity map imaging of ions and electrons using electrostatic lenses: Application in photoelectron and photofragment ion imaging of molecular oxygen. Rev. Sci. Instr., 68(9):3477–3484, 1997.

[34] European XFEL. `http://www.xfel.eu/`.

[35] M. Feld, editor. Laser Spectroscopy IX. Academic Press, Inc., 1989.

[36] M. Ferray, A. L. L'Huillier, X. F. Li, L. A. Lompré, G. Mainfray, and C. Manus. Multiple-harmonic conversion of 1064 nm radiation in rare gases. J. Phys. B: AMO Phys., 21:L31–L35, 1988.

[37] J. R. Fienup. Reconstruction of an object from the modulus of its Fourier transform. Opt. Lett., 3(1):27–29, 1978.

[38] J. R. Fienup. Phase retrieval algorithms: a comparison. Appl. Opt., 21:2758–2769, 1982.

[39] D. N. Fittinghoff, P. R. Bolton, B. Chang, and K. C. Kulander. Observation of nonsequential double ionization of helium with optical tunneling. PRL, 69:2642, 1992.

[40] S. V. Fomichev, P. Breger, B. Carré, P. Agostini, and D. Zaretsky. Non-collinear high-harmonic generation. Laser Phys., 12:383, 2002.

[41] B. La Fontaine. Lasers and Moores law. SPIE Professional, page 20, Oct. 2010.

[42] M. V. Frolov, N. L. Manakov, and A. F. Starace. Wavelength scaling of high-harmonic yield: Threshold phenomena and bound state symmetry dependence. PRL, 100(17):173001, 2008.

[43] B. R. Galloway, D. Popmintchev, E. Pisanty, D. D. Hickstein, M. M. Murnane, H. C. Kapteyn, and T. Popmintchev. Lorentz drift compensation in high harmonic generation in the soft and hard x-ray regions of the spectrum. Opt. Exp., 24(19):21818–21832, 2016.

[44] D. Gauthier, P. Rebernik Ribic, G. Adhikary, A. Camper, C. Chappuis, R. Cucini, L. F. DiMauro, G. Dovillaire, F. Frassetto, R. Géneaux, P. Miotti, L. Poletto, B. Ressel, C. Spezzani, M. Stupar, T. Ruchon, and G. De Ninno. Tunable orbital angular momentum in high-harmonic generation. Nat. Comm., 8:14971, 2017.

[45] R. Gerchberg and W. O. Saxton. Phase determination from image and diffraction plane pictures in the electron microscope. Optik, 34:275–283, 1971.

[46] R. Gerchberg and W. O. Saxton. A practical algorithm for the determination of phase from image and diffraction plane pictures. Optik, 35(2):237–246, 1972.

[47] Michael Gerrity. Development of a High Energy, kHz, Mid-Infrared OPCPA Laser for keV High Harmonic Generation. PhD thesis, University of Colorado at Boulder, 2015.

[48] S. Ghimire, A. D. DiChiara, E. Sistrunk, P. Agostini, L. F. DiMauro, and D. A. Reis. Observation of high-order harmonic generation in a bulk crystal. Nat. Phys., 7:138–141, 2011.

[49] B. Henrich, K. Z. Hatsagortsyan, and C. H. Keitel. Positronium in intense laser fields. PRL, 93(1):013601, 2004.

[50] C. Hernández-García, A. Picón, J. San Román, and L. Plaja. Attosecond extreme ultraviolet vortices from high-order harmonic generation. PRL, 111(8):083602, 2013.

[51] C. M. Heyl, P. Rudawski, F. Brizuela, S. N. Bengtsson, J. Mauritsson, and A. LHuillier. Macroscopic effects in noncollinear high-order harmonic generation. PRL, 112(14):143902, 2014.

[52] K. M. Hoogeboom-Pot, J. N. Hernandez-Charpak, E. H. Anderson, X. Gu, R. Yang, M. M. Murnane, H. C. Kapteyn, and D. Nardi. A new regime of nanoscale thermal transport: collective diffusion increases dissipation efficiency. PNAS, 112:4846–4851, 2015.

[53] M. Y. Ivanov, T. Brabec, and N. Burnett. Coulomb corrections and polarization effects in high-intensity high-harmonic emission. PRA, 54(1):742–745, 1996.

[54] K. Jain. Excimer Laser Lithography. SPIE Press, Bellingham, WA, 1990.

[55] L. V. Keldysh. Ionization in the field of a strong electromagnetic wave. Sov. Phys. JETP, 20(5):1307–1314, 1965.

[56] U. Keller. Progress in Optics, volume 46, chapter Ultrafast Solid-State Lasers. Elsevier: Amsterdam, 2004.

[57] A. V. Kim, M. Yu. Ryabikin, and A. M. Sergeev. From femtosecond to attosecond pulses. Phys. Uspekhi, 42(1):54, 1999.

[58] K. T. Kim, C. Zhang, A. D. Shiner, S. E. Kirkwood, E. Frumker, G. Gariepy, A. Naumov, D. M. Villeneuve, and P. B. Corkum. Manipulation of quantum paths for space time characterization of attosecond pulses. Nat. Phys., 9(3):159–163, 2013.

[59] F. Kong, C. Zhang, F. Bouchard, Z. Li, G. G. Brown, D. Hyuk Ko, T.J. Hammond, L. Arissian, R. W. Boyd, E. Karimi, and P.B. Corkum. Controlling the orbital angular momentum of high harmonic vortices. Nat. Comm., 8:14970, 2017.

[60] K. C. Kulander. Dynamics of short-pulse excitation, ionization and harmonic generation. In Proceedings on SILAP III, B. Piraux, ed. Plenum, New York, 1993.

[61] S. Kumar, Y. W. Parc, A. S. Landsman, and D. E. Kim. Temporally-coherent terawatt attosecond XFEL synchronized with a few cycle laser. Scientific Reports, 6(37700), 2016.

[62] Brookhaven National Laboratory. NSLS-II Storage Ring Parameters. `https://www.bnl.gov/ps/accelerator/`.

[63] Lawrence Berkeley Laboratory. Center for X-ray Optics. http://www.cxro.lbl.gov/.

[64] SLAC National Accelerator Laboratory. Record Peak Brightness. https://heds.slac.stanford.edu/our-research/record-peak-brightness.

[65] A. A. Lagatsky, F. Fusari, S. Calvez, S. V. Kurilchik, V. E. Kisel, N. V. Kuleshov, M. D. Dawson, C. T.A. Brown, and W. Sibbett. Femtosecond pulse operation of a Tm, Ho-codoped crystalline laser near 2 um. Opt. Lett., 35(2):172–174, 2010.

[66] D. A. Leonard. Observation of raman scattering from the atmosphere using a pulsed nitrogen ultraviolet laser. Nature, 216(5111):142–143, 1967.

[67] P. D. Lett, R. N. Watts, C. I. Westbrook, W. D. Phillips, P. L. Gould, and H. J. Metcalf. Observation of atoms laser cooled below the Doppler limit. PRL, 61(2):169, 1988.

[68] M. Lewenstein, Ph. Balcou, M. Yu. Ivanov, A. L. L'Huillier, and P. B. Corkum. Theory of high-harmonic generation by low-frequency laser fields. PRA, 49(3):2117–2132, 1994.

[69] A. L. L'Huillier. High-order harmonic generation in rare gases with a 1-ps 1053-nm laser. PRL, 70:774–777, 1993.

[70] A. L. L'Huillier, K. J. Schafer, and K. C. Kulander. Theoretical aspects of intense field harmonic-generation. J. Phys. B: AMO Phys., 24(15):3315–3341, 1991.

[71] David R. Lide, editor. CRC Handbook of Chemistry and Physics, chapter 10: Atomic, Molecular, and Optical Physics: Ionization Potentials of Atoms and Atomic Ions. CRC Press, Boca Raton, Florida, 84th edition, 2003.

[72] Q. Lin, S. Li, and W. Becker. High-order harmonic generation in a tightly focused laser beam. Opt. Lett., 31(14):2163–2165, 2006.

[73] A. Ludwig, J. Maurer, B. W. Mayer, C. R. Phillips, L. Gallmann, and U. Keller. Breakdown of the dipole approximation in strong-field ionization. PRL, 113(24):243001, 2014.

[74] D. R. Luke. Relaxed averaged alternating reflections for diffraction imaging. Inverse Problems, 21(1):37–50, 2005.

[75] A. L. LHuillier, L. A. Lompre, G. Mainfray, and C. Manus. Multiply charged ions induced by multiphoton absorption in rare gases at 0.53 um. PRA, 27:2503, 1983.

[76] Y. Ma, H. Yang, J. Guo, C. Sathe, A. Agui, and J. Nordgren. Structural and electronic properties of low dielectric constant fluorinated amorphous carbon films. Appl. Phys. Lett., 72(25):3353–3355, 1998.

[77] T. H. Maiman. Stimulated optical radiation in ruby. Nature, 187(4736):493–494, 1960.

[78] A. G. Manning, R. Khakimov, R. G. Dall, and A. G. Truscott. Single-atom source in the picokelvin regime. PRL, 113:130403, 2014.

[79] E. A. J. Marcatili and R. A. Schmeltzer. Hollow metallic and dielectric waveguides for long distance optical transmission and lasers. The Bell System Technical Journal, 43(4):1783–1809, 1964.

[80] J. McKeever, A. Boca, H. J. Boozer, J. R. Buck, and H. J. Kimble. A one-atom laser in a regime of strong coupling. Nature, 425:268–271, 2003.

[81] A. McPherson, G. Gibson, H. Jara, U. Johann, T. S. Luk, I. A. McIntyre, K. Boyer, and C. K. Rhodes. Studies of multiphoton production of vacuum-ultraviolet radiation in rare gases. J. Opt. Soc. Am. B, 4(4):595–601, 1987.

[82] A. Medina, F. Gayá, and F. Pozo. Compact laser radar and three-dimensional camera. JOSA A, 23:800–805, 2006.

[83] J. Meijer. Laser beam machining (LBM), state of the art and new opportunities. J. Mat. Proc. Tech., 149:2–17, 2004.

[84] J. Miao, T. Ishikawa, I. K. Robinson, and M. M. Murnane. Diffractive imaging with coherent x-ray sources. Science, 348:530, 2015.

[85] H. M. Milchberg, C. G. Durfee III, and T. J. McIlrath. High-order frequency conversion in the plasma waveguide. PRL, 75:2494, 1995.

[86] R. Miller, T. E. Northup, K. M. Birnbaum, A. Boca, A. D. Boozer, and H. J. Kimble. Trapped atoms in cavity QED: coupling quantized light and matter. J. Phys. B: At. Mol. Opt. Phys., 38(9):S551–S565, 2005.

[87] N. Milosevic, P. B. Corkum, and T. Brabec. How to use lasers for imaging attosecond dynamics of nuclear processes. PRL, 92(1):013002, 2004.

[88] E. I. Moses. Ignition and inertial confinement fusion at The National Ignition Facility. J. Phys.: Conference Series, 244:012006, 2010.

[89] M. Munoz, F. Farges, and P. Argoul. Continuous Cauchy wavelet transform of XAFS spectra. Physica Scripta, 2005(T115):221, 2005.

[90] Y. Nabekawa, T. Shimizu, Y. Furukawa, E. J. Takahashi, and K. Midorikawa. Interferometry of attosecond pulse trains in the extreme ultraviolet wavelength region. PRL, 102(21):213904, 2009.

[91] D. Nardi, M. Travagliati, M. E. Siemens, Q. Li, M. M. Murnane, H. C. Kapteyn, G. Ferrini, F. Parmigiani, and F. Banfi. Probing thermomechanics at the nanoscale: Impulsively excited pseudosurface acoustic waves in hypersonic phononic crystals. Nano Lett., 11:4126–4133, 2011.

[92] S. Palaniyappan, I. Ghebregziabher, A. DiChiara, J. MacDonald, and B. C. Walker. Emergence from nonrelativistic strong-field rescattering to ultrastrong-field laser-atom physics: A semiclassical analysis. PRA, 74:033403, 2006.

[93] A. Paul, R. A. Bartels, R. Tobey, H. Green, S. Weiman, I. P. Christov, M. M. Murnane, H. C. Kapteyn, and S. Backus. Quasi-phase-matched generation of coherent extreme-ultraviolet light. Nature, 421(6918):51–54, 2003.

[94] P. M. Paul, E. S. Toma, P. Breger, G. Mullot, F. Augé, P. Balcou, H. G. Muller, and P. Agostini. Observation of a train of attosecond pulses from high harmonic generation. Science, 292(5522):1689, 2001.

[95] G. G. Paulus, W. Becker, W. Nicklich, and H. Walther. Rescattering effects in above-threshold ionization: a classical model. J. Phys. B.: At. Mol. Opt. Phys., 27:L703–L708, 1994.

[96] J. Peatross, J. L. Chaloupka, and D. D. Meyerhofer. High-order harmonic generation with an annular laser beam. Opt. Lett., 19(13):942, 1994.

[97] Y.-P. Peng, X. Zou, Z. Bai, Y. Leng, B. Jiang, X. Jiang, and L. Zhang. Mid-infrared laser emission from Cr:ZnS channel waveguide fabricated by femtosecond laser helical writing. Sci. Reports, 5:18365, 2015.

[98] J. A. Pérez-Hernández, L. Roso, and L. Plaja. Harmonic generation beyond the strong-field approximation: the physics behind the short-wave-infrared scaling laws. Opt. Exp., 17(12):9891–9903, 2009.

[99] A. Peters, K. Y. Chung, and S. Chu. Measurement of gravitational acceleration by dropping atoms. Nature, 400:849–852, 1999.

[100] J. J. Pigeon, S. Ya. Tochitsky, C. Gong, and C. Joshi. Supercontinuum generation from 2 to 20 m in GaAs pumped by picosecond CO2 laser pulses. Opt. Lett., 39(11):3246–3249, 2014.

[101] J. Pigeona, S. Tochitsky, and C. Joshi. Nonlinear optical compression of high-power 10-um CO2 laser pulses in gases and semiconductors. In AIP Conference Proceedings **1812**, National Harbor, MD, United States, July-Aug. 2017. AIP.

[102] E. Pisanty, D. D. Hickstein, B. R. Galloway, C. G. Durfee, H. C. Kapteyn, M. M. Murnane, and M. Ivanov. High harmonic interferometry of the Lorentz force in strong mid-infrared laser fields. submitted.

[103] E. Pisanty, S. Sukiasyan, and M. Ivanov. Spin conservation in high-order-harmonic generation using bicircular fields. PRA, 90(4):043829, 2014.

[104] M. N. Polyanskiya, M. Babzien, and I. V. Pogorelsky. 100-terawatt CO2 laser: Design and current status. In AIP Conference Proceedings **1777**, San Jose, CA, United States, July 2016. AIP.

[105] T. Popmintchev, M.-C. Chen, P. Arpin, M. M. Murnane, and H. C. Kapteyn. The attosecond nonlinear optics of bright coherent x-ray generation. Nat. Phot., 4(12):822–832, 2010.

[106] Tenio Popmintchev. Tunable Ultrafast Coherent Light in the Soft and Hard X-ray Regions of the Spectrum: Phase Matching of Extreme High-Order Harmonic Generation. PhD thesis, University of Colorado at Boulder, 2009.

[107] B. Ravel and M. Newville. ATHENA, ARTEMIS, HEPHAESTUS: data analysis for x-ray absorption spectroscopy using IFEFFIT. J. Syncrotron. Rad., 12:537–541, 2005.

[108] J. Ring. The laser in astronomy. New Scientist, Jun 20, 1963.

[109] I. Robinson and R. Harder. Coherent x-ray diffraction imaging of strain at the nanoscale. Nat. Mater., 8:291–298, 2009.

[110] A. Rundquist, C. G. Durfee III, Z. Chang, C. Herne, S. Backus, M. M. Murnane, and H. C. Kapteyn. Phase-matched generation of coherent soft x-rays. Science, 280(5368):1412–1415, 1998.

[111] D. Sanchez, M. Hemmer, M. Baudisch, S. L. Cousin, K. Zawilski, P. Schunemann, O. Chalus, C. Simon-Boisson, and J. Biegert. 7 um, ultrafast, sub-millijoule-level mid-infrared optical parametric chirped pulse amplifier pumped at 2 um. Optica, 3(2):147, 2016.

[112] G. Sansone, L. Poletto, and M. Nisoli. High-energy attosecond light sources. Nat. Phot., 5(11):655–663, 2011.

[113] P. O. Schmidt, T. Rosenband, C. Langer, W. M. Itano, J. C. Bergquist, and D. J. Wineland. Spectroscopy using quantum logic. Science, 309:749–752, 2005.

[114] M. D. Schwartz. Quantum Field Theory and the Standard Model. Cambridge University Press, 2014.

[115] Matthew Seaberg. Nanoscale EUV Microscopy on a Tabletop: A General Transmission and Reflection Mode Microscope Based on Coherent Diffractive Imaging with High Harmonic Illumination. PhD thesis, University of Colorado at Boulder, 2007.

[116] B. H. Shaw, J. van Tilborg, T. Sokollik, C. B. Schroeder, and W. P. Leemans. High-harmonic generation from replenishing solid tapes. In Conference on Lasers and Electro-Optics (CLEO), San Jose, CA, United States, June 2013. IEEE.

[117] Andrej Singer. Coherence properties of third and fourth generation x-ray sources. Theory and experiment. PhD thesis, Universität Hamburg, 2012.

[118] Photonics Solutions. Quantronix Palitra Specifications - Photonics Solutions. `https://www.photonicsolutions.co.uk/upfiles/QXPalitra.pdf`.

[119] T. Tajima and J. M. Dawson. Laser electron accelerator. PRL, 43:267–270, 1979.

[120] J. Tate, T. Auguste, H. G. Muller, P. Saliéres, P. Agostini, and L. F. DiMauro. Scaling of wave-packet dynamics in an intense midinfrared field. PRL, 98(1):013901, 2007.

[121] S. Teichmann, F. Silva, S. Cousin, M. Hemmer, and J. Biegert. 0.5-kev soft x-ray attosecond continua. Nat. Comm., 7:11493, 2016.

[122] A. Fleischer *et al.* Spin angular momentum and tunable polarization in high-harmonic generation. Nat. Phot., 8(7):543–549, 2014.

[123] A. Sandhu *et al.* Generation of sub-optical-cycle, carrier-envelope-phaseinsensitive, extreme-UV pulses via nonlinear stabilization in a waveguide. PRA, 74(6):061803, 2006.

[124] B. Abbey *et al.* Quantitative coherent diffractive imaging of an integrated circuit at a spatial resolution of 20 nm. Appl. Phys. Lett., 93:214101, 2008.

[125] B. P. Abbott *et al.* Observation of gravitational waves from a binary black hole merger. PRL, 116:061102, 2016.

[126] B. Zhang *et al.* Full field tabletop EUV coherent diffractive imaging in a transmission geometry. Opt. Exp., 21(19):21970–21980, 2014.

[127] B. Zhang *et al.* High contrast 3D imaging of surfaces near the wavelength limit using tabletop EUV ptychography. Ultramicroscopy, 158:98–104, 2015.

[128] C. Chen *et al.* Tomographic reconstruction of circularly polarized high-harmonic fields: 3D attosecond metrology. Sci. Adv., 2:e1501333, 2016.

[129] C. Hernández-García *et al.* Schemes for generation of isolated attosecond pulses of pure circular polarization. PRA, 93:043855, 2016.

[130] D. D. Hickstein *et al.* Angularly separated beams of circularly polarized high harmonics. Nat. Phot., 9:743–750, 2015.

[131] D. F. Gardner *et al.* Subwavelength coherent imaging of periodic samples using a 13.5nm tabletop high-harmonic light source. Nat. Phot., 11:259–264, 2017.

[132] D. M. Gaudiosi *et al.* High harmonic generation from ions in a capillary discharge plasma waveguide. OPN, 17(12):44, 2006.

[133] D. Nardi *et al.* Probing limits of acoustic nanometrology using coherent extreme ultraviolet light. Proc. of SPIE, 8681:86810N, 2013.

[134] D. Popmintchev *et al.* Ultraviolet surprise: Efficient soft x-ray high-harmonic generation in multiply ionized plasmas. Science, 350(6265):1225–1231, 2015.

[135] D. Popmintchev *et al.* Near and extended edge x-ray absorption fine structure spectroscopy using ultrafast coherent high harmonic supercontinua. submitted.

[136] E. A. Gibson *et al.* Coherent soft x-ray generation in the water window with quasi-phase matching. Science, 302(5642):95, 2003.

[137] E. Goulielmakis *et al.* Single-cycle nonlinear optics. Science, 320:1614–1617, 2008.

[138] E. Turgut *et al.* Controlling the competition between spin transport and optically induced demagnetization in magnetic multilayers. PRL, 110:197201, 2013.

[139] G. Andriukaitis *et al.* 90 GW peak power few-cycle mid-infrared pulses from an optical parametric amplifier. Opt. Lett., 36(15):2755–2757, 2011.

[140] G. Sansone *et al.* Isolated single-cycle attosecond pulses. Science, 314(5798):443–446, 2006.

[141] H. C. Kang *et al.* Focusing of hard x-rays to 16 nanometers with a multilayer Laue lens. Appl. Phys. Lett., 92:221114, 2008.

[142] H. D. Jiang *et al.* Quantitative 3D imaging of whole, unstained cells by using x-ray diffraction microscopy. PNAS, 107:11234–11239, 2010.

[143] I. Thomann *et al.* Characterizing isolated attosecond pulses from hollow-core waveguides using multi-cycle driving pulses. Opt. Exp., 17(6):4611–4633, 2009.

[144] J. Itatani *et al.* Attosecond streak camera. PRL, 88(17):173903, 2002.

[145] J. L. Ellis *et al.* Phase matching of noncollinear sum and difference frequency high harmonic generation above and below the critical ionization level. Opt. Exp., 25(9):10126–10144, 2017.

[146] J. Nelson *et al.* High-resolution x-ray diffraction microscopy of specifically labeled yeast cells. PNAS, 107:7235–7239, 2010.

[147] J. Seres *et al.* Coherent superposition of laser-driven soft-x-ray harmonics from successive sources. Nat. Phys., 3:878–883, 2007.

[148] K. Jain *et al.* Ultrafast deep-UV lithography with excimer lasers. IEEE El. Dev. Lett., EDL-3:53, 1982.

[149] M.-C. Chen *et al.* Bright, coherent, ultrafast soft x-ray harmonics spanning the water window from a tabletop light source. PRL, 105(17):173901, 2010.

[150] M. D. Seaberg *et al.* Tabletop nanometer extreme ultraviolet imaging in an extended reflection mode using coherent Fresnel ptychography. Optica, 1:39, 2014.

[151] M. Litos *et al.* High-efficiency acceleration of an electron beam in a plasma wakefield accelerator. Nature, 515(7525):92–95, 2014.

[152] M. R. Gomez *et al.* Experimental demonstration of fusion-relevant conditions in magnetized liner inertial fusion. PRL, 113:155003, 2014.

[153] M. Seaberg *et al.* Ultrahigh 22 nm resolution coherent diffractive imaging using a desktop 13 nm high harmonic source. Opt. Exp., 19:22470, 2011.

[154] O. Kfir *et al.* Generation of bright phase-matched circularly-polarized extreme ultraviolet high harmonics. Nat. Phot., 9:99, 2015.

[155] R. A. Bartels *et al.* Generation of spatially coherent light at extreme ultraviolet wavelengths. Science, 297(5580):376–378, 2002.

[156] R. L. Sandberg *et al.* Near diffraction limited coherent diffractive imaging with tabletop soft x-ray sources. J. Phys.: Conference Series, 186:012058, 2009.

[157] S. Mathias *et al.* Probing the timescale of the exchange interaction in a ferromagnetic alloy. PNAS, 109:4792, 2012.

[158] S. P. Hatchett *et al.* Electron, photon, and ion beams from the relativistic interaction of petawatt laser pulses with solid targets. Phys. Plasmas, 7(5):2076–2082, 2000.

[159] T. Fan *et al.* Bright circularly polarized soft x-ray high harmonics for x-ray magnetic circular dichroism. PNAS, 112:14206, 2015.

[160] T. Popmintchev *et al.* Phase matching of high harmonic generation in the soft and hard x-ray regions of the spectrum. PNAS, 106(26):10516–10521, 2009.

[161] T. Popmintchev *et al.* Bright coherent ultrahigh harmonics in the kev x-ray regime from mid-infrared femtosecond lasers. Science, 336(6086):1287–1291, 2012.

[162] W. P. Leemans *et al.* GeV electron beams from a centimetre-scale accelerator. Nat. Phys., 418:696–699, 2006.

[163] X. M. Tong and C. D. Lin. Empirical formula for static field ionization rates of atoms and molecules by lasers in the barrier-suppression regime. J. Phys. B: AMO Physics, 38:2593–2600, 2005.

[164] R. Trebino. Frequency-Resolved Optical Gating: The Measurement of Ultrashort Laser Pulses. Springer Science and Business Media, 2000.

[165] A. Turpin, L. Rego, A. Picón nd J. San Román, and C. Hernández-García. Extreme ultraviolet fractional orbital angular momentum beams from high harmonic generation. Sci. Rep., 7:43888, 2017.

[166] S. Vasilyev, M. Mirov, and V. Gapontsev. High power Kerr-lens mode-locked femtosecond mid-ir laser with efficient second harmonic generation in polycrystalline Cr2+:ZnS and Cr2+:ZnSe. In ASSL, Shanghai, China, Nov. 16–21 2014. OSA.

[167] M. Verschl. Laser-driven recollisions generalized to relativistic energies. Laser Phys., 18(5):598–607, 2008.

[168] D. N. Vitek, D. E. Adams, A. Johnson, P. S. Tsai, S. Backus, C. G. Durfee, D. Kleinfeld, and J. A. Squier. Temporally focused femtosecond laser pulses for low numerical aperture micromachining through optically transparent materials. Opt. Exp., 18(17):18086–18094, 2010.

[169] B. Walker, B. Sheehy, L. F. DiMauro, P. Agostini, K. J. Schafer, and K. C. Kulander. Precision measurement of strong field double ionization of helium. PRL, 73(9):1227–1230, 1994.

[170] B. Walker, B. Sheehy, K. C. Kulander, and L. F. DiMauro. Elastic rescattering in the strong field tunneling limit. PRL, 77(25):5031–5034, 1996.

[171] Z. Wei, B. Zhou, C. Xu, X. Zhong, Y. Zhang, Y. Zou, and Z. Zhang. All Solid-State Passively Mode-Locked Ultrafast Lasers Based on Nd, Yb, and Cr Doped Media. INTECH Open Access Publisher, 2012.

[172] J. Wildenauer. Generation of the ninth, eleventh, and fifteenth harmonics of iodine laser radiation. J. Appl. Phys., 62:41, 1987.

[173] M. Wu, S. Ghimire, D. A. Reis, K. J. Schafer, and M. B. Gaarde. High-harmonic generation from Bloch electrons in solids. PRA, 91:043839, 2015.

[174] H. Zacharias. Spatio-temporal coherence and non-linear correlation of fel pulses in the soft x-ray regime. In International workshop on X-ray diagnostics and scientific application of the European XFEL, Ryn, Eastern North of Poland, Feb. 14–27 2010.

[175] Q. Zhan. Cylindrical vector beams: from mathematical concepts to applications. Adv. in Opt. and Phot., 1:1–57, 2009.

[176] X. Zhang, A. Lytle, T. Popmintchev, X. Zhou, H. Kapteyn, M. Murnane, and O. Cohen. Quasi-phase-matching and quantum-path control of high-harmonic generation using counterpropagating light. Nat. Phys., 3(4):270–275, 2007.

Appendix A

Hollow Waveguide Modes

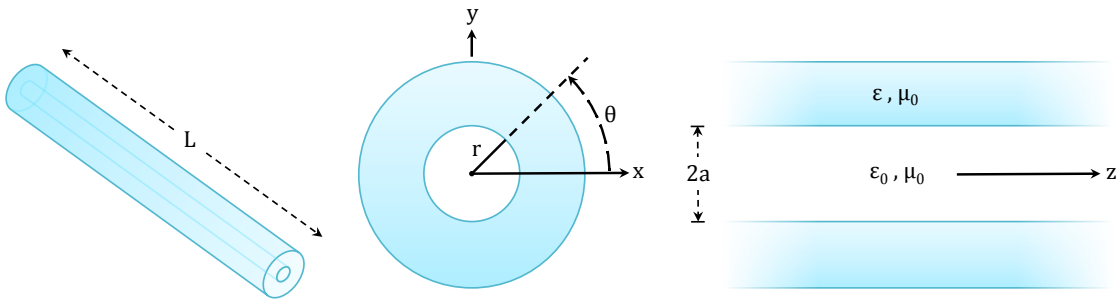

Figure A.1: Illustrations of the hollow waveguide geometry.

Waveguides have a different set of boundary conditions than free space, resulting in a different set of basis modes. In free-space, the basis modes are plane waves, which can be added together to construct any arbitrary field profile. For cylindrically-symmetric hollow capillaries, Bessel modes form a basis. Marcatili solved for the full electromagnetic field components for the hollow waveguide modes in [79] (neglecting powers of λ/a larger than 1). Three categories of modes are discussed: circular/transverse electric (TE), circular/transverse magnetic (TM), and hybrid (EH). The TE and TM modes have azimuthal and radial polarizations, respectively. They also contain a "doughnut" intensity profile, with zero amplitude at the center of the mode. HHG can be possible using these driving modes, as discussed in Section 5.1. Here, the linearly-polarized modes will be investigated in detail. The general EH_{pq} mode has the following field components within the hollow region of the waveguide:

- Internal field components for the EH_{pq} mode in cylindrical coordinates:

$$\begin{aligned}
E_{pq,r} &= \left[J_{p-1}(k_i r) + \frac{iu_{pq}}{2kr}\sqrt{n^2-1}J_p(k_i r)\right]\sin(p\theta)e^{i(\gamma_{pq}z-\omega t)} \\
E_{pq,\theta} &= \left[J_{p-1}(k_i r) + \frac{iu_{pq}^2}{2pka}\sqrt{n^2-1}J_p'(k_i r)\right]\cos(p\theta)e^{i(\gamma_{pq}z-\omega t)} \\
E_{pq,z} &= -i\frac{u_{pq}}{ka}J_p(k_i r)\sin(p\theta)e^{i(\gamma_{pq}z-\omega t)} \\
H_{pq,r} &= -\sqrt{\frac{\epsilon_0}{\mu_0}}E_{pq,\theta} \\
H_{pq,\theta} &= \sqrt{\frac{\epsilon_0}{\mu_0}}E_{pq,r} \\
H_{pq,z} &= -\sqrt{\frac{\epsilon_0}{\mu_0}}E_{pq,z}\cot(p\theta)
\end{aligned} \tag{A.1}$$

For a EH_{pq} mode to be linearly-polarized along the y-direction, it is easy to show that p must be equal to 1, resulting in the following field components:

- Internal field components for the y-polarized EH_{1q} mode in Cartesian coordinates:

$$\begin{aligned}
E_{1q,x} &= 0 \\
E_{1q,y} &= \left[J_0(k_i r) + \frac{iu_{1q}}{2kr^2}\sqrt{n^2-1}\left(\frac{y^2}{r}J_1(k_i r) + \frac{u_{1q}x^2}{a}J_1'(k_i r)\right)\right]e^{i(\gamma_{1q}z-\omega t)} \\
E_{1q,z} &= -i\frac{u_{1q}}{ka}\left(\frac{y}{r}\right)J_1(k_i r)e^{i(\gamma_{1q}z-\omega t)} \\
H_{1q,x} &= -\sqrt{\frac{\epsilon_0}{\mu_0}}E_{1q,y} \\
H_{1q,y} &= 0 \\
H_{1q,z} &= -\sqrt{\frac{\epsilon_0}{\mu_0}}\left(\frac{x}{y}\right)E_{1q,z}
\end{aligned} \tag{A.2}$$

Here, $B = \mu_0 H$, J_p is a p^{th} order Bessel function of the first kind, u_{pq} is the q^{th} root of the equation $J_{p-1}(u_{pq}) = 0$, $n = \sqrt{\epsilon/\epsilon_0}$ is the complex refractive index of the waveguide material, $r = \sqrt{x^2+y^2}$, $k = 2\pi/\lambda$, $k_i = \sqrt{k^2 - \gamma_{pq}^2}$, and:

$$\gamma_{pq} = k\left[1 - \frac{1}{2}\left(\frac{u_{pq}}{ka}\right)^2\left(1 - \frac{i}{ka}\frac{(n^2+1)}{\sqrt{n^2-1}}\right)\right] \tag{A.3}$$

These solutions are valid for $\lambda << a$. Under this condition, the z-component of the mode is small, as are the latter terms in the square brackets (terms containing higher order Bessel functions).

Furthermore, the boundary conditions at $r = a$ allow the replacement: $J_0(k_i r) \rightarrow J_0\left(u_{1q}\,\frac{r}{a}\right)$. With these assumptions, the linearly-polarized modes have the following electric field component along the y-direction:

$$E_{1q,y} \cong J_0\left(u_{1q}\,\frac{r}{a}\right) e^{i(\gamma_{1q} z - \omega t)} \tag{A.4}$$

The EH_{1q} modes form a basis that can represent any linearly-polarized mode profile with cylindrical symmetry. Thus, one can consider an input laser mode incident on the entrance of a hollow waveguide. The amount of light coupled into each of the waveguide modes can be calculated through mode decomposition, as investigated in [1]. Consider an input Gaussian mode with power normalization:

$$\begin{gathered} E_{input}(r) = \sqrt{\frac{2}{\pi w(z)^2}}\; e^{-r^2/w(z)^2}\,\hat{y} \\ \int_0^{2\pi} d\theta \int_0^{\infty} dr\; r\,|E_{input}(r)|^2 = 1 \end{gathered} \tag{A.5}$$

The normalized basis functions for the decomposition are:

$$\begin{gathered} \bar{E}_{1q}(r) = \frac{\sqrt{2}}{a J_1(u_{1q})} J_0\left(u_{1q}\,\frac{r}{a}\right)\hat{y} \\ \int_0^{2\pi} d\theta \int_0^{a} dr\; r\,|E_{1q,y}(r)|^2 = 1 \end{gathered} \tag{A.6}$$

The input field can be represented as a sum of the basis functions:

$$E_{input}(r) = \sum_q c_{1q} \bar{E}_{1q}(r), \tag{A.7}$$

where

$$\begin{aligned} c_{1q} &= \int_0^{2\pi} d\theta \int_0^{a} dr\; r\,\bar{E}_{1q}(r)^*\,E_{input}(r) \\ &= \frac{2}{\sqrt{\pi}\,a w(z) J_1(u_{1q})} \int_0^{2\pi} d\theta \int_0^{a} dr\; r\,J_0\left(u_{1q}\,\frac{r}{a}\right)\; e^{-r^2/w(z)^2} \end{aligned} \tag{A.8}$$

The power coupled from the input Gaussian beam into each mode is simply $P_{1q} = |c_{1q}|^2$. Note that this derivation assumes a flat wavefront for the input field ($z = 0$, $w(z) = w_0$). If, for instance, there is wavefront curvature (indicating a Gaussian mode that is focusing or defocusing at the waveguide entrance), then there would be an additional phase term inside the integral of Eq. (A.8) taking the

form:

$$exp\left(\frac{ikr^2}{2R(z)}\right) = exp\left(i2\pi N\frac{r^2}{a^2}\right) \tag{A.9}$$

Here, $R(z)$ represents the wavefront radius of curvature, and N is the number of waves between the center of the waveguide and the wall at $r = a$. Figure A.2 shows the power coupled into the first five EH_{1q} modes for input Gaussian modes with varying radii and wavefront curvature.

Because the complex wavenumber γ_{pq} is dependent on the mode indices p and q, each mode will propagate at a different phase velocity, and with a different propagation loss. Therefore, any input field that couples into more than one waveguide mode will change its spatial profile during propagation. Beating effects will result in modulation of the peak intensity along the longitudinal direction. For long propagation distances, the modes with the lowest loss (those with the lowest values of p and q) will dominate.

The analysis performed for the linearly-polarized Gaussian modes coupled to the hybrid waveguide modes can be replicated in the case of radially- and azimuthally-polarized modes. In this scenario, the relevant waveguide modes are the TE_{0q} and TM_{0q} modes from [79]. As mentioned previously, these have "doughnut" intensity profiles. Using the TE_{0q} mode to represent this profile, the basis modes have the following normalized amplitudes:

$$TE_{0q} = \bar{E}_{0q}(r) = \frac{1}{\sqrt{\pi}\,aJ_0(u_{2q})}J_1\left(u_{2q}\,\frac{r}{a}\right) \tag{A.10}$$

As for the free-space modes with radial/azimuthal polarizations, the solutions are Laguerre-Gauss beams (or cylidrical vector beams) as described in [175]. The lowest order mode is the LG_{01} mode, which has the following normalized amplitude:

$$LG_{01} = \frac{2}{\sqrt{\pi}\,w(z)^2}\,r\,e^{-r^2/w(z)^2} \tag{A.11}$$

Note that the LG_{01} mode contains the same spot width parameter $w(z)$ as for Gaussian modes, but it does not correspond to the radius at which the intensity drops by $1/e^2$. Instead, the maximum intensity of the "doughnut" mode occurs at a radius $r = w/\sqrt{2}$. The intensity at $r = w$ is equal to the maximum intensity multiplied by $(2/e)$, where $e = 2.718$ is the natural Euler number (Fig.

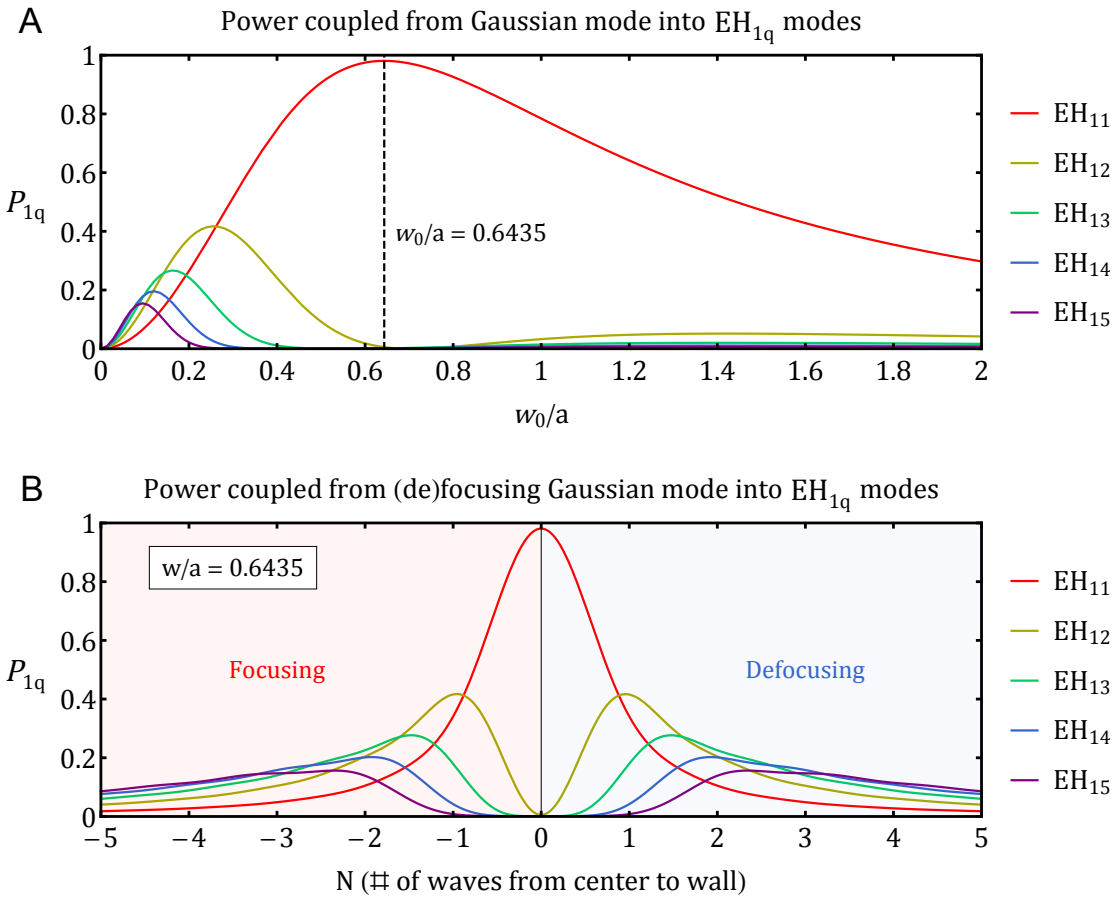

Figure A.2: The power coupled from Gaussian modes into the first five EH_{1q} waveguide modes. (A) Coupling of Gaussian modes with flat wavefront and varying mode radii. The optimal coupling of the Gaussian mode into the EH_{11} mode occurs for $w_0/a = 0.6435$, with 98% coupling efficiency. (B) Coupling of Gaussian modes with optimal radii but with varying wavefront curvature.

A.3). Following the same modal decomposition, the power coupled from the LG_{01} mode into the TE_{0q} modes can be calculated, and these are plotted as a function of w_0/a in Fig. A.4.

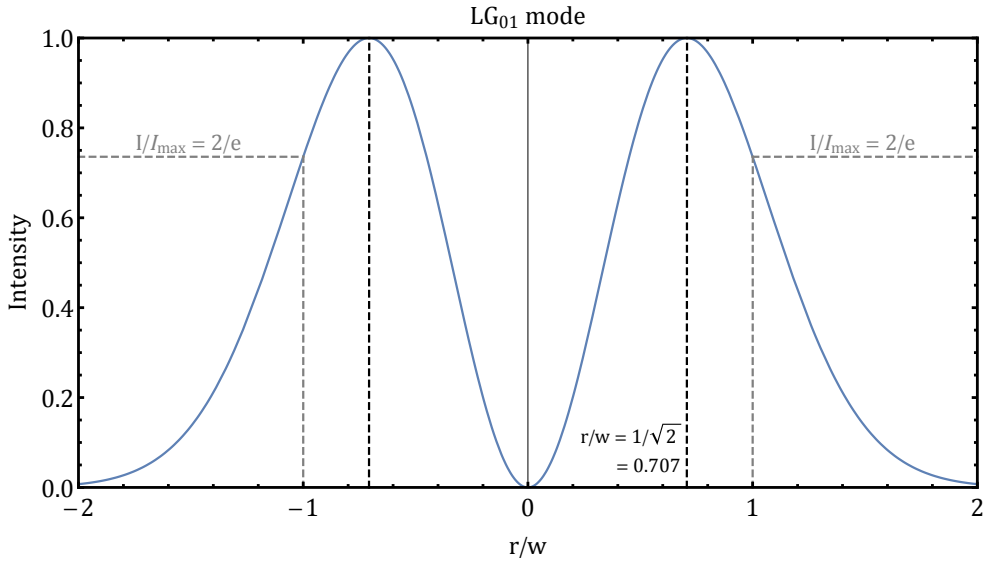

Figure A.3: Plot of the LG_{01} mode intensity as a function of radius. The beam spot width parameter w does not carry the same meaning as it does for a Gaussian beam, despite it following the same $w(z)$ equation through propagation (Eq. (1.76)).

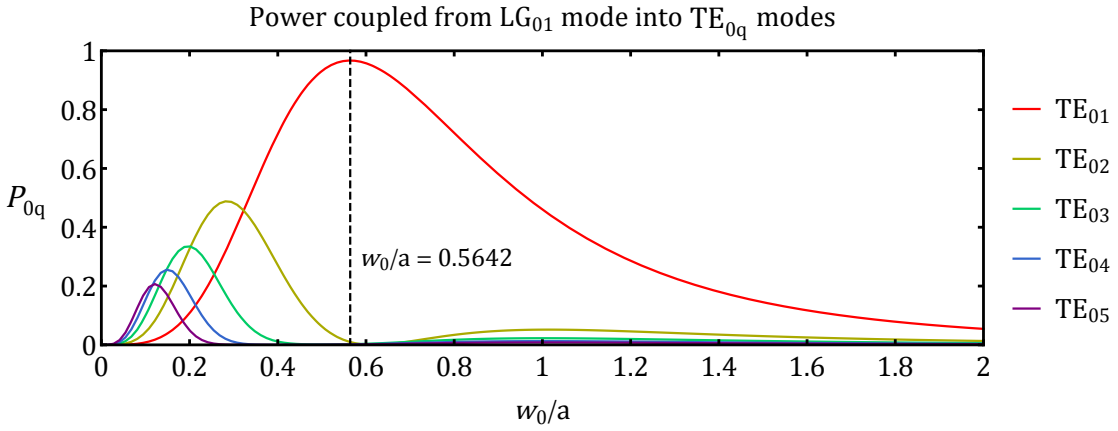

Figure A.4: The power coupled from azimuthally-polarized LG_{01} modes into the first five TE_{0q} waveguide modes. The plots are the same for radially-polarized LG_{01} modes coupling to the TM_{0q} modes. The optimal coupling of the LG_{01} mode into the TE_{01} mode occurs for $w_0/a = 0.5642$, with 96.7% coupling efficiency. The wavefront is assumed to be flat for this calculation.